Earth Observation-based Time Series Analysis of Retrogressive Thaw Slump Dynamics in the Russian High Arctic

Master Thesis

to attain the academic degree

Master of Science (M.Sc.) in Geosciences

submitted by

Sophia Barth

Supervisors: Prof. Dr. Guido Grosse

Dr. Ingmar Nitze

Institute for Geosciences at the University of Potsdam

Permafrost Section at the Alfred Wegener Institut Potsdam

Potsdam, 29.07.2022

Selbstständigkeitserklärung

Hiermit versichere ich, dass ich die vorliegende Arbeit ohne Hilfe Dritter und ohne Zuhilfenahme anderer als der angegebenen Quellen und Hilfsmittel angefertigt habe. Die den benutzten Quellen wörtlich oder inhaltlich entnommenen Stellen sind als solche kenntlich gemacht. Die „Richtlinie zur Sicherung guter wissenschaftlicher Praxis für Studierende an der Universität Potsdam (Plagiatsrichtlinie) - Vom 20. Oktober 2010“, im Internet unter https://www.uni-potsdam.de/am-up/2011/ambek-2011-01-037-039.pdf, habe ich zur Kenntnis genommen.

Potsdam, 29.07.2022

Acknowledgements

First and foremost, I would like to thank my supervisors Ingmar Nitze and Guido Grosse for their excellent support. Thank you for encouraging me to pursue my interests, to try out new ideas and for always taking the time to answer my questions. Thank you also for the opportunity to present a preliminary part of this work at the the ESA Living Planet Symposium in Bonn and the 16th International Circumpolar Remote Sensing Symposium in Fairbanks.

A big thank you goes to the whole Permafrost Remote Sensing Team for the professional support, the lively exchange of knowledge and the terrific working atmosphere. Thank you Alexandra Runge, Cornelia Inauen, Tabea Rettelbach, Bennet Juhles and Sebastian Laboor. Many thanks also to all the other colleagues from AWI Potsdam for the numerous inspiring conversations.

My special thanks go to my friends and family, who were always there for me and cheered me on. In particular, I would like to thank Igor and Pauline for their tireless support in every way. This support has contributed significantly to the completion of this work.

Abstract

While temperatures are rising globally, they are rising more than twice as fast in the Arctic. Landscapes underlain by permafrost are especially vulnerable to this changing climate and experience increased thaw and degradation. The proceeding warming of organic-rich frozen ground is a highly relevant driver of carbon release into the atmosphere. Retrogressive Thaw Slumps (RTSs) are dynamic thermokarst features which develop when ice-rich permafrost thaws and thus are important indices when it comes to the assessment of potential carbon sources in permafrost landscapes.

Thousands of RTSs have been inventoried in northwestern Canada. These inventories showed that thaw slumping modifies terrain morphology and alters the discharge into aquatic systems resulting amongst others in infrastructure instabilities and ecosystem changes. Furthermore, recent studies project that abrupt thermokarst processes contribute significant amounts of greenhouse gas emissions.

As observed in most arctic regions, RTS activity has increased in the Russian High Arctic, however, little research has been done on RTSs in this region. The objective of this study is to better understand growth pattern and development rates of RTSs in northern Russia during the last decade. The study area consists of five different sites in the Russian High Arctic covering an area of more than 600 km^2. The sites are located on the Novaya Zemlya Archipelago, Kolguev Island, Bol'shoy Lyakhovsky Island and Taymyr Peninsula in ice-rich permafrost characterized by either buried glacial ice deposits or syngenetically formed Yedoma permafrost. To assess changes in number and extent, a GIS based inventory of manually mapped RTSs was created. The inventory is based on multispectral imagery of high-resolution satellite sensors, including PlanetScope, RapidEye, Pléiades and SPOT. Cloud free images were acquired between 2011 and 2020 and exist for each or every few years depending on their availability. Additional data sets such as ArcticDEM, Esri Satellite base map and Tasseled Cap Landsat Trends were used to support the mapping process. From the extracted individual RTS objects, changes in number and surface area were calculated. Furthermore, for coastal slumps thermal denudation and thermal abrasion rates were computed.

The results show that RTS activity was high at the study sites during the investigation period and that the diverse sites revealed different RTS characteristics, with non-coastal

RTSs showing a much larger increase in area. At the non-coastal sites, RTS-affected area increased by a factor of 2 (100 %) in West Taymyr, a factor of 4 (400 %) in Novaya Zemlya, and a factor of 33 (3300 %) in East Taymyr, with particularly large increases in more recent years. At the coastal sites, total RTS area increased by a factor of 1.2 (20%) in North Kolguev, remained the same in South Kolguev, and decreased slightly by a factor of 0.95 (5%) in Bol'shoy Lyakhovsky. Headwall and base of the coastal slumps retreated at different rates. However, at all coastal sites, erosion of the headwall and base progressed, demonstrating that RTS activity cannot be determined by area changes alone because coastal RTSs are strongly influenced by thermal abrasion and thermal denudation which diminishes areal changes. Moreover, the number of RTS did not necessarily increase with increasing RTS activity. At all study sites except East Taymyr, increased RTS activity resulted from RTS growth rather than new RTS initiation. In addition, climate analysis revealed that the mean temperature increased significantly, within the last decade at all sites, potentially favouring RTS initiation and growth.

The findings of this study contribute substantially to our understanding of regional permafrost thaw in the Russian High Arctic. Nevertheless, further research is needed to quantify volumetric permafrost loss and associated carbon release comprehensively throughout the Russian High Arctic to better understand RTS dynamics and their impact on greenhouse gas release.

Zusammenfassung

Während die Temperaturen weltweit steigen, steigen sie in der Arktis mehr als doppelt so schnell. Permafrostlandschaften sind durch den Klimawandel besonders gefährdet und von verstärktem Auftauen und Degradation betroffen. Die fortschreitende Erwärmung des organisch reichen gefrorenen Bodens ist ein sehr wichtiger Faktor für die Freisetzung von Kohlenstoff in die Atmosphäre. Retrogressive Thaw Slumps (RTSs) oder 'Retrogressive Taurutschungen', sind dynamische Thermokarst-Merkmale, die beim Auftauen von eisreichem Permafrost entstehen und somit ein wichtiger Indikatoren für die Bewertung potenzieller Kohlenstoffquellen in Permafrostlandschaften. Tausende Taurutschungen wurden im Nordwesten Kanadas untersucht. Diese Studien haben gezeigt, dass Taurutschungen die Geländemorphologie und den Abfluss in aquatische Systeme verändern, was u. a. zu Instabilitäten der Infrastruktur und Veränderungen des Ökosystems führt. Darüber hinaus gehen neuere Studien davon aus, dass abrupte Thermokarstprozesse erhebliche Mengen an Treibhausgasemissionen verursachen.

Wie in den meisten arktischen Regionen hat die Taurutschungs-Aktivität auch in der russischen Hocharktis zugenommen, allerdings wurden bisher nur wenige Taurutschungen in dieser Region untersucht. Ziel dieser Studie ist es, die Wachstumsmuster und Entwicklungsraten von Taurutschungen in Nordrussland während des letzten Jahrzehnts besser zu verstehen. Das Untersuchungsgebiet besteht aus fünf verschiedenen Standorten in der russischen Hocharktis und nimmt eine Fläche von mehr als 600 km^2 ein. Die Standorte befinden sich auf dem Novaya Zemlya Archipel, der Kolguev Insel, der Bolshoy Lyakhovsky Insel und der Taymyr Halbinsel in eisreichem Permafrost, der entweder durch verbleibende Gletschereisablagerungen oder syngenetisch gebildetem Yedoma Permafrost gebildet wird. Zur Bewertung der Veränderungen in Anzahl und Ausdehnung wurde ein GIS-basiertes Inventar manuell kartierter Taurutschungen erstellt. Die Bestandsaufnahme basiert auf multispektralen Bildern von hochauflösenden Satellitensensoren, darunter PlanetScope, RapidEye, Pléiades und SPOT. Die wolkenfreien Bilder wurden zwischen 2011 und 2020 aufgenommen und liegen je nach Verfügbarkeit für jedes oder alle paar Jahre vor. Zusätzliche Datensätze wie ArcticDEM, Esri Satellite Base Map und Tasseled Cap Landsat Trends wurden zur Unterstützung des Kartierungsprozesses verwendet. Aus den extrahierten einzelnen Taurutschungen wurden

die Veränderungen in Anzahl und Fläche berechnet. Darüber hinaus wurden für Küstentaurutschungen die Raten der thermischen Denudation und der thermischen Abrasion berechnet. Die Ergebnisse zeigen, dass die Taurutschungs-Aktivität an den Untersuchungsstandorten während des Untersuchungszeitraums hoch war und dass die verschiedenen Standorte unterschiedliche Merkmale aufwiesen, wobei die Taurutschungen an den nicht-küstenbeeinflussten Standorten eine wesentlich größere Flächenvergrößerung aufwiesen. An den nicht-küstenbeeinflussten Standorten nahm die von Taurutschungen betroffene Fläche in West Taymyr um den Faktor 2 (100%), in Novaya Zemlya um den Faktor 4 (400%) und in East Taymyr um den Faktor 33 (3.300%) zu, wobei die Zunahme in den letzten Jahren besonders stark war. An den Küstenstandorten nahm die gesamte Taurutschungsfläche in Nord-Kolguev um den Faktor 1,2 (20%) zu, in Süd-Kolguev blieb sie gleich und in Bol'shoy Lyakhovsky ging sie leicht um den Faktor 0,95 (5%) zurück. Die Abrisskante und der Steilwandfuß der küstennahen Taurutschungen zogen sich unterschiedlich schnell zurück. An allen Küstenstandorten schritt die Erosion der Abrisskante und der Basis jedoch voran, was zeigt, dass die Taurutschungs-Aktivität nicht allein durch Flächenveränderungen bestimmt werden kann, da die Taurutschungen an der Küste stark durch thermische Abrasion und thermische Denudation beeinflusst werden, was die Flächenveränderungen verringert. Außerdem nahm die Anzahl der Taurustchungen nicht unbedingt mit zunehmender Taurutschungs-Aktivität zu. An allen Untersuchungsstandorten mit Ausnahme von East Taymyr resultierte die erhöhte Taurutschungs-Aktivität eher aus dem Wachstum als aus dem Entstehen neuer Taurutschungen. Darüber hinaus ergab die Klimaanalyse, dass die Durchschnittstemperatur in den letzten zehn Jahren an allen Standorten erheblich gestiegen ist, was die Entstehung und das Wachstum von retrogressiven Taurutschungen begünstigt haben könnte.

Die Ergebnisse dieser Studie tragen wesentlich zu unserem Verständnis des regionalen Permafrosttauens in der russischen Hocharktis bei. Dennoch sind weitere Forschungsarbeiten erforderlich, um den volumetrischen Permafrostverlust und die damit verbundene Kohlenstofffreisetzung in der gesamten russischen Hocharktis umfassend zu quantifizieren, um die Taurutschungs-Dynamiken und ihre Auswirkungen auf die Freisetzung von Treibhausgasen besser zu verstehen.

Contents

List of Figures

List of Tables

1 Introduction

Since pre-industrial times, anthropogenic greenhouse gas emissions have led to a warming of the Earth's climate. In the first two decades of the 21st century (2001–2020) the global surface temperature was 0.99 [0.84 to 1.10] °C higher than between 1850 and 1900 (IPCC, 2021). The effects of climate warming are already being felt particularly strongly in the Arctic. The Arctic surface temperature has risen by more than twice the global average over the last two decades (IPCC, 2019). The more rapid surface temperature increase in the Arctic, referred to as Arctic Amplification, is driven by local feedbacks, especially temperature and sea-ice related feedbacks, as well as changes in the poleward energy transport (Previdi et al., 2021). Profound environmental changes due to climate warming are visible in various parts of the Arctic cryosphere and include, the decrease in sea and land ice extent, the reduction of spring snow cover extent and the warming and thawing of permafrost (IPCC, 2019; Biskaborn et al., 2019b).

Landscapes underlain by permafrost are a major component of the Arctic cryosphere and especially sensitive to climate change (Romanovsky et al., 2010; Grosse et al., 2011). Permafrost occurs on land and beneath offshore Arctic continental shelves. It covers large parts of the earth's surface: About 14 million km² - or 15 % of the exposed land surface in the Northern Hemisphere – is underlain by permafrost (Obu, 2021). These frozen soils store large quantities of organic matter that contain approximately twice as much carbon as we detect in the atmosphere today. The carbon in the frozen ground derives from animal and plant remains that have been stored in the earth for thousands of years due to low decomposition rates, which in turn have been caused by low soil temperature and obstructed drainage (Schuur et al., 2008). Recent changes in the soil thermal regimes triggered by climate change result in increased thaw and degradation of permafrost. As a consequence, increased microbial activity in the thawing permafrost leads to the release of the greenhouse gases (GHGs) carbon dioxide and methane (Abbott et al., 2016; Mackelprang et al., 2011). The release of GHG from permafrost into the atmosphere causes a positive feedback (permafrost carbon feedback) to global warming. This feedback loop represents a highly relevant driver of GHG into the atmosphere, however, numerous interactions of the permafrost with the environment complicate a sufficient assessment of the danger at hand (Schuur et al., 2015; Strauss et al., 2017).

In ice-rich permafrost soils, thawing induces thermokarst formation which results in surface subsidence and the formation of characteristic landforms. Retrogressive Thaw Slumps (RTSs) are dynamic thermokarst features which result from slope failure after ice-rich permafrost thaws. Thousands of RTSs have been inventoried in Northwestern Canada in regions where buried glacial ice is melting in thawing permafrost. These inventories showed that thaw slumping substantially modifies terrain morphology and alters the discharge into aquatic systems (Kokelj et al., 2013), also resulting in infrastructure instabilities (Hjort et al., 2022). Most RTSs occur along coast- and shorelines, leading to changes in optical and biogeochemical properties of aquatic systems which can have severe consequences on the aquatic food web (Kokelj et al., 2009a). Furthermore, recent studies have shown increased temporal thaw dynamics of RTSs in Northern high latitudes (Runge et al., 2022; Ward Jones et al., 2019; Lewkowicz & Way, 2019; Bernhard et al., 2022b) and projected that abrupt thermokarst disturbances contribute significant amounts of greenhouse gas emissions (Knoblauch et al., 2021). As observed in most Arctic regions, RTSs have also been developing in the Russian High Arctic (Ardelean et al., 2020; Nitze et al., 2018; Runge et al., 2022). However, research on RTSs in northern Russia has mostly focused on Yamal peninsula, where industrial development required mapping of potential landscape hazards resulting from permafrost thaw (Ardelean et al., 2020). In most other regions of the Russian High Arctic, RTS occurrence and distribution is poorly known so far. The objective of this study is to better understand growth pattern and development rates of RTSs at high temporal resolution in high Arctic Russia, using remote sensing data of the last decade (2011 to 2020).

2 Background

2.1 Permafrost

By definition Permafrost, or perennially cryotic ground, is ground that remains at or below 0 °C for at least two consecutive years (van Everdingen, 2005). It can consist of rock, sediments or soil and contain varying amounts of ice and organic material. Since, in most cases, the ground has been frozen for several thousand years, it stores large quantities of organic carbon and prevents it from being broken down and released. Approximately 1460 to 1600 petagrams of organic soil carbon is currently stored in terrestrial permafrost regions in the northern Hemisphere (IPCC, 2019). These climate-sensitive carbon stocks are a major component of the carbon cycle and therefore are of great importance for climate change (Grosse et al., 2011).

The first permafrost probably formed prior to or during the first ice age at around 2.3 billion years ago. Ever since the distribution and thickness varied due to subsequent ice ages (Osterkamp & Burn, 2003). The extent of the permafrost region spreads over around 21 million km^2, predominantly located in the Northern Hemisphere. Of these approximately 14 million km^2 or 15 % of the exposed land surface in the Northern Hemisphere, are underlain by permafrost (Obu, 2021). A distinction is made between continuous permafrost in cold regions, where at least 90 % of the region is frozen, discontinuous permafrost, where between 50-90 % of a region is underlain by permafrost, sporadic permafrost, where it makes up regionally between 10-50 % and isolated patches, which defines regions where less than 10 % of permafrost is present in the ground (Fig.2.1) (Brown et al., 1997). Most of these soils are found in the polar regions, where permafrost exists both on land and beneath offshore arctic continental shelves. In lower latitudes permafrost occurs in high mountains.

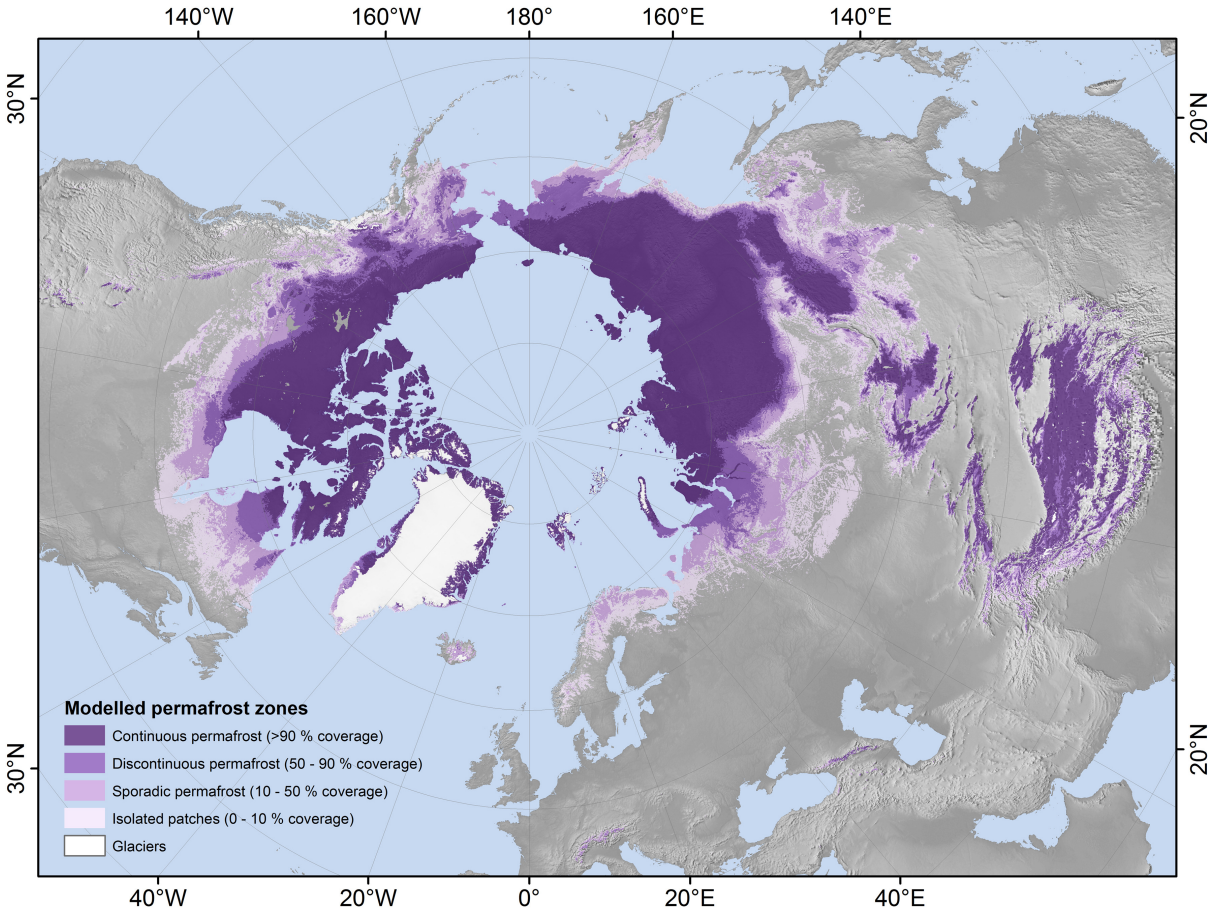

Figure 2.1: Map of Permafrost zonation in the Northern Hemisphere based on TTOP modelling for 2000–2016 at 1 km^2 scale (Obu et al., 2019).

Generally, the soil profile of permafrost consists of two main sections: the near surface layer, termed Active Layer (AL), which thaws by about 15 to 100 centimetres every summer and the frozen layer (permafrost) which lies underneath (Fig.2.2). In between these two layers a dynamic transition zone, especially rich in ice, exists (Shur et al., 2005). Underneath the permafrost, where the freezing point is exceeded, an unfrozen ground layer, also called Talik, begins. Taliks can also exist within the permafrost layer forming unfrozen lenses, e.g. beneath lakes and large rivers. The respective thicknesses of the individual layers depend on many variables. Among others, the climate, the thickness of the snow cover, the vegetation and the organic layer have a significant influence. The greatest thickness of permafrost is found in north-eastern Siberia where it reaches about 1.6 kilometres in depth (Biskaborn et al., 2019a).

The ice content in permafrost soils is of particular interest for assessing the thermal vulnerability (Grosse et al., 2011). Permafrost with low ice content ($<$ 10 % by volume) makes up the largest share, approximately 66.5 % of the total permafrost area, and is

predominantly observed in high plateaus and mountainous regions. Ice-rich permafrost (> 20 % by volume), particularly prone to thawing (Grosse et al., 2011; Strauss et al., 2017), represents almost 9 % of the total permafrost area and is mostly found at high latitudes (Zhang et al., 2008). Yedoma permafrost, widespread in Siberia and Alaska, is a special type of ice-rich, syngenetically formed permafrost. It consist of fine sediments and is especially rich in both, syngenetic and segregated ice, containing a total of between 44 and 48 vol% of ground ice (Strauss et al., 2017). These characteristic soils which formed during the late Pleistocene currently lock more than 25 % (including deposits of degradation features) of the organic carbon stored in permafrost regions and are particularly vulnerable to climate change (Strauss et al., 2017). Besides Yedoma permafrost, there is also ice-rich permafrost in areas formerly dominated by glaciers, which is often epigenetically formed and contains remaining glacier ice.

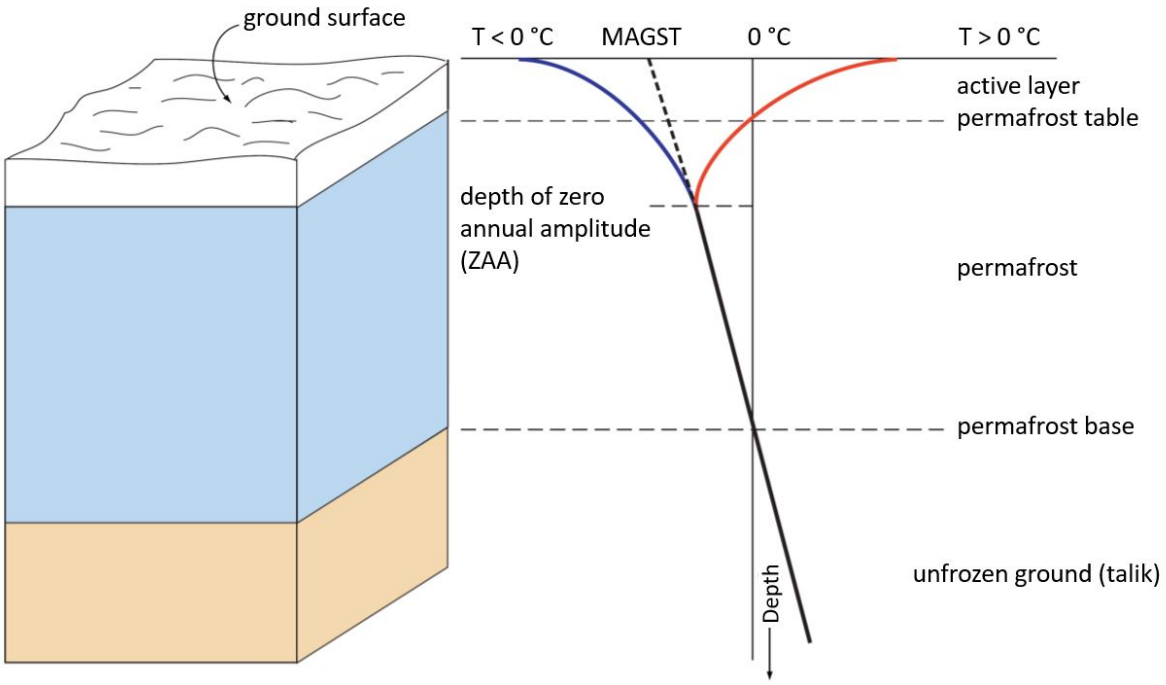

Figure 2.2: Schematic representation of the most important terms related to permafrost and a typical temperature profile. The red and blue curves correspond to the warmest temperatures in summer and the coldest in winter, respectively. MAGST is the mean annual ground surface temperature (modified after Nötzli & Gruber (2005)).

2.2 Permafrost in a changing climate

The Arctic near-surface air temperature is rising three times faster than the global average. Between 1971 and 2019, the average yearly Arctic near-surface air temperature increased

by 3.1 °C (AMAP, 2021). According to the Intergovernmental Panel on Climate Change's Sixth's Assessment Report, the air temperature in the Arctic is projected to rise even further – to between 3.3 and 10 °C depending on the course of future emissions by the end of this century (IPCC, 2019). Permafrost thaw and degradation is a major result of the rising surface temperatures and can have far-reaching consequences for ecosystems, hydrology, human infrastructure and the global climate (AMAP, 2021). The temperature rise in permafrost soils is influenced by several physical factors and thus not progressing at the same rate across the entire Arctic. Recent studies found that Permafrost temperatures rise occurs overall faster in colder continuous permafrost zones than in warmer discontinuous permafrost zones (IPCC, 2019). Warming and thawing of the frozen ground accelerates the microbial breakdown of soil organic carbon and can result in a release of the greenhouse gases carbon dioxide an methan. Regionally the degradation proceeds, for instance due to deepening of the active layer and locally also rapidly and irreversibly through thermokarst processes. The thaw process is complex and influenced by many factors such as thickness of snowcover, thickness of organic layer and occurrence and intensity of disturbances like wildfires. All of these factors greatly effect the heat conduction into the ground and thus can enhance thawing. Although projections of the total release of GHGs from permafrost soils vary, and highly depend on anthropogenic emission scenarios, most scientists agree that by 2100 permafrost will become a carbon source to the atmosphere (Abbott et al., 2016). Greenhouse gas release into the atmosphere of only a fraction of the organic carbon stored in permafrost soils could significantly contribute to the global temperature rise and thus enhance the rate of future climate change, a process known as the permafrost carbon feedback (Schuur et al., 2008).

2.2.1 Thermokarst

Although all permafrost can be affected by thawing and thus severely effect the immediate environment and the climate, a particularly strong impact on surface stability, microtopography, hydrology, ecosystem function, and the carbon cycle is observed when ice-rich permafrost thaws (Grosse et al., 2011). Processes which result of the thawing of ice-rich permafrost and the melting of massive ground ice are referred to as thermokarst. The main thermokarst processes involve hill slope, thaw lake and wetland processes and result in the formation of characteristic landforms. Hill slope processes include

Retrogressive Thaw Slumps (RTS), Active Layer Detachment Slide (ALDS) and Thermal Erosion Gullies. Thaw lake processes include lake expansion, drainage and lake basin development. Processes in wetlands include peatland collapse and bog and fenland development. Since the formation of permafrost, thermokarst processes have been an important component in shaping permafrost landscapes, however, in the course of recent climate change thermokarst processes have increased in frequency and magnitude (Kokelj & Jorgenson, 2013; Nitze et al., 2018).

(a) RTS on Bol'shoy Lyakhovsky (coastal)

(b) Selawik Slump (non-coastal)

Figure 2.3: Field photos of RTS; (a) Picture of a, according to my definition, coastal RTS on Bol'shoy Lyakhovsky island taken in 1988., (b) Picture of a, according to my definition, non-coastal RTS in West Alaska (Selawik Slump) taken in 2016. Photo credits: (a) Lutz Schirrmeister, (b) Ingmar Nitze.

2.2.1.1 Retrogressive Thaw Slumps

Retrogressive Thaw Slumps are dynamic thermokarst features which develop on hill slopes when ice-rich permafrost thaws. RTSs are commonly observed throughout the entire Arctic, in various regions of western Canada, Alaska and Siberia, predominantly in areas underlain by remnant glacier ice or by ice-rich permafrost of the Yedoma domain (Kokelj & Jorgenson, 2013). While they are small-scale features they can reach considerable annual growth rates, with headwall retreat up to several meters per summer (Lantz & Kokelj, 2008), impacting the immediate surrounding abruptly and irreversibly.
Active RTSs are characterized by a steep, ice-rich headwall (up to tens of meters high), a low-angled scar zone consisting of thawed muddy material and a dynamic slump floor with incised gullies that can be several hectares in area, mobilizing thawed sediments, carbon, and nutrients into downstream environments (Fig.2.4) (Kokelj et al., 2015; Ramage et al., 2017; Lantuit & Pollard, 2008). RTSs can grow for decades or stabilize over time. Stable RTSs can be distinguished from active slumps by their inactive, more gentle sloping headwalls and vegetated slump floors (Ramage et al., 2017; Lantuit & Pollard, 2008). Since RTSs are polycyclic features, once stabilized they can be re-initiated by various feedback mechanisms (Kokelj & Jorgenson, 2013; Runge et al., 2022).

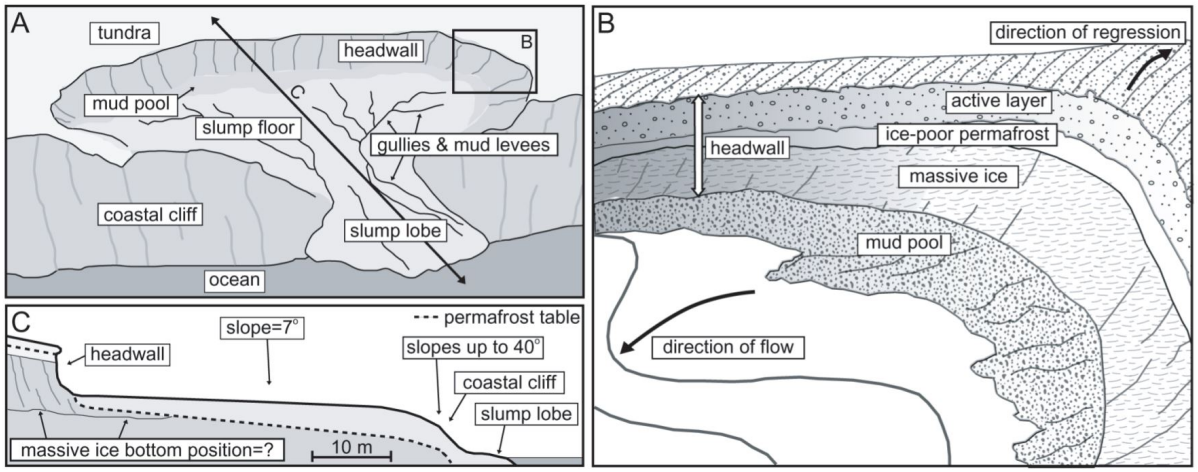

Figure 2.4: Conceptual scheme of retrogressive thaw slump. Inset B focuses on the slump headwall. Inset C is a cross-section of the slump. The diagram shows the relation between retrogressive thaw slump development and massive ground ice occurrence (after Lantuit & Pollard (2005)).

Thaw Slumps most often occur close to coast and shorelines. Along the interface of land and water mechanical forces, including fluvial and wave erosion and thermal processes,

including solar radiation and heat advection can lead to the exposure of ground ice on permafrost slopes and thus initiate RTS formation (Kokelj & Jorgenson, 2013). Along lake shores thermally driven subsidence is a common process resulting in the development of thaw slumping (Kokelj et al., 2009b). Along permafrost coastlines RTSs can be influenced by the two major coastal erosion processes thermal abrasion and thermal denudation. Thermal abrasion is the combined mechanical and thermal effect of wave energy at the base of the slump and thermal denudation describes the combined influence of solar insolation and heat advection which drives the headwall regression (Günther et al., 2013). Both processes can be considered separately, however, the movement of the headwall is influenced by the removal of deposited slump material from the base of the bluff.
The initiation and intensity in RTS development varies, both spatially and temporally, depending on a variety of geomorphic, hydrological and climatic influencing factors such as ground ice content and slope orientation as well as heavy precipitation and high-temperature events (Günther et al., 2012; Kokelj & Jorgenson, 2013; Kokelj et al., 2015). Already today, the consequences of thaw slumping are numerous, including impacts on the morphology of the terrain and the modification of the discharge into aquatic systems resulting in infrastructure instabilities and ecosystem changes (Kokelj et al., 2013; Hjort et al., 2022). Various studies showed that the activity of RTSs has accelerated in the context of climate change (Lantuit & Pollard, 2005, 2008; Runge et al., 2022) reinforcing these impacts. Furthermore, projections show that the organic carbon exposed through slumping will potentially increase the GHG concentration in the atmosphere (Knoblauch et al., 2021; Bernhard et al., 2022b) and thus further heat up the climate.

2.3 Aim

The occurrence and distribution of RTSs in the northern high latitudes of Russia is poorly known so far. The aim of this study is to get a detailed understanding of RTS patterns and development rates throughout the Russian High Arctic. The main research questions that shaped this thesis are:

(1) How have RTS dynmaics in the Russian High Arctic developed over the past decade?
(2) Where do RTSs form and what might trigger RTS initiation and growth?

(3) Is enhanced RTS activity showing up in recent years as observed in other studies which investigated slumping the High Arctic?
(4) Are the development rates of RTS observed in this study comparable to those observed in other High Arctic regions?

3 Study area

Within the context of this study, I investigated five diverse sites located in the Russian High Arctic. The area subject to this study spans more than 600 km^2 and is located on Novaya Zemlya Archipelago, Kolguev Island, Bol'shoy Lyakhovsky Island and Taymyr Peninsula (Fig.3.1).

Two of the study sites are located on the West Coast of Kolguev, hereafter referred to as North and South Kolguev. Two further sites are located on the Taymyr Peninsula, one to the east and one to the west, referred to below as East Taymyr and West Taymyr. Additionally, there is a site located on the West Coast of Novaya Zemlya Archipelago and another one on the South Coast of Bol'shoy Lyakhovsky Island. With the exception of the two sites on Kolguev Island, which are situated in the sporadic permafrost zone, all other sites are located in the continuous permafrost zone (Obu et al., 2019).

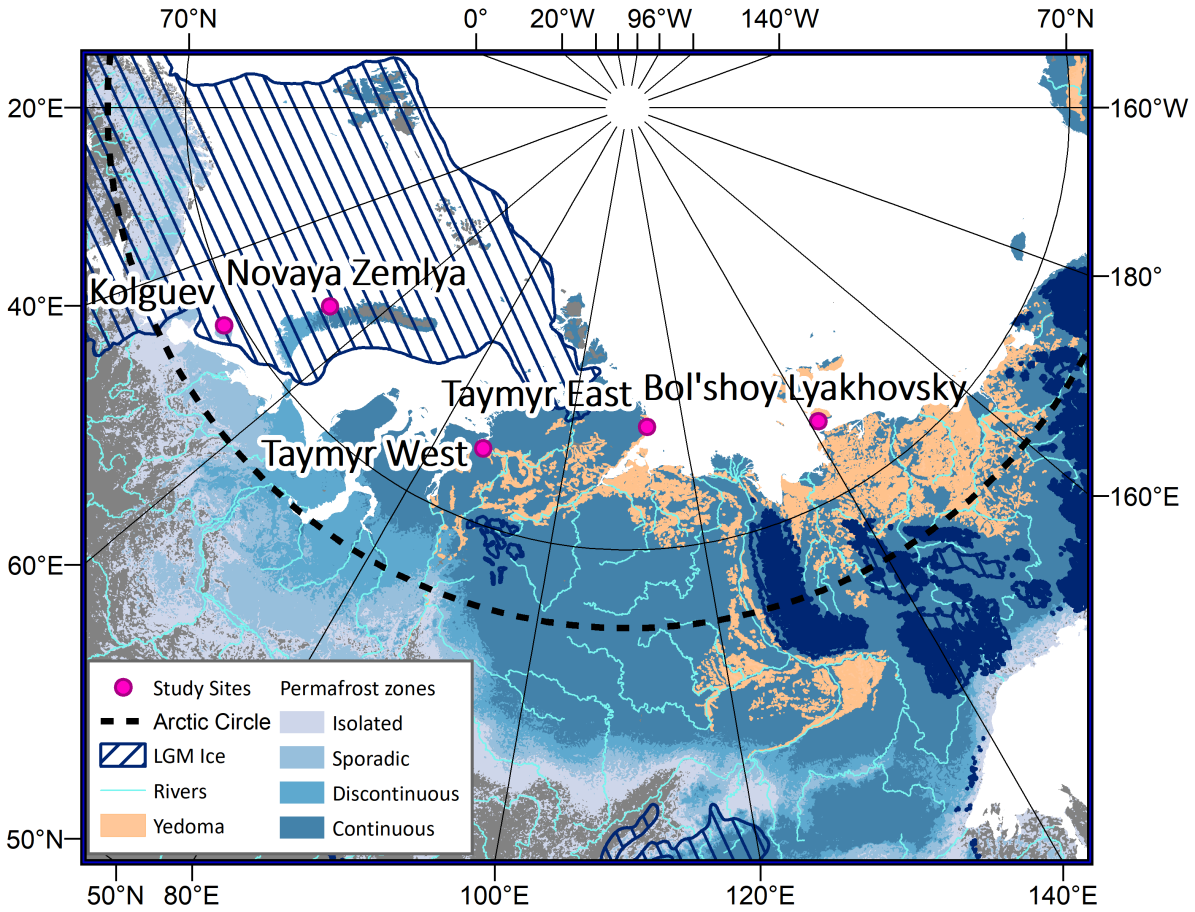

Figure 3.1: Map showing the location of the study sites in northern Russia. The permafrost zones are according to Obu et al. (2019), the Last Glacial Maximum (LGM) glaciation ice extent according to Ehlers & Gibbard (2003) and the Yedoma distribution according to Strauss et al. (2022).

The Kara, Barents, Laptev and East Siberian Sea – all extensions of the Arctic Ocean – surround the study sites and have a significant impact on the prevailing climate. According to the Köppen-Geiger climate classification, the entire study area belongs to the ET tundra climate class. This category describes regions in which at least one month has an average temperature of 0 °C, but in which no month exceeds the threshold of 10 °C in the annual average (Beck et al., 2018). Table 3.1 lists additional climatic information for all sites, including Mean Annual Air Temperature (MAAT) in July and January and Mean Annual Total Precipitation (MATP) as well as Mean Annual Ground Temperature and Vegetation class.

Just like the local climate itself, permafrost characteristics, such as ice content and organic matter content, vary throughout the study area. Nonetheless, it is important to note that all sites are located in regions which have seen recent reports of enhanced slump activity (Runge et al., 2022; Günther et al., 2013; Bernhard et al., 2022a). The High Arctic is particularly affected by global warming and the study sites are located in ice-rich permafrost, which in turn is especially prone to thawing.

During the LGM, both Kolguev Island and Novaya Zemlya Archipelago were covered with a dynamic ice sheet (Ehlers & Gibbard, 2003). In certain regions in this area, permafrost contains tabular ground ice and is relatively young when compared to Yedoma permafrost which is exposed in large parts of the Russian Arctic. The study sites on Taymyr are located south and southeast of a former ice sheet which covered the northeast of the peninsula during the last glaciation (Alexanderson et al., 2001). The sites are located in a zone shaped by buried glacial ice of pre-LGM moraines (Barr & Clark, 2012). The study site located on Bol'shoy Laykhovsky island lies within old, ice-rich permafrost of the Yedoma domain which formed during the late Pleistocene, where long-term syngenetic freezing and continuous sedimentation led to the formation of tall ice wedges embedded in organic rich, silt-dominated sediments (Strauss et al., 2017).

Kolguev and Bol'shoy Lyakhovsky are coastal sites: In the following, RTSs which were observed at these sites will be referred to as "coastal RTSs". RTSs observed at all other sites will be referred to as "non-coastal RTSs". Coastal RTSs differ from non-coastal RTSs in that they were initiated right at the coastline as part of the coastal erosion processes thermal abrasion and thermal denudation. These coastal RTSs form u-shaped depressions right at the coastline and regress inland over time. Non-coastal RTS, occurring primarily on

slopes and along lakeshores, were mapped at the study sites on Novaya Zemlya and Taymyr.

Table 3.1: Mean annual air temperature (MAAT) and mean annual total precipitation (MATP) are derived from ERA5 reanalysis data based on a 30km-grid from the time span 1981-2010, mean annual ground temperature at the top of the permafrost at 1 km spatial resolution after Obu et al. (2018), and vegetation class after Walker et al. (2005).

Study Site	Coordinates (centre)	MAAT (Jan) [°C]	MAAT (Jul) [°C]	MATP [mm]	MAGT [°C]	Tundra CAVM subzone
Novaya Zemlya	73.7 °N, 53.8°E	-13	3.6	723	1 to -2	A
South Kolguev	69.2 °N, 48.3 °E	-9.9	6.8	607	0 to 2	D
North Kolguev	69.2 °N, 48.5 °E	-8.5	5.6	627	0 to 2	D
Bol'shoy Lyakhovsky	73.4 °N, 141.2 °E	-31.8	5.9	246	-7 to -11	B
East Taymyr	75.5 °N, 113.4 °E	-30	3.9	331	-7 to -11	B
West Taymyr	73.2 °N, 87.2 °E	-29.3	8.7	398	-5 to -8	C,D

3.1 Coastal sites

3.1.1 Kolguev Island

Kolguev island is located off the coast of Arctic European Russia in the Barents Sea, separated from the mainland by the roughly 75 km wide Pomor Strait (Fig.3.1, (Glazov et al., 2021)). The island is characterized by sporadically distributed, ice-rich permafrost consisting of massive tabular ground ice deposits embedded in fine grained, sandy and clayey glacial sediments (Kizyakov et al., 2013). The origin of the tabular ice deposits is subject to a continued debate. Some studies argue that it formed through water migration under gradual freezing of the former sea floor, (Leibman et al., 2003) whilst others report that they originated from buried glacial ice of the Late Pleistocene (Streletskaya et al.,

2021).

The study site is located along the northwestern coast of Kolguev island and has been divided into two sections: The RTS of the southern section (Fig.3.2) are located around 3.0 km south of the Sauchiha river mouth along the northwestern coast of Kolguev, hereinafter referred to as South Kolguev, the RTS of the northern section (Fig.3.3) are located roughly 7 km north of it, hereinafter referred to as North Kolguev. The coastal zone is characterized by a gentle hilly landscape with steep bluff walls tens of meters high. Thermo-erosion such as thermo-abrasion and thermo-denudation greatly shape the coastal zone in this region, were thawing of the tabular ground ice results in the formation of thermo-cirques or thermoterraces (Kizyakov et al., 2013, 2019).

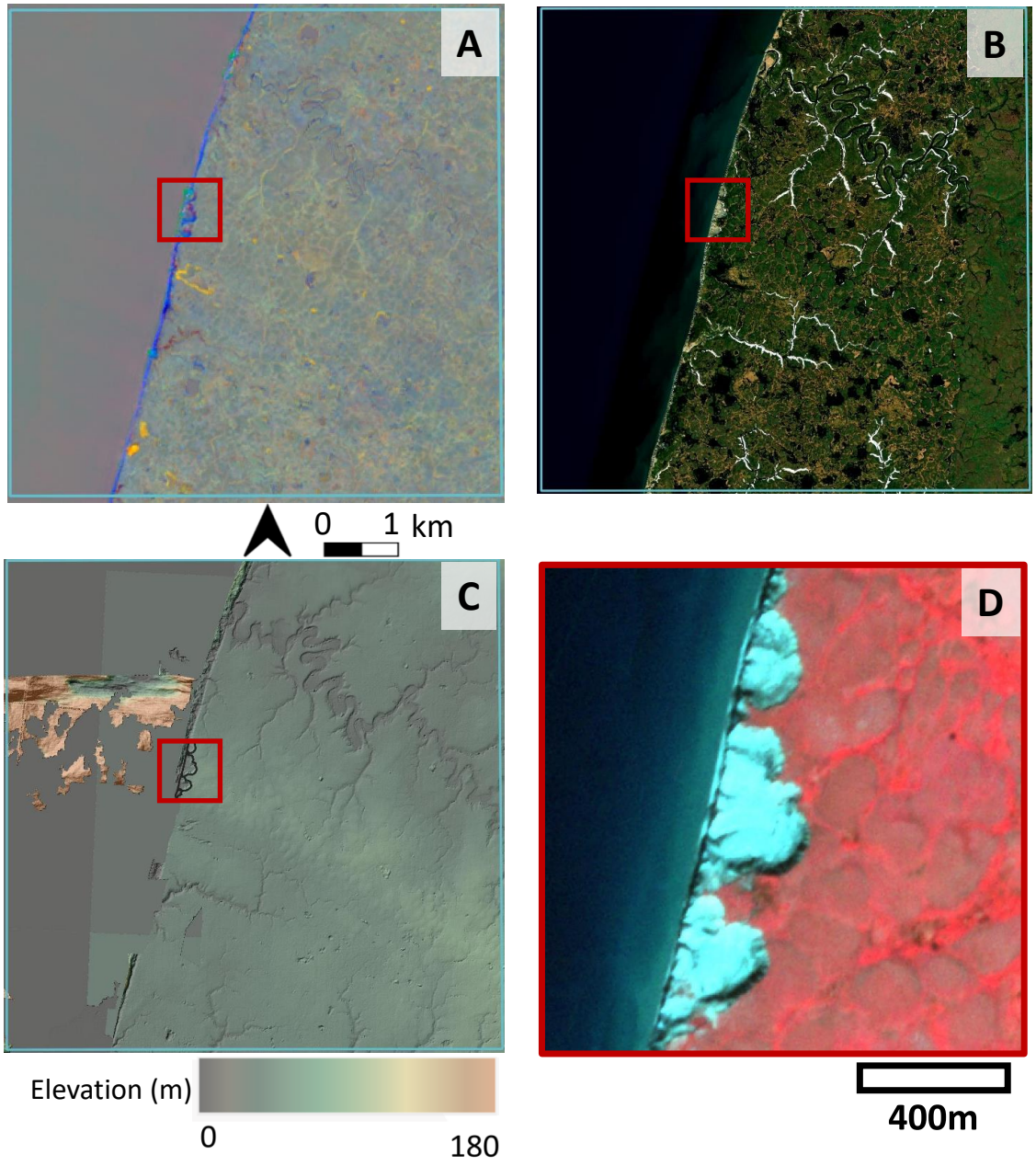

Figure 3.2: Study site South Kolguev. A: Tasseled Cap trend visualization, B: ESRI satellite layer (Esri World Imagery, 2009), C: ArcticDEM (Porter et al., 2018) superimposed with hillshade and overlaid with RTS object outlines of 2020, D: PlanetScope satellite image (NIR-R-G) acquired on 27.07.2020. Red box detailed view of D. Note partially missing ArcticDEM data in C.

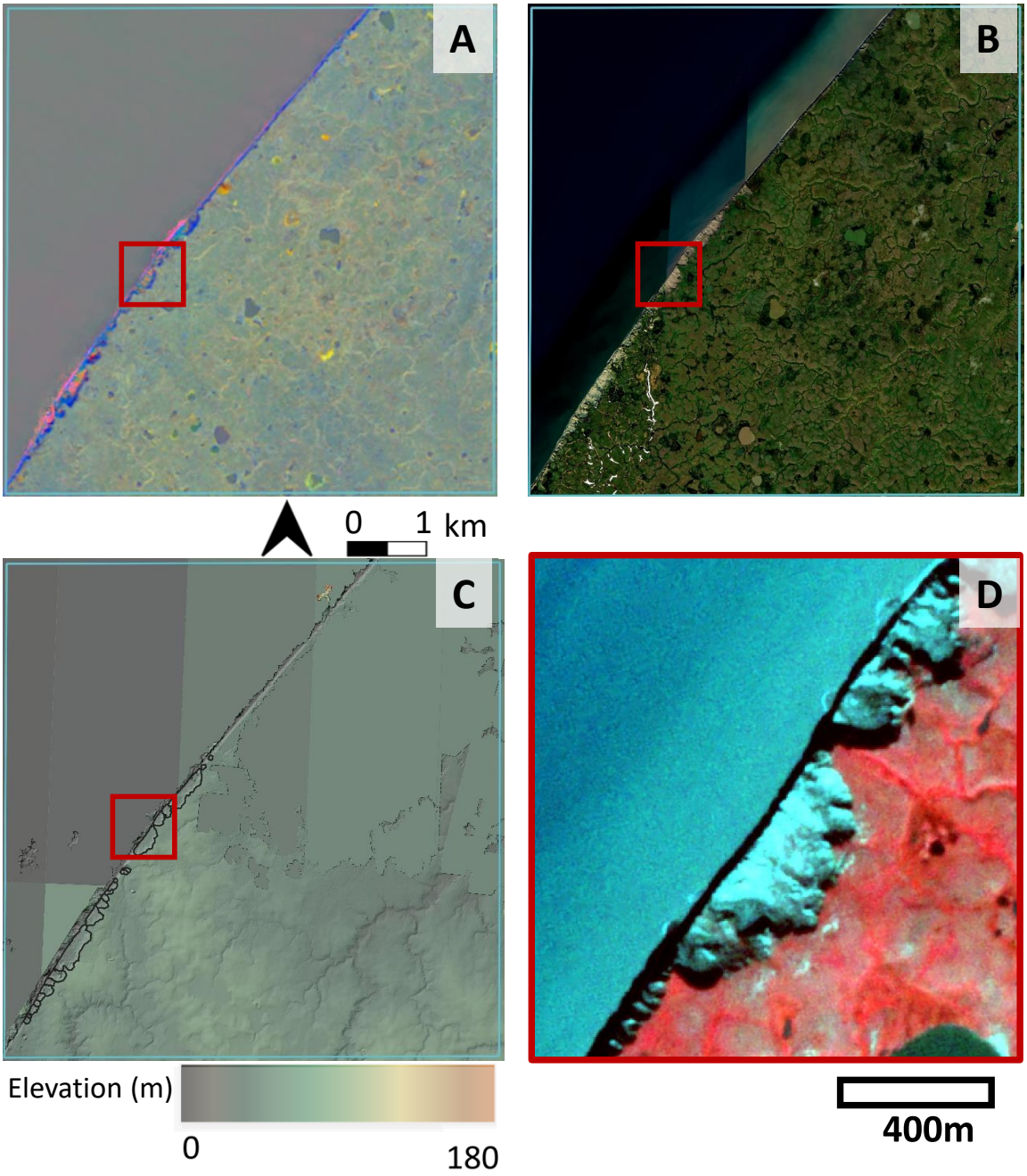

Figure 3.3: Study site North Kolguev. A: Tasseled Cap trend visualization, B: ESRI satellite layer (Esri World Imagery, 2009), C: ArcticDEM (Porter et al., 2018) superimposed with hillshade and overlaid with RTS object outlines of 2020, D: PlanetScope satellite image (NIR-R-G) acquired on 23.08.2020. Red box detailed view of D. Note partially missing ArcticDEM data in C.

3.1.2 Bol'shoy Lyakhovsky

Bol'shoy Lyakhovsky Island, located off the coast of Eastern Siberia between the Laptev Sea and the East Siberian Sea, is the southernmost island of the New Siberian Islands

(Fig.3.1). Located east of the active Gackel-Ust Lena rift zone, neotectonic activity plays an important role in the geological and sedimentary development of the island. The landscape is dominated by a smooth hilly terrain with a few local elevations reaching up to 300 m. Numerous thermo-erosional valleys and some thermokarst lakes shape the landscape (Andreev et al., 2009). The study site is located along the southern coast of the island, on a flat terrain, which has been strongly impacted by thermo-erosional processes (Fig.3.4). Thermo-cirques extend along large parts of the southern coast and result from the thawing of ice-rich permafrost deposits ((a) in Fig.2.3). The permafrost in this region is characterized by a Pleistocene ice complex, also called Yedoma permafrost, which consists of large syngenetic ice wedges embedded in silty fine sands and peat layers and the subsequently deposited marine sediments of the Holocene (Wetterich et al., 2019).

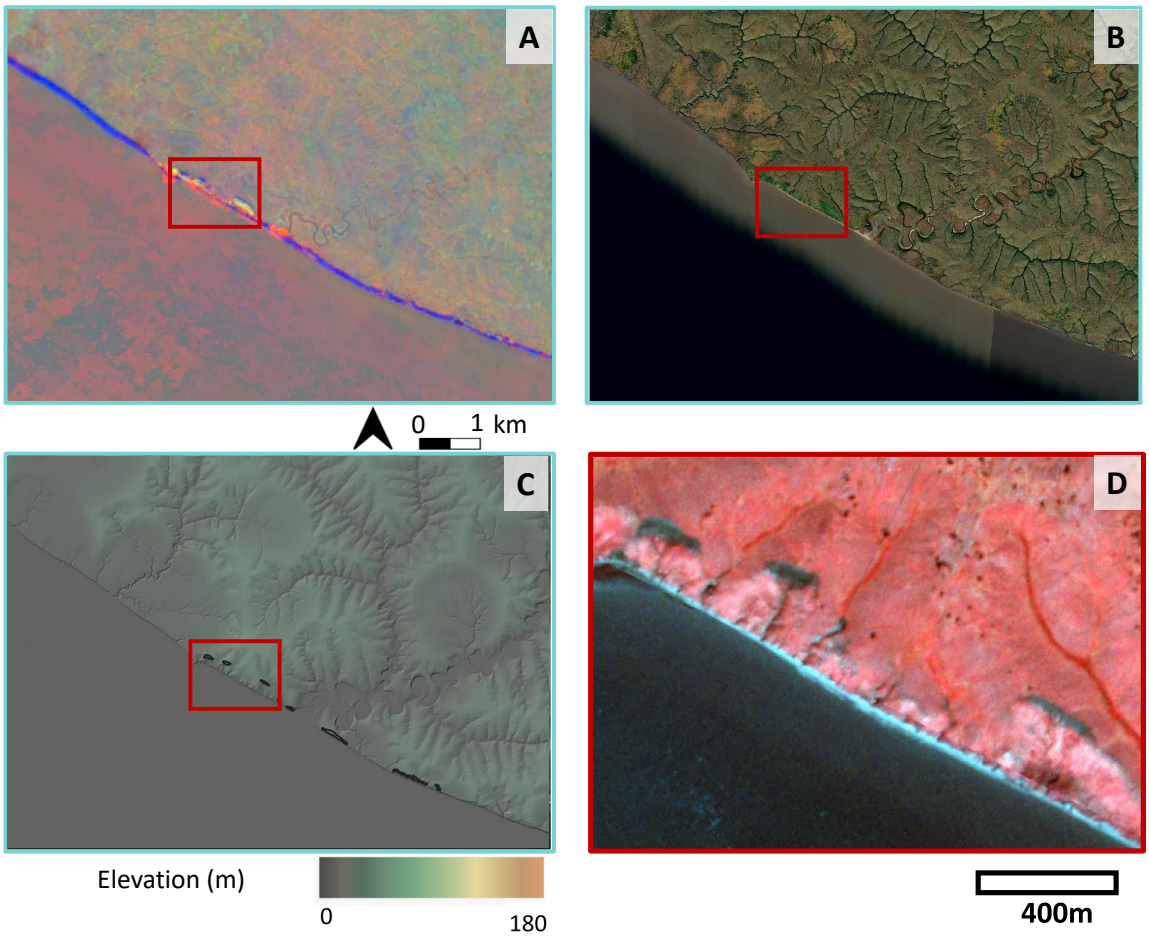

Figure 3.4: Study site Bol'shoy Lyakhovsky. A: Tasseled Cap trend visualization, B: ESRI satellite layer (Esri World Imagery, 2009), C: ArcticDEM (Porter et al., 2018) superimposed with hillshade and overlaid with RTS object outlines of 2020, D: PlanetScope satellite image (NIR-R-G) acquired on 13.07.2020. Red box detailed view of D.

3.2 Non-coastal sites

3.2.1 Novaya Zemlya

Novaya Zemlya archipelago is located northeast of Kolguev island off the coast of Arctic European Russia bound to the west by the advected warm North Atlantic water of the Barents Sea and to the east by the cold water of the Kara Sea which greatly affects the thermal regime of the islands (Fig.3.1). As a northern extension of the Ural Mountains, the landscape is dominated by mountainous terrain. Novaya Zemlya consists of two main islands, the northern Severny Island and the southern Yuzhny Island, which are separated by the Matochkin Strait. The Northern Island is largely covered by the Gory Mendeleyeva glacier. On Novaya Zemlya, mean annual temperature and precipitation vary greatly due to its large latitudinal span and marine environment. The West Coast, where the study site is located, is characterized by relatively mild and humid climate caused by the warm Atlantic waters transported by the Gulf Stream (Rusakov et al., 2022). Compared to the East Coast, the West Coast receives 600 mm more precipitation per year (Rusakov et al., 2022).

The study area is located on Sukhoy Nos, on the west coast of Severny Island, south of the Gory Mendeleyeva Glacier, on a projecting, very gently rolling terrain, with highest elevations of 80 m (Fig.3.5). Between 1958 and 1961, the USSR used the region for nuclear testing (Miroshnikov et al., 2017). Among the bombs detonated in this region is the Tsar Bomba, a record-breaking 50-megaton hydrogen bomb (Khan, 2020). At Sukhoy Nos, RTS ocurrence is widely spread, with slumps appearing close to lakes, channels and the coast. A large proportion of big slumps developed close to the coastlines of the study site. Unlike the coastal slumps, these slumps were triggered up-slope and as they grew, they intersected with the coast over time.

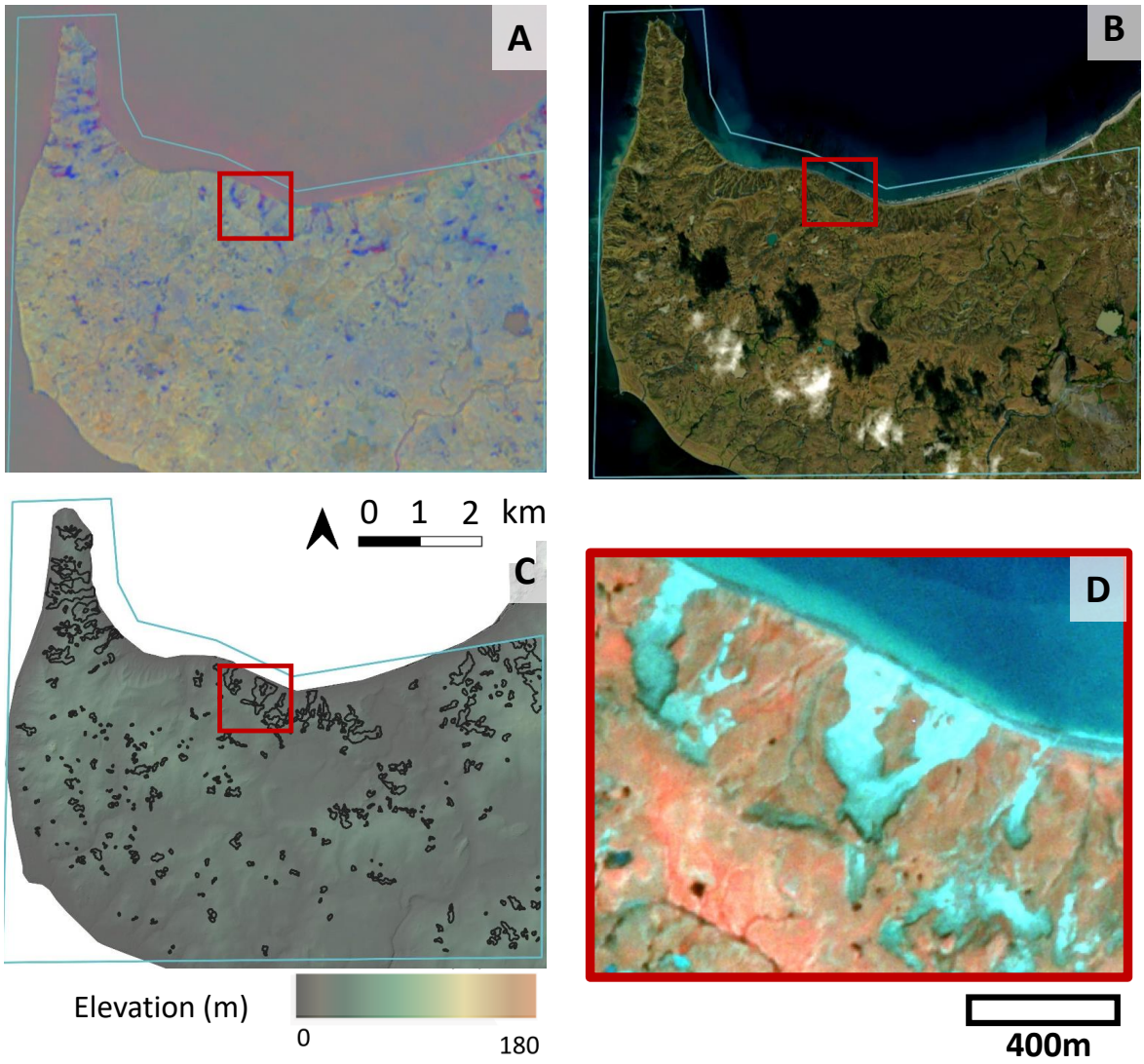

Figure 3.5: Study site Novaya Zemlya. A: Tasseled Cap trend visualization, B: ESRI satellite layer (Esri World Imagery, 2009), C: ArcticDEM (Porter et al., 2018) superimposed with hillshade and overlaid with RTS object outlines of 2020, D: PlanetScope satellite image (NIR-R-G) acquired on 22.07.2020. Red box detailed view of D.

3.2.2 Taymyr Peninsula

Located between the bays of the rivers Yenisey and Khatanga, Taymyr Peninsula separates the western Kara Sea from the eastern Laptev Sea and forms the northernmost part of the Eurasian mainland (Fig.3.1). During the LGM, the northwest of Taymyr was covered by ice sheets (Alexanderson et al., 2001). The surrounding area has been affected by pre-LGM glacial moraines, which shaped large parts of the region (Barr & Clark, 2012). The permafrost in this area is characterized by buried glacial moraine ice deposits. After Strauss et al. (2017), both study sites are located within close proximity to Yedoma

deposits.

3.2.2.1 West Taymyr

The study site on West Taymyr is located near the Pyasina river delta . The landscape is characterized by numerous smaller and several larger lakes which are surrounded by a gentle rolling terrain with hills reaching up to 180 m (Fig.3.6). RTSs here are mainly located along lake shores, with several (up to 15) slumps per lake.

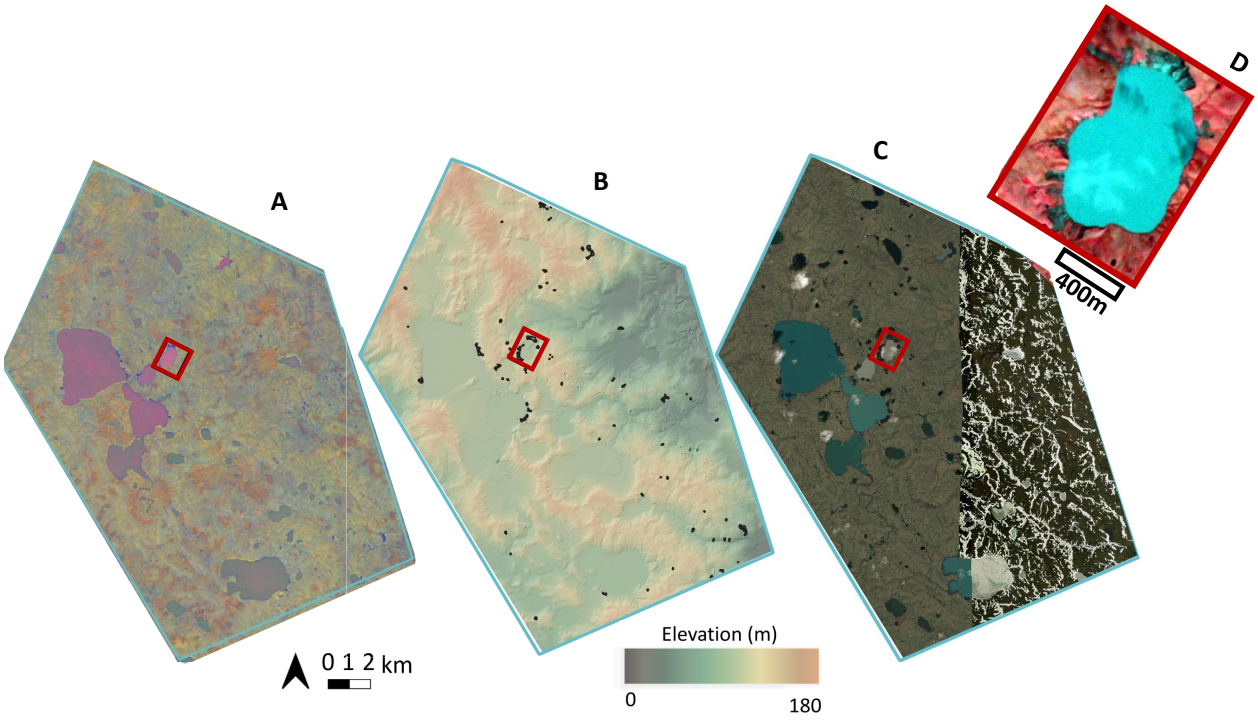

Figure 3.6: Study site West Taymyr. A: Tasseled Cap trend visualization, B: ESRI satellite layer (Esri World Imagery, 2009), C: ArcticDEM (Porter et al., 2018) superimposed with hillshade and overlaid with RTS object outlines of 2020, D: PlanetScope satellite image (NIR-R-G) acquired on 21.08.2020. Red box detailed view of D.

3.2.2.2 East Taymyr

The study site located close to the eastern coast of Taymyr Peninsula, is situated in an area characterized by a few larger lakes which are surrounded by relatively smooth relief with hills reaching up to 120 m (Fig.3.7). Most of the RTS occurred along the slopes close to the lake shores. However, in many cases they didn't originate directly at the shoreline as is the case for West Taymyr.

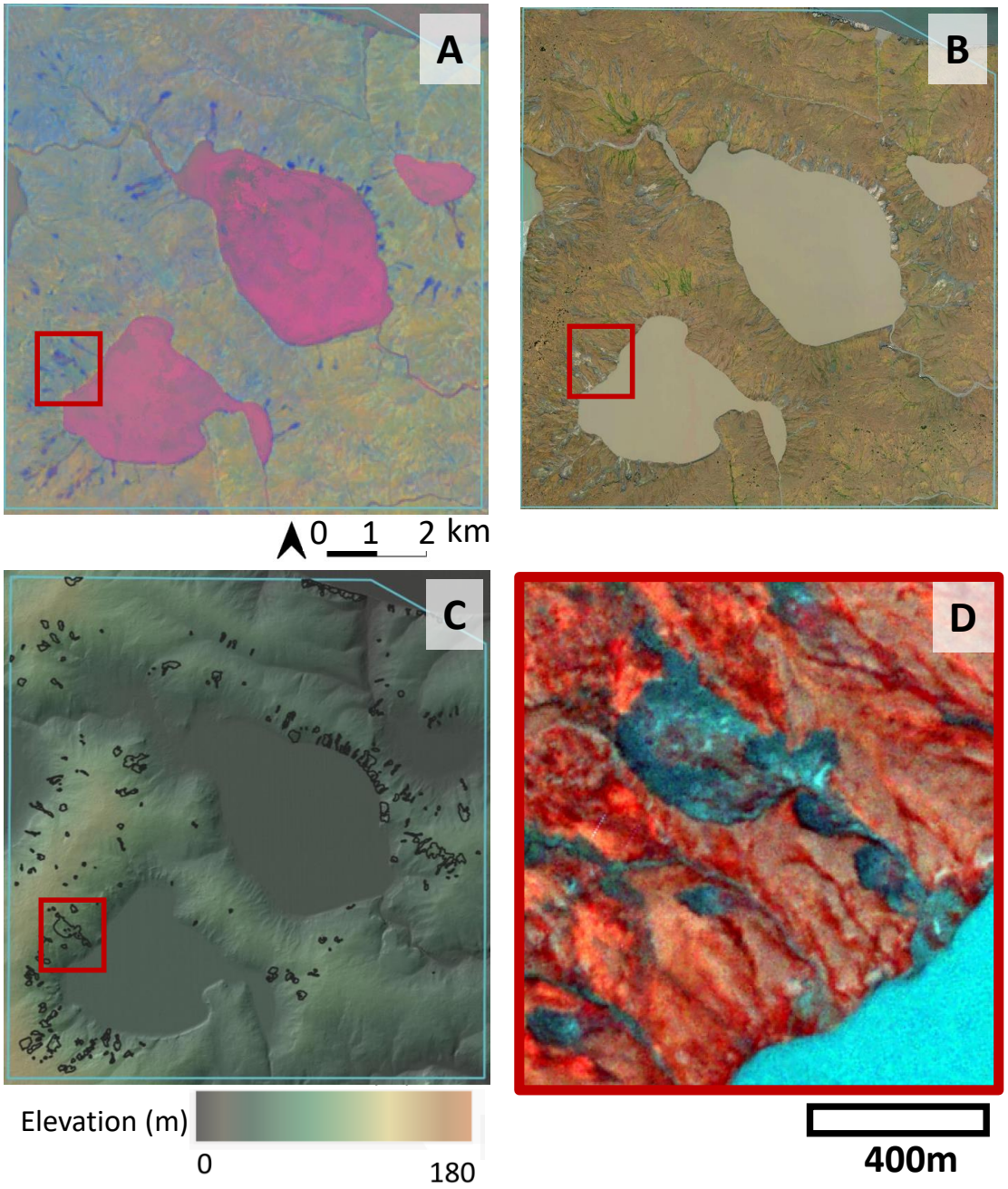

Figure 3.7: Study site East Taymyr. A: Tasseled Cap trend visualization, B: ESRI satellite layer (Esri World Imagery, 2009), C: ArcticDEM (Porter et al., 2018) superimposed with hillshade and overlaid with RTS object outlines of 2020, D: PlanetScope satellite image (NIR-R-G) acquired on 14.08.2020. Red box detailed view of D.

4 Data and methods

4.1 Data

A variety of data sets were composed to obtain the RTS inventory. Primarily, I used high resolution satellite imagery to map RTS. Additionally, I included the ESRI satellite base map (Esri World Imagery, 2009), the ArcticDEM (Porter et al., 2018) and Tasseled Cap Landsat Trends (Nitze & Grosse, 2016; Nitze et al., 2018) for the period between 2000 and 2019 in the data set.

4.1.1 Very high-resolution satellite imagery

Multi-spectral optical data of the satellite constellations PlanetScope and RapidEye were compiled between 2013 and 2020 to create time series of the individual study sites. The image collections were filled with spatially very high resolved, pan-sharpened images of Pléiades and SPOT (6 and 7), acquired between 2011 and 2019. Each of the sensors is equipped with four spectral bands in the visible (red, green, blue; RGB) and near-infrared (NIR) wavelengths that assist in landscape interpretation. The RapidEye sensor additionally provides a band in the Red edge wavelengths. The spatial resolution of the data collection ranges between 0.5 m of the Pléiades images to 5 m of the RapidEye images (Table 4.1,4.2). All imagery used in this study had previously undergone radiometric, sensory and geometric correction and was georeferenced by the suppliers before use (see earth.esa.int/eogateway/catalog for additional information of the data products). For more detailed information, see Table A0.1 in the appendix which lists each single image ID with the corresponding satellite sensor and additional information for the data used in this inventory.

The availability of suitable imagery is highly limited in the northern high latitudes due to long snow periods and frequent cloud cover. Additionally, low sun elevations in high-latitude environments can lead to low signal-to-noise ratios. Therefore, the image selection was restricted by several factors, including cloud and snow cover, shadows, and insufficient image resolution. Images were selected based on the absence of clouds (less than 10% in most cases) and throughout the snow-free summer months (July to August). Because RTS are small-scale features, mapping these landforms requires imagery with very high spatial

resolution, which in most cases is not freely available and was collected less frequently in earlier years (prior to 2013) compared to imagery with lower spatial resolution (such as Sentinel, Landsat, etc.), which further limits the time series. For most study sites, images were available between 2013 and 2020, for each or every second year. The two exceptions to this are the study sites on Bol'shoy Lyakhovsky and East Taymyr: In these cases, image collections are available from 2011 to 2020, with a four-year image gap between 2011 and 2016 (Table 4.2). Surface reflectance data from the PlanetScope and RapidEye sensors were downloaded via the Planet Explorer interface from Planet Teams (https://api.planet.com). SPOT and Pléiades images were made available through the ESA third-party application.

Table 4.1: Very high-resolution satellite image data collection for each site respectively. RE = RapidEye, PS = PlanetScope, S = SPOT (6 and 7), P = Pléiades.

Site	Aquisition year	Sensor	Res.	Spectral bands
Novaya Zemlya	2013, 2016	RE	5 m	RGB+Red edge+NIR
	2018, 2020	PS	3 m	RGB+NIR
	2019	S	1.5 m	RGB+NIR
	2016	P	0.5 m	RGB+NIR
East Taymyr	2011, 2016	RE	5 m	RGB+Red edge+NIR
	2016, 2018, 2019, 2020	PS	3 m	RGB+NIR
	2017	S	1.5 m	RGB+NIR
West Taymyr	2013, 2015	RE	5 m	RGB+Red edge+NIR
	2018, 2019, 2020	PS	3 m	RGB+NIR
	2017	S	1.5 m	RGB+NIR
Bol'shoy Lyakhovsky	2011	RE	5 m	RGB+Red edge+NIR
	2018, 2019, 2020	PS	3 m	RGB+NIR
	2016, 2017	S	1.5 m	RGB+NIR
North Kolguev	2013, 2015	RE	5 m	RGB+Red edge+NIR
	2018, 2019, 2020	PS	3 m	RGB+NIR
	2016, 2017	S	1.5 m	RGB+NIR
South Kolguev	2013, 2015	RE	5 m	RGB+Red edge+NIR
	2018, 2019, 2020	PS	3 m	RGB+NIR
	2016, 2019	S	1.5 m	RGB+NIR

Table 4.2: Acquisition steps of the very high-resolution satellite image data collection for each site respectively.

Site	2011	2012	2013	2014	2015	2016	2017	2018	2019	2020
Novaya Zemlya			x			x		x	x	x
East Taymyr	x					x	x	x	x	x
West Taymyr			x		x		x	x	x	x
Bol'shoy Lyakhovsky	x					x	x	x	x	x
North Kolguev			x		x	x	x	x	x	x
South Kolguev			x		x	x		x	x	x

4.1.2 ArcticDEM

The ArcticDEM, version 3.0 Pan-Arctic (Porter et al., 2018) provides high quality elevation data in all land area north of 60°N (except for minor data gaps). It is produced by very high-resolution optical imaging satellites of the Maxar constellation. The 2 m resolution ArcticDEM mosaic (version 3, Google Earth Engine Dataset: "UMN/PGC/ArcticDEM/V3/2m_mosaic") was used to calculate detrended elevation and slope maps in GEE. Since RTSs mostly occur along hillslopes, the topographic information extracted from the ArcticDEM was used to support the mapping process. In later stages of the analysis, the ArcticDEM mosaic raster file was separately downloaded, clipped and reprojected respectively to the location of the surveyed sites in QGIS 3.10. and used to extract local terrain characteristics such as slopes.

4.1.3 Tasseled Cap Landsat Trends

The temporal trend data sets of Tasseled Cap indices (brightness (TCB), greenness (TCG), and wetness (TCW)) of Landsat Data (Collection 1, Tier 1, Surface Reflectance), calculated and described in previous work of Nitze & Grosse (2016); Nitze et al. (2018) and Nitze et al. (2021), were used to identify active RTS. The Tasseled Cap Landsat Trends calculated in GEE were visualized in QGIS 3.10. through the Google Earth Engine Plugin ("users/ingmarnitze/TCTrend_SR_2000-2019_TCVIS"). The data set consists of selected cloud less (< than 70% cloud coverage), snow/ice, cloud and shadow masked

Landsat scenes for the period between 2000 and 2019. Amongst others, Tasseled Cap Landsat trends are useful to detect rapid disturbances (Nitze et al., 2018). Illustrated by image subset B2 in Figure4.1, active pulse disturbances such as RTS show up as blue features on the TCVIS layer.

4.1.4 ESRI satellite basemap

The publicly available very high resolution imagery in ESRI satellite base layers (Esri World Imagery, 2009), (Table4.3) was accessed and used for mapping through the QuickMapServices Plugin in QGIS 3.10. (https://github.com/nextgis/quickmapservices).

Table 4.3: ESRI satellite basemap scenes for each site respectively. WV02 = WorldView-2, WV04 = WorldView-4, QB02 = QuickBird-2.

Site	Aquisition date	Sensor	Resolution
East Taymyr	02/08/2021	WV02	0.5 m
West Taymyr	17/07/2015	WV02	0.5 m
	17/06/2021	WV02	0.5 m
Novaya Zemlya	08/25/2012	QB02	0.6 m
Kolguev South	07/05/2017	WV04	0.31 m
Kolguev North	07/05/2017	WV04	0.31 m
	07/04/2016	WV02	0.5 m

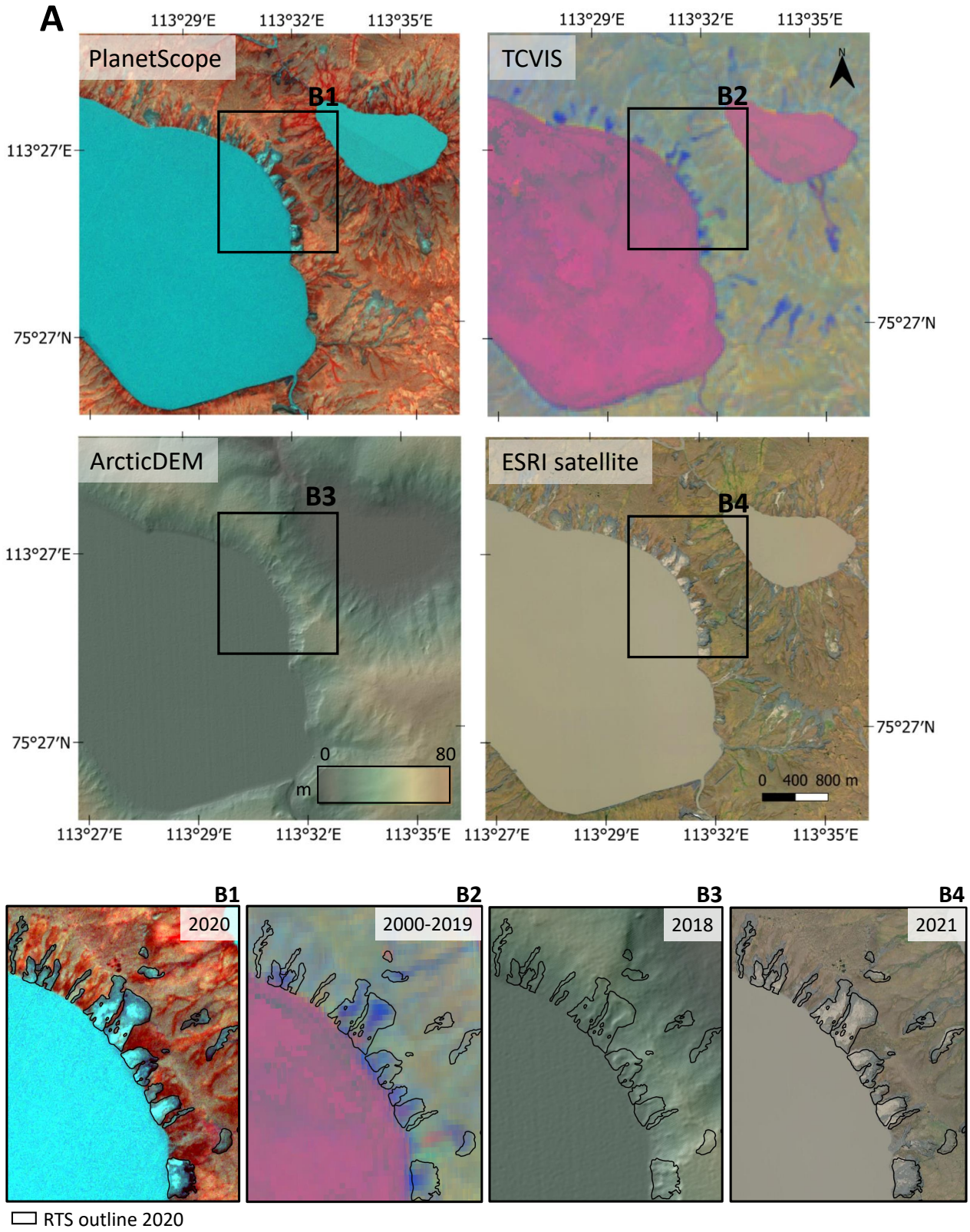

Figure 4.1: Map showing the different data sets used in this inventory, located on a subsection of the East Taymyr study site (A); B1: PlanetScope image subset of 14.08.2020, B2: Landsat Trend data subset, B3: ArcticDEM (Porter et al., 2018) subset superimposed with hillshade, B4: ESRI satellite subset Esri World Imagery (2009). Note that the B1-B4 had been overlaid with RTS object outlines of 2020.

4.2 Methods

Spatial data analysis was mainly performed in ArcMap 10.5 and QGis 10.3. Additional data processing and plotting was done in Python 3.8.8.

4.2.1 Image processing

Before I started the actual mapping process, image processing steps were performed in Python. In a first step, I merged all related single image scenes of one year together. In combination, they fully encompass the respective study site to image mosaics. In a next step, image co-registration was applied to account for positional inaccuracies between the individual satellite image mosaics.

4.2.1.1 Image co-registration

As described above, all satellite images were provided as georeferenced datasets. However, even after orthocorrection, there were still alignment errors of up to a few meters between the individual satellite images. It is crucial to account for misalignment when working with time series, as positional inaccuracies can largely affect the reliability of change detection calculations. To account for inter-image shifts, image co-registration was applied after merging the image scenes. Image co-registration matches two or more images geometrically so that corresponding pixels, representing the same objects, align as closely as possible. I used the global method of the automated, open-source image co-registration software AROSICS (Scheffler et al., 2017) which works on a Python base. The software uses phase correlation, an intensity-based registration technique, as the core technology to detect sub-pixel displacements. Using the global method, a small subset of the image is created to compute a X/Y translation vector. The information of the sub-pixel shifts is then applied to the metadata of the output image. Sub-pixel shifts were estimated based on formulas 1 and 2, where v(0,0) represents the value of the refreshed cross power spectrum at the peak position and v(1,0) and v(0,1) represent the direct neighbours in X- and Y-direction:

$$\delta x = \frac{v(1,0)}{v(1,0)v(0,0)}$$

$$\delta y = \frac{v(0,1)}{v(0,1)v(0,0)}$$

The co-registration process was performed for each site separately. The software offers the possibility to set the individual parameters separately, which allows specifying the parameters according to the image data set. First, the reference and target images were defined. I used the most recent available image as the reference image, this was the 2020 image for all sites, so the target images represented by all remaining images of a site were shifted according to the 2020 image. The window size of the image subset was set to 600 x 600 pixels. I kept the window position, which was set by default to the central position of the image overlap. I increased the maximum shift distance parameter, which is in reference image pixel units to 20 to include single images with exceedingly large shifts. To compress my data lossless I used the compression method 'Deflate' in the GDAL creation options parameter. Additionally, I defined the NIR band of the reference image and the target image as the band from which to calculate the displacement. To validate the image match, the structural similarity index (SSIM) was calculated before and after calculating the shift correction. The SSIM measures the difference in perception between two similar images. If the SSIM was higher after co-registration, the target image was shifted, if it was lower, the target image was kept in place. In case the satellite images came with auxiliary files, like cloud masks, I applied the corresponding shift to them as well.

4.2.2 Manual mapping of active RTS

To investigate changes in active RTS numbers and extent over time, a GIS-based inventory of manually mapped RTS was created. The Tasseled Cap Trend product, the ArcticDEM, the ESRI satellite basemap, and the preprocessed satellite mosaics were loaded into QGIS 3.10., with satellite imagery visualized in NIR, Red, and Green false-color schemes to more clearly distinguish between vegetated areas (red) and non-vegetated areas such as bare ground and water bodies (light blue).

An RTS identification and mapping procedure, consisting of three main steps, was developed. As a first step, I examined the Landsat trend product to get an overview over fast disturbances in my study area. RTS that were active between 2000 and 2019 appear as blue features on the trend product (see B2 in Fig.4.1). Other rapid land-to-water surface changes (e.g. floodings), may also appear as blue features on the TCVIS layer. Therefore,

as a second step, I took a closer look at the ERSI satellite map and the ArcticDEM to verify that the blue features appearing on the trend product are an actual result of RTS activity. Since RTSs are slope features, the identification process can benefit from projecting the location of a previously identified slump onto an elevation model. This is where the ArcticDEM comes in (see B3 in Fig.4.1). Additionally, very high spatially resolved imagery, like the ERSI satellite base layer are useful to identify characteristic features of RTS (see B4 in Fig.4.1). On the lower resolution satellite imagery and the even coarser resolution Landsat trend data, these features are much more difficult, if not impossible, to detect, especially for small RTS.

In a third step, using the information from previous steps, I eventually identified and mapped every individual active RTS on the VHR satellite images for each time step, respectively. The RTS identification was based on typical characteristics of slump activity (see detailed description above; 2.2.1.1 Retrogressive Thaw Slumps). An important indicator of active slumps were the steep headwalls, which in many cases casted dark shadows on the satellite images . Slurry scar zones and dynamic slump floors, often including incised gullies, were additional characteristics of slump activity used in the identification process. These slump features are non-vegetated and thus show up on the satellite images in blueish-green when visualized in a false color scheme (see B1 in Fig.4.1). After identification, the extent of active slumps was mapped as polygon vector shapefiles based on the individual satellite images of the different years. From the mapped slumps, numbers and areal extents were calculated. The extent of RTS has been variously defined and mapped in previous studies; some studies included stable RTS in their inventory (Ramage et al., 2017). In this study, I focused only on the non-vegetated, active slump zones, excluding debris tongues and inactive slump parts.

4.2.3 Analysis of RTS characteristics

4.2.3.1 Terrain assessment

Slope and aspect maps were created for all sites to provide an overview of the preferred slope orientation and angle on which RTS occurred. The ArcticDEM mosaic raster file was loaded into QGIS 3.10., clipped and reprojected respectively to the location of the investigated sites and used to extract the slope aspects and angles. Then, centroids of the

RTS polygon vector files were created and for each of them, the corresponding aspect, slope and elevation values were extracted. The resulting data was then uploaded as a CSV file into Python, further edited and plotted.

4.2.3.2 Bluff and headwall erosion

For the coastal RTSs, change distances from headwalls and bluffs were calculated in ArcMap 10.5, using the Digital Shoreline Analysis System (DSAS) tool version 5 over the time period studied (2011/2013-2020) (DSAS, 2018). Before the calculations were performed, all coastal polygon vector shape files created in the previous step were transferred into line vector shape files. Then, the date of the corresponding satellite image was assigned to the line shape files. Afterwards, the line shapefiles were clipped, so that two separated lines appeared, representing the bluff and the headwall of the slump, respectively. Finally, all headwall line shape files of the different years were merged and imported as single feature class into a new geodatabase. The same procedure was applied to the bluff line shape files. To accelerate this process, I automated the process by creating a simple model using Arcmap ModellBuilder. After bringing the data into the right shape, I created a baseline shape file which was used as a reference line. Rates of change were then calculated for headwalls and bluffs, each based on the reference baseline. A transect was created every 10 m, for which the change in distance was calculated. To best fit the transects, I set the smoothing distance to 450 m for Kolguev and 100 m for Bol'shy Lyakhovsky. For verification purpose, I manually checked all transects before calculations were performed and deleted single transects which clearly did not follow the bluff and headwall movement directions. The net change distance (in m) was than calculated using the DSAS tool. Additionally, from the net change distances, yearly change rates (m/yr) were calculated for the respective study period which ranged from 2011 at Bol'shoy Lyakhovsky and 2013 at Kolguev to 2020. This procedure was performed for both, bluff and headwall.
In this study, the change rate is defined as the summed horizontal change distance in meter that the headwall or bluff base moved per year in the investigated period. Headwall and bluff are dominated by negative change rates, meaning that they reveal overall erosion. In most cases, more than 90% of the transects revealed negative rates associated with erosion.

4.2.3.3 Temperature and precipitation analysis

ERA5-Land Monthly (Muñoz Sabater, J., 2019) data were used to analyze summer and winter temperature means and ERA5 Daily Aggregates (C3S, 2017) were used to analyze total monthly precipitation and long term temperature and precipitation anomalies. The noaaplotter was used to plot temperature and precipitation anomalies and total monthly precipitation compared to 1981-2010 climate normals (https://github.com/initze/noaaplotter). All data were accessed in Google Earth Engine and processed and visualized in Python.

5 Results

5.1 RTS characteristics

To better understand local RTS development rates and distribution pattern throughout the last decade, I mapped RTSs at five selected study sites. The study included a total area of 627 km^2 affected by strong RTS development, while the extent of the individual study sites ranged between 55 and 272 km^2.

Table 5.1 summarizes the amount and mapped areal extent of identified RTSs per study site. Significantly more RTSs were found at non-coastal sites than at coastal sites. However, coastal slumps affect relatively large areas despite their small number. At Novaya Zemlya, 329 individual RTSs were observed in 2020, affecting an area of 353 ha. In the same year, at West Taymyr, a total of 108 RTSs were counted making up 67 ha and at East Taymyr, 254 RTSs were counted making up 196 ha. At Kolguev, 27 individual slumps were counted in 2020, affecting 129 ha, of these, 3 slumps, affecting 19 ha were observed along the southern study section. At Bol'shoy Lyakhovsky, 11 active slumps affected around 10 ha in 2020.

The normalized area frequency plot in Figure 5.1 shows that the majority of the slumps are rather small. About 50% of all mapped RTSs are smaller than 0.32 ha and about 90% are smaller than 1.95 ha. Exceptionally larger slumps, so called mega slumps, are rare. Some of the largest slumps were observed at North Kolguev (largest slump: 27.8 ha in 2020), Novaya Zemlya (largest slump: 19.7 ha in 2020) and Taymyr East (largest slump: 14.6 ha in 2020). The mean size of observed RTSs at the five sites range between 0.3 (at Novaya Zemlya in 2013) to 4.8 ha (at North Kolguev in 2020) (Fig.5.2).

Table 5.1: RTS and Study Site characteristics

Study site and respective size	Site/RTS characteristics	RTS Number in 2020	RTS extent in 2020 (in ha)	relative RTS extent per study area in 2020 (%)
Novaya Zemlya (55 km^2)	buried glacial ice, continuous permafrost, RTSs on hillslopes	329	353	6.43
Kolguev (132 km^2)	tabular ground ice, sporadic permafrost, coastal RTSs	27	129	0.98
Bol'shoy Lyakhovsky (77 km^2)	Yedoma permafrost, continuous permafrost, coastal RTSs	11	10	0.13
East Taymyr (91 km^2)	buried glacial moraine ice, Yedoma domain, continuous permafrost, RTSs on lakeshore & hillslopes	254	196	2.15
West Taymyr (272 km^2)	buried glacial moraine ice, Yedoma domain, continuous permafrost, RTSs on lakeshore	108	67	0.24

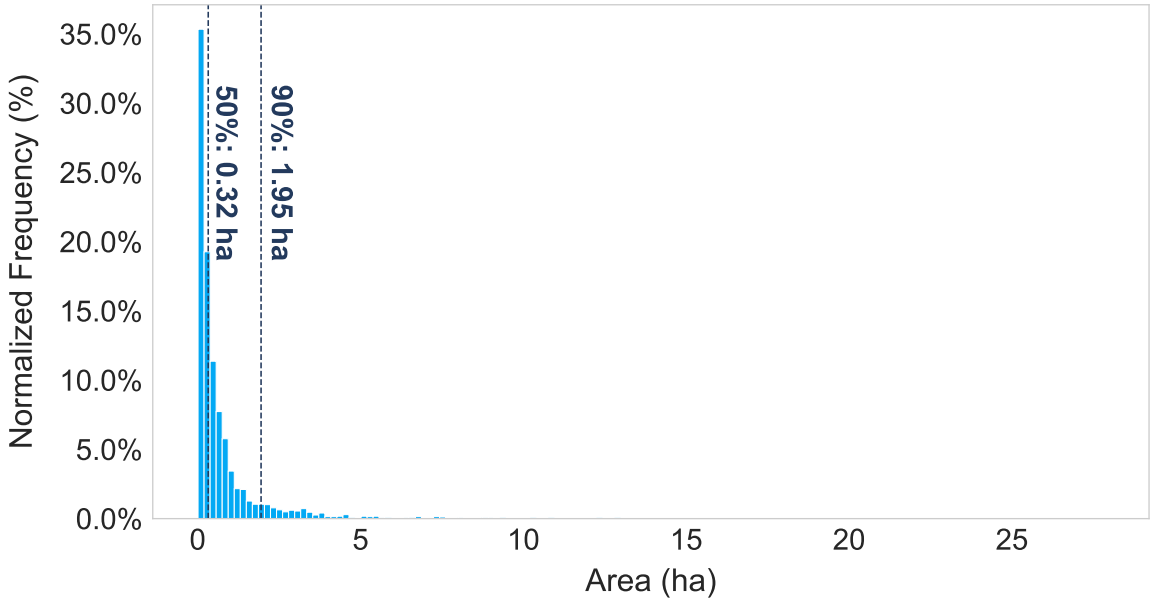

Figure 5.1: Normalized Frequency of individual RTS object sizes in percent for all sites and time steps.

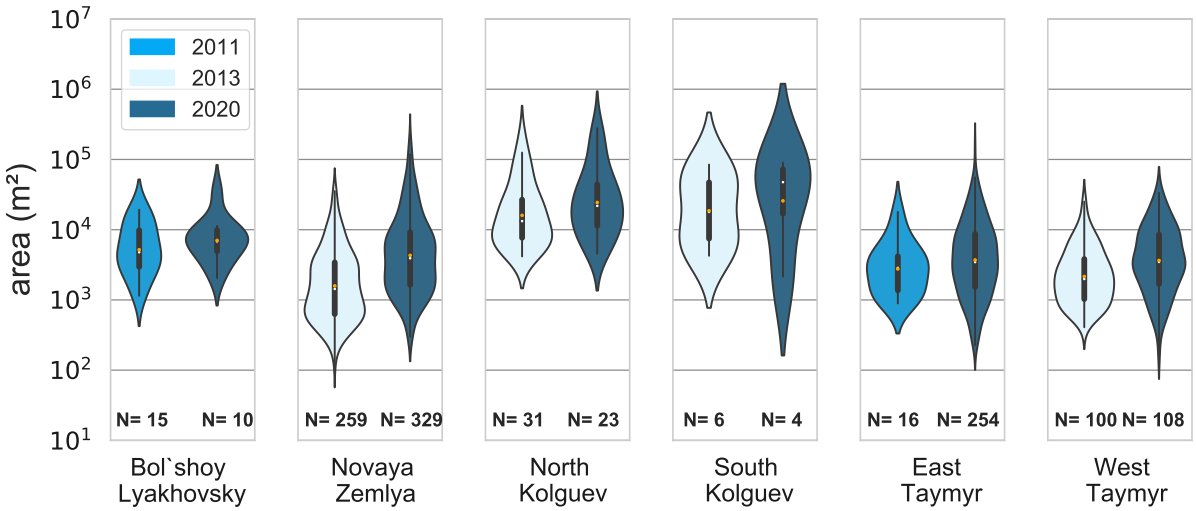

Figure 5.2: RTS object size distribution for the earliest (2011/2013) and latest (2020) year of the time series, for each site respectively. The orange dots represent mean and the white dots median values. The RTS number per year is given by N. Note that to better illustrate the data, the area is in meter and on a logarithmic scale.

The slope and elevation assessment showed that the majority of slumps occur below 50 m a.s.l.. West Taymyr is the only site were slumps occur at higher elevations, on average at 100 ma.s.l.. In addition, most of the RTSs were found in sloped terrain of 2-7 °(more than 55%). As an exception, RTSs observed at the West Coast of Kolguev were found on

steeper terrain with a mean slope of 12 ° (South Kogluev) and 19 ° (North Kolguev). At Novaya Zemlya, most of the area covered by RTSs in 2020 occurred on slopes facing west and northwest. A smaller percentage was observed on northeast facing slopes and none on slopes facing towards the south (Fig.5.3). At East Taymyr the majority of RTSs are located surrounding two larger lakes, a preferred slope direction is not clearly identifiable. The largest portion of RTS-affected area in 2020 was located on slopes facing towards the North and the South-East (Fig.5.4). Similarly, at West Taymyr RTSs occurred mainly surrounding lakes. Most of the area affected by RTSs in 2020 occurred along the northeastern shores of lakes, on slopes facing southwest (Fig.5.5). At the coastal sites, all slumps are facing towards the ocean. At Kolguev, slumps occurred on west and northwest oriented slopes of the West Coast. At Bol'shoy Lyakhovsky, slumps occurred on the southwest oriented slopes of the southern coast of the island.

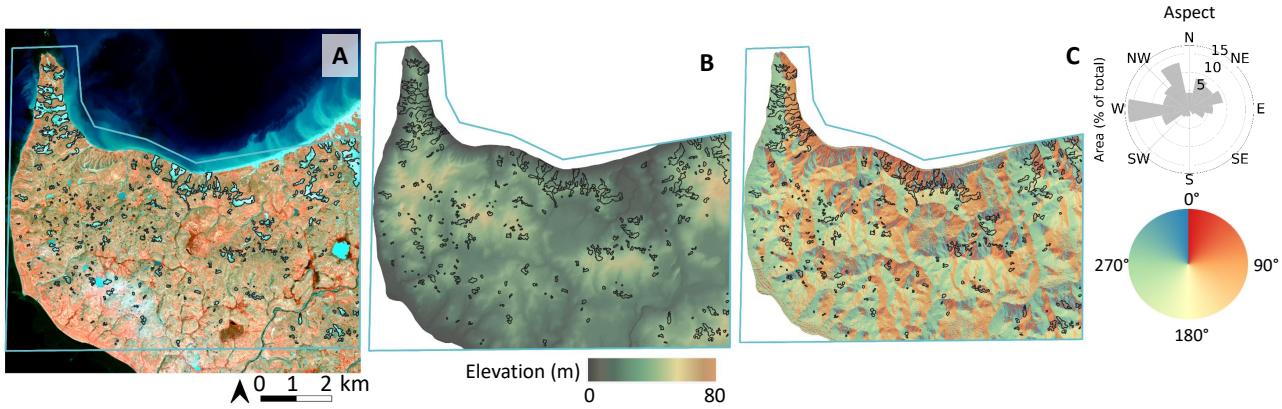

Figure 5.3: Study site Novaya Zemlya (Sukhoy Nos) with RTS object outlines of 2020. A: PlanetScope satellite image (NIR-R-G) acquired on 22.07.2020, B: ArcticDEM (Porter et al., 2018) superimposed with hillshade, C: slope map derived from ArcticDEM with RTS slope aspect plot weighted by RTS area.

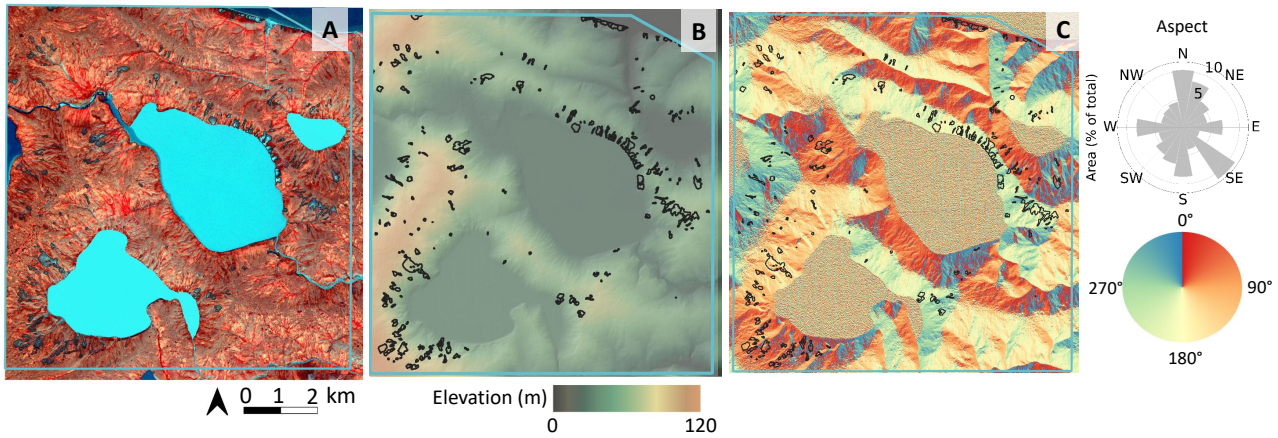

Figure 5.4: Study site East Taymyr with RTS object outlines of 2020. A: PlanetScope satellite image (NIR-R-G) acquired on 14.08.2020, B: ArcticDEM (Porter et al., 2018) superimposed with hillshade, C: slope map derived from ArcticDEM with RTS slope aspect plot weighted by RTS area.

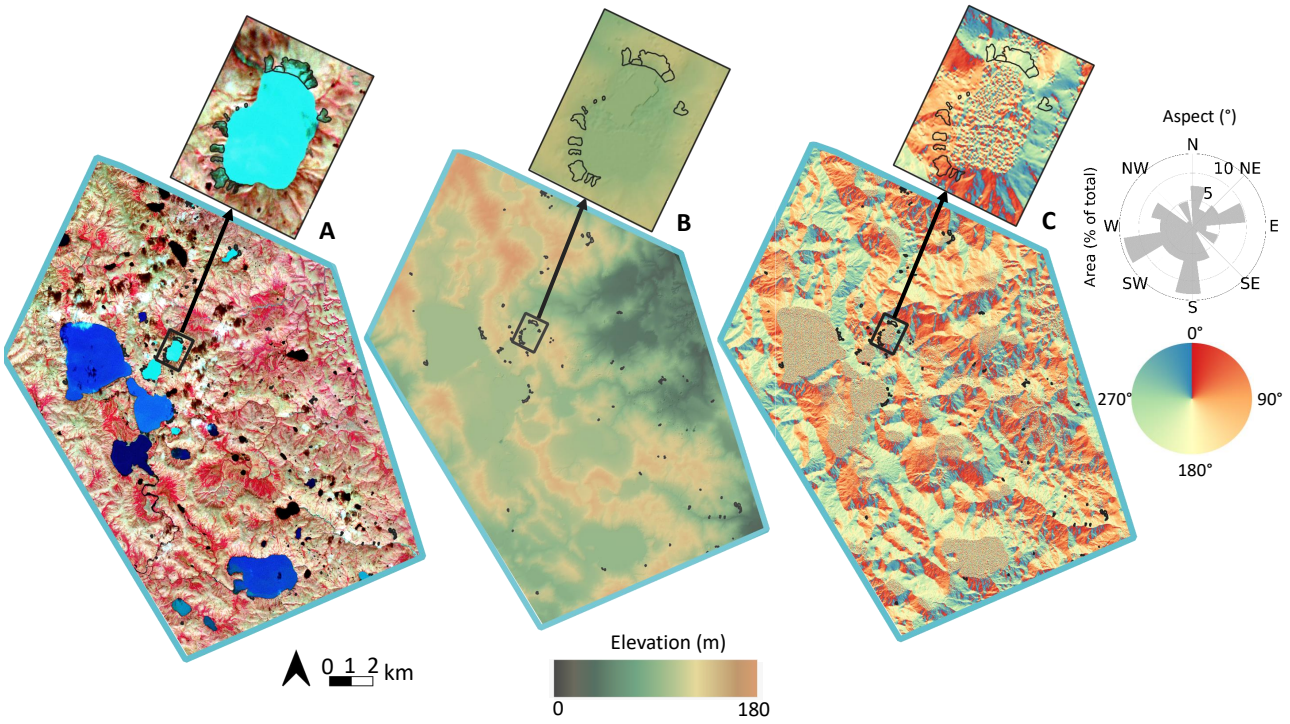

Figure 5.5: Study site West Taymyr with RTS object outlines of 2020. A: PlanetScope satellite image (NIR-R-G) acquired on 21.08.2020, B: ArcticDEM (Porter et al., 2018) superimposed with hillshade, C: slope map derived from ArcticDEM with RTS slope aspect plot weighted by RTS area.

5.2 Non-coastal RTS

As seen in Figure 5.6, the summed RTS area increased significantly throughout the time series at all non-coastal sites. Between the earliest and most recent year of the time series, the summed RTS area at East Taymyr increased by a factor of 33 (3300 %), at West Taymyr by a factor of 2 (100 %) and at Novaya Zemlya by a factor of 4 (400 %).
The areal increase varies in space and time. Exceptionally large increases appear to occur in the short-term, in most cases within a year or two. At East Taymyr the areal gain of RTSs in a single and the most recent year (between summer 2019 and 2020), exceeds the summed increase recorded in the previous three years. At the same site another strong increase occurred between 2011 and 2016. However, the 2011 image is covered largely by clouds which likely reduces the mapped RTS area and number of the year 2011. In the four years following 2011, no imagery exists which further diminishes the significance of increase. At Novaya Zemlya, an outstanding increase in RTS areal extent occurred in the period between 2013 and 2018 with a summed areal increase of nearly 400 %.
In contrast to the summed RTS area, the RTS number does not show a clear trend that applies to all non-coastal sites. At East Taymyr, the RTS number follows a similar trend as the summed RTS area, both increase significantly throughout the time series. At West Taymyr and Novaya Zemlya, RTS numbers did not significantly increase. At West Taymyr, RTS numbers slightly fluctuated but stayed more or less steady at around 100. At Novaya Zemlya, RTS numbers even decreased in more recent years (after 2016).

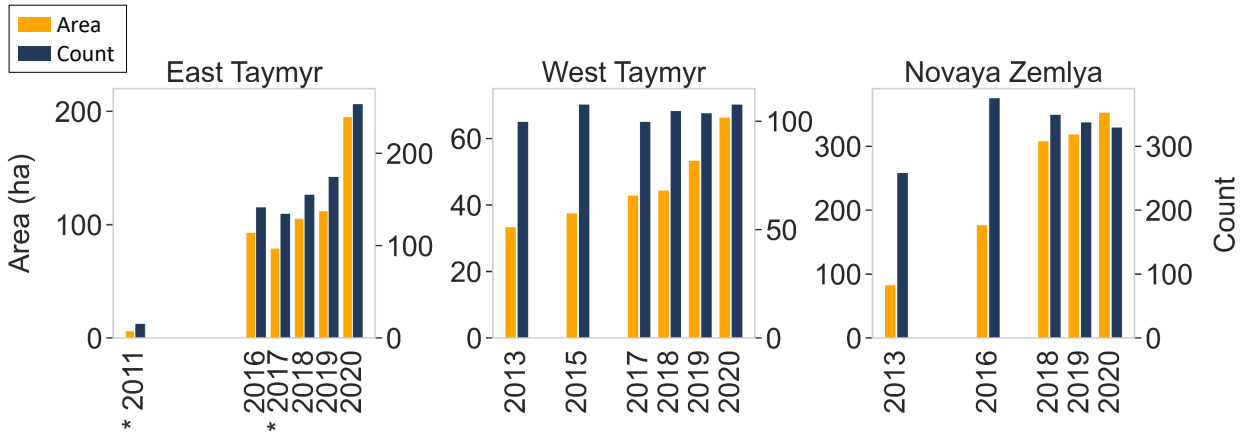

Figure 5.6: RTS number and summed RTS area per year at South Kolguev, North Kolguev and Bol'shoy Lyakhovsky. Orange bars represent summed RTS area in ha and blue bars represent RTS number.

RTSs are not distributed uniformly throughout the Russian High Arctic, the RTS-affected area varies significantly in space. At Novaya Zemlya around 6.4 % of the study area has been affected by active slumps in 2020. At the northern peninsula of Sukhoy Nos, a local subregion, even about 30 % of the area was affected by RTSs in 2020 (Fig.5.7). Novaya Zemlya reached by far the largest extend of RTS-affected area in comparison to the total area of the study site. At all other sites the RTS-affected area ranged between 0.1 and 2.1 % of the respective study area (Table 5.1).

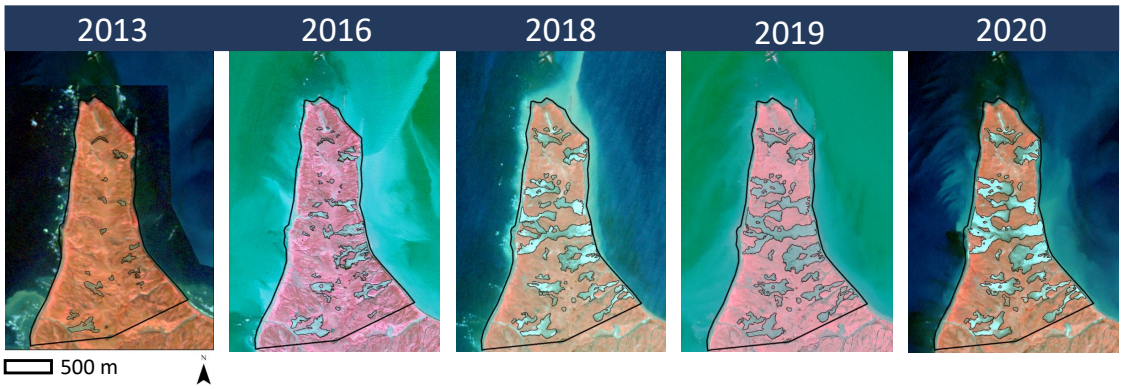

Figure 5.7: Northern peninsula of Sukhoy Nos, subregion of Novaya Zemlya characterized by particularly strong RTS development. Maps show multi-spectral false-color images of the years 2013, 2016, 2018, 2019 and 2020 with corresponding RTS object outline. Left to right: RapidEye image taken on 13.09.2013, Pléíades image taken on 07.09.2016 and PlanetScope images taken on 21.08.2018, 26.07.2019 and 22.07.2020.

5.3 Coastal RTS

In contrast to the non-coastal sites, the summed RTS area at the coastal sites did not show a clear positive trend in time (Fig. 5.8). At all coastal sites, the summed RTS area has changed little over time while a clear negative trend in RTS numbers has been observed in more recent years (following 2017). At North Kolguev, the RTS-affected area slightly rose throughout the investigation period indicating that thermal denudation rates were on average higher than thermal abrasion rates. At South Kolguev, the summed RTS area stayed more or less the same, indicating that thermal abrasion and thermal denudation rates advanced at a similar rate. RTSs at Bol'shoy Lyakhovsky form an exception as active slumps were often formed as part of older, stabilized slumps. In the investigated time period the headwalls of the slumps retreated steadily, while the lower parts of the slumps stabilized over time which overall resulted in a decrease of the summed RTS area. It should be taken into account however, that the total area affected by RTSs increased. By the method I chose in this study, I focused only on active RTSs and therefore did not include the entire area affected by RTSs in my calculations, which would include inactive RTS portions.

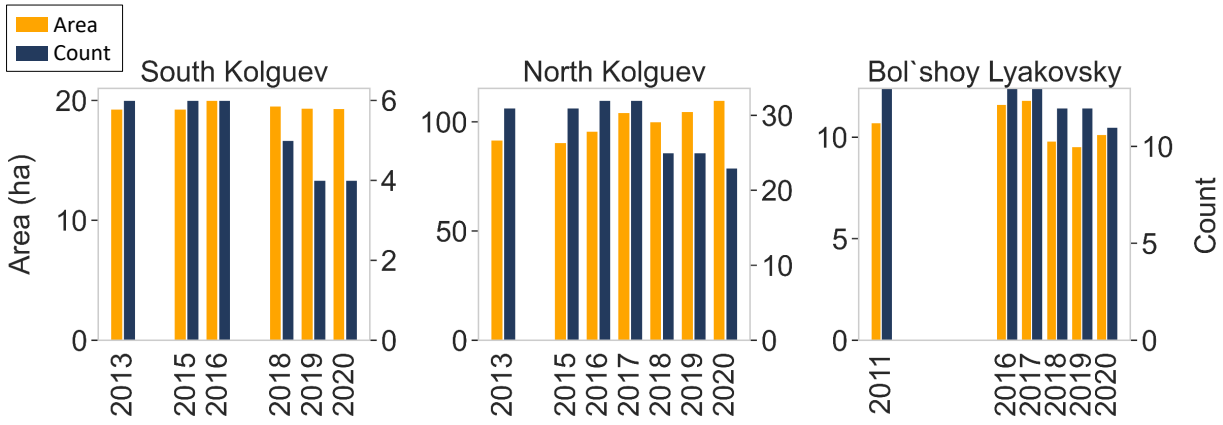

Figure 5.8: RTS number and summed RTS area per year at South Kolguev, North Kolguev and Bol'shoy Lyakhovsky. Orange bars represent summed RTS area in ha and blue bars represent RTS number.

5.3.0.1 Headwall and bluff erosion rates

For the coastal sites, RTS headwall and bluff base change rates were calculated for the investigation period. The change distances and rates were summed and averaged per study site respectively. Headwall erosion results from thermal denudation and bluff base erosion from thermal abrasion.

At Kolguev, I retrieved headwall and bluff base change rates between 2013 and 2020 along two sections of the West Coast. The slumps located further north revealed average thermal abrasion rates at the base of -1.4 m/yr and average thermal denudation rates at the headwall of -3.9 m/yr (see B in Fig.5.9 and B in Fig.5.10). The bluff base retreated on average -10.1 m, with maximum net distances up to -34.2 m. The headwall retreated on average -27.8 m, in some places even up to -136.6 m. I discovered, that the RTSs located further south showed average thermal abrasion rates at the bluff base of -5.2 m/yr and average thermal denudation rates at the headwall of -2.9 m/yr (see A in Fig.5.9 and A in Fig.5.10). In the seven years investigated, the headwall retreated on average -20.3 m and up to -68.0 m maximum, while the bluff base retreated on average -36.4 m, with maximum net distances up to -49.1 m.

These bluff base and headwall change rates reveal that RTSs have been active at the West Coast of Kolguev in recent years. In some areas, the headwall has eroded faster than in others, as has the bluff base. Comparatively stronger erosion along bluffs and headwalls was observed for RTSs of larger individual size. At South Kolguev, headwall retreat rates are high in distinct areas, where bluff base retreat rates are high as well. This phenomenon does not show up for the headwall and bluff change rates of North Kolguev. In a southern section of North Kolguev, even the opposite is the case, very high headwall erosion rates occur along large slumps were bluff base erosion rates are among the lowest (see black and white arrows in Fig.6.2).

At Bol'shoy Lyakhovsky, headwall and bluff retreat rates were calculated between 2011 and 2020. Headwall change rates reached on average around -6.3 m/yr. In the nine years investigated, the headwall retreated on average -50.5 m, in some places even up to -93.8 m (see C in Fig.5.9 and C in Fig.5.10). The change rate of the bluff base, calculated for the same period, was on average -3.7 m/yr. The bluff base eroded on average -33.5 m, in some places even up to -81.9 m.

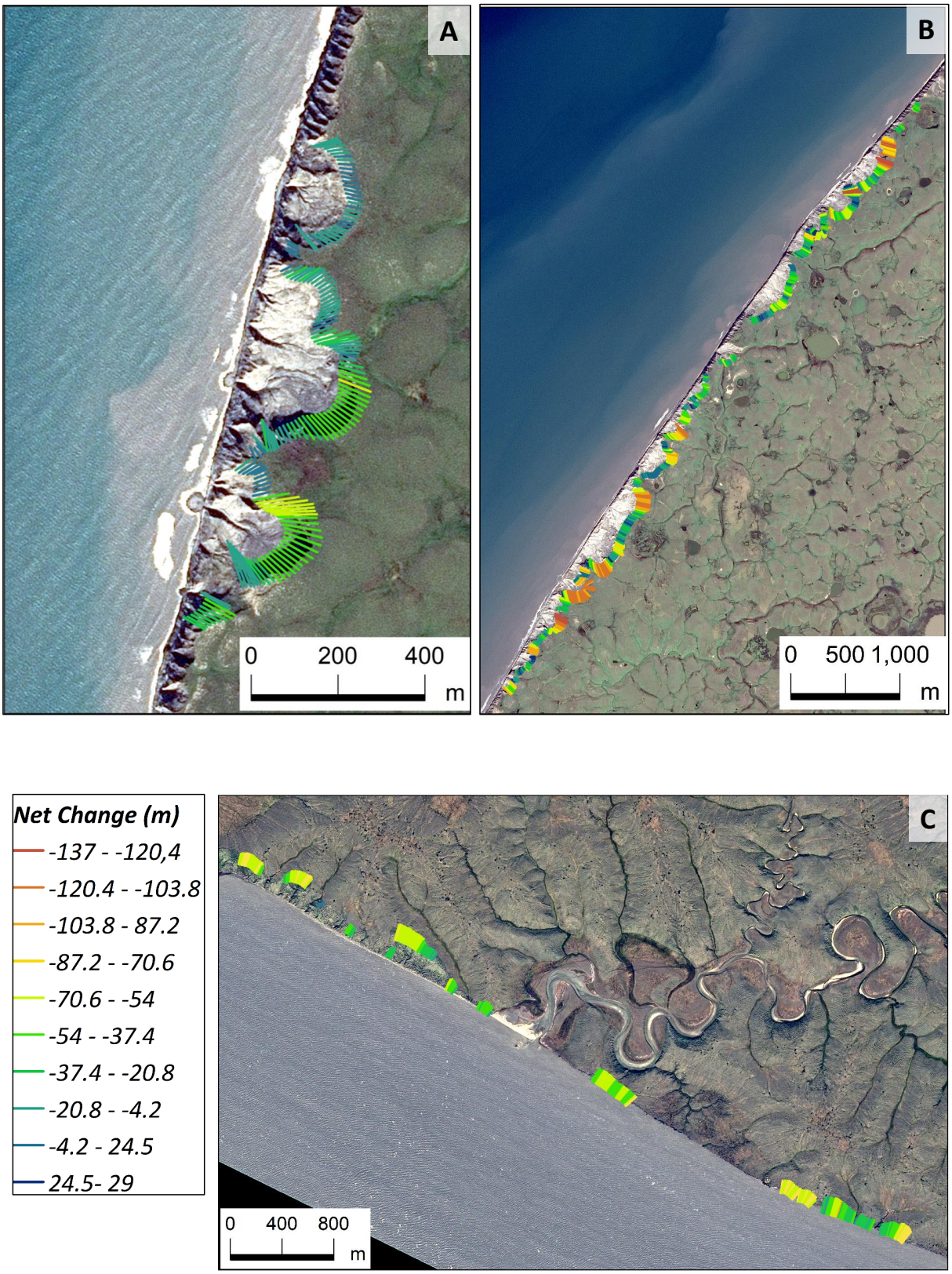

Figure 5.9: Net headwall change rates at South Kolguev (A), North Kolguev (B) and Bol'shoy Lyakhovsky (C); Rates were calculated between 2013 and 2020 at North and South Kolguev and between 2011 and 2020 at Bol'shoy Lyakhovsky. Background images are visualized in RGB color scheme; North Kolguev: SPOT 6 image taken on 01.07.2016, South Kolguev; SPOT 6 image taken on 20.08.2016, Bol'shoy Lyakhovsky: SPOT 7 image taken on 03.08.2016.

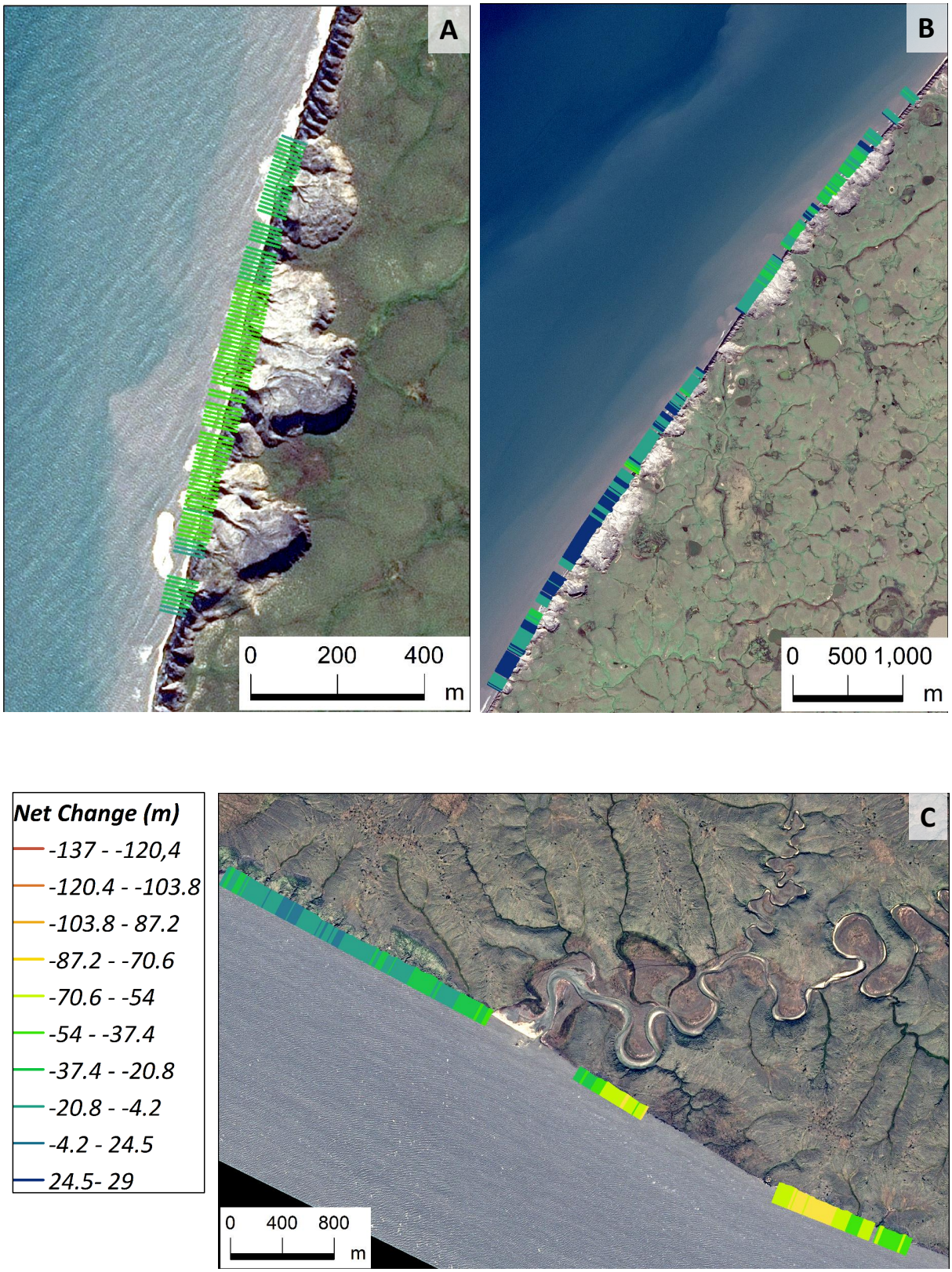

Figure 5.10: Net bluff change rates at South Kolguev (A), North Kolguev (B) and Bol'shoy Lyakhovsky (C); Rates were calculated between 2013 and 2020 at North and South Kolguev and between 2011 and 2020 at Bol'shoy Lyakhovsky. Background images are visualized in RGB color scheme; North Kolguev: SPOT 6 image taken on 01.07.2016, South Kolguev; SPOT 6 image taken on 20.08.2016, Bol'shoy Lyakhovsky: SPOT 7 image taken on 03.08.2016.

6 Discussion

6.1 RTS and study site characteristics

The study sites are located in ice-rich permafrost of different origin, characterized by buried glacial ice deposits or syngenetically formed Yedoma permafrost. Novaya Zemlya and Kolguev had been covered by a dynamic ice sheet during the LGM. Ground ice in this region consists of buried glacial ice, preserved by the aggregation of permafrost after the retreat of the ice sheets. The investigated RTSs at Bol'shoy Lyakhovsky have evolved in Yedoma deposits, were thick, syngenetic ground ice formed as sediment was deposited during the late Pleistocene. East and West Taymyr are located in an intermediate zone. The origin of permafrost involved at both study sites cannot be clearly determined from the literature. After Barr & Clark (2012) the broader region is shaped by buried glacial moraine complexes, however, after (Strauss et al., 2022) the study sites are located within the Yedoma domain, which includes the Yedoma deposits itself and frozen deposits that accumulated after Yedoma degradation in thermokarst landforms. Since the permafrost ice content is an important factor determining RTS development, the different formations of permafrost and ground ice in these regions likely affect RTS dynamics and characteristics.

Most of the observed slumps are located on slopes with a gradient between 2 and 7 °. Bernhard et al. (2022a) and Runge et al. (2022) found that RTSs occurred in the same slope range at other locations in northern Russia. An overall preferred slope orientation of RTSs was not identified in this study. At West Taymyr, the summed RTS area is largely limited to southwest facing slopes, which is consistent with previous studies assessing RTSs in northern Russia (Bernhard et al., 2022a; Nesterova et al., 2020). Overall higher initiation and growth rates of RTSs are associated with a slope orientation to the southwest due to the higher available energy of solar radiation (Lewkowicz, 1987), which could be the reason why RTSs at West Taymyr often occur at this slope orientation.

On Novaya Zemlya, RTSs were predominantly facing towards west and northwest. This is one of the dominant coastal slope orientations in the study region. It is likely that the proximity to the ocean is an enhancing growth factor for RTSs in this region, as a large portion of the summed RTS area occurs close to the coast, facing the ocean. At

East Taymyr, no preferential slope aspect of RTSs is apparent, slumps occur largely surrounding the two prominent lakes in the study region. It is apparent however, that RTSs close to the further north located lakeshore occur on southwest facing slopes and that RTSs on the further south located lakeshore face towards the north- and southeast, which is roughly the opposite direction. Because RTSs are a degradation feature of ice-rich permafrost, it is likely that small-scale variations in the ground ice content affect the local distribution and extent of RTS (Bernhard et al., 2022a; Ramage et al., 2017).
All coastal slumps are facing towards the ocean. At Kolguev, slumps occurred on west and northwest oriented slopes of the West Coast. At Bol'shoy Lyakhovsky, slumps occurred on the southwest oriented slopes of the southern coast of the island. The high ice content observed at both coastal stretches, as well as the proximity to the ocean are likely reinforcing factors for RTS activity along these sites.
The mean sizes of RTSs at the five sites range between 0.3 (at Novaya Zemlya in 2013) and 4.8 ha (at North Kolguev in 2020) which agrees well with the findings of previous studies recording mean RTS sizes of 1.5 (Ramage et al., 2017) and up to 4.8 ha (Runge et al., 2022). The mean slump sizes were overall larger at the coastal sites in comparison to the non-coastal sites where RTSs occurred mainly on hill slopes and lake shores. Observed coastal RTSs, however, were much smaller in number. At several study sites the maximum slump size fell into the defined size range of megaslumps (5-40 ha) (Kokelj et al., 2015). At South Kolguev, maximum slump sizes reached 9 ha, at East Taymyr 14.6 ha, at Novaya Zemlya 19.7 ha (largest non-coastal slump observed) and at North Kolguev 27.8 ha (largest coastal slump observed). These RTSs undercut maximum extents of megaslumps recorded in northwest Canada by Kokelj et al. (2015), were a slump reached 39 ha in size and exceeded maximum extents of RTSs found in North Siberia by Runge et al. (2022) were a slump reached up to 14.9 ha in size. It should be considered however, that Runge et al. (2022) defined a maximum mapping unit which filtered out potential RTSs larger than 15 ha. These results reveal, that due to the wide spatial coverage of diverse study sites, the manual mapping method and the usage of VHR satellite imagery, I was able to capture both, smaller slumps less than half a hectar in size as well as megaslumps of up to nearly 28 ha in size.

6.1.1 Dynamics of non-coastal RTS

The summed RTS area increased significantly throughout the time series at all non-coastal sites. This coincides with recent studies by Ward Jones et al. (2019), Lewkowicz & Way (2019), Runge et al. (2022) which found that RTS activity increased in recent years and concluded that this clear positive trend in slump growth observed in many parts of the High Arctic likely relates to climate warming. The magnitude in RTS growth varied among the non-coastal study sites. At East Taymyr, RTSs increased exceptionally strong in areal extent and number. In 2011, 16 slumps affected an area of about 6 ha. In 2020, 254 slumps affected an area of roughly 196 ha. This is equal to an areal increase by a factor of 33 in nine years. These findings indicate that RTSs newly developed or re-initiated leading to a total areal increase. This means, that the increase in summed RTS area was mainly caused by the initiation of new slumps. These results are smaller but similar in magnitude to the volumetric rate of change observed between 2010 and 2021 at a study site on northern Taymyr (Bernhard et al., 2022b). Bernhard et al. (2022b) discovered a 43-fold increase in volume and found that this increase was induced by the increase in RTS initiations, which agrees well with my findings. Additionally, they found evidence that a particularly large volumetric increase in 2020 resulted of the northern Siberian heat wave of 2020.

At West Taymyr and Novaya Zemlya, the increase in total RTS area is less pronounced when compared to East Taymyr. The summed RTS area doubled at West Taymyr thoughout the investigated period, with a more gradual increase at the beginning of the time series. In 2013, 100 RTSs affected 33 ha and in 2020, 108 RTSs affected 67 ha. The comparatively small increase in RTS number reveals, that here, the areal increase is likely caused by the growth of already existing slumps rather than the initiation of new ones, as also pointed out by Lewkowicz & Way (2019) for the Canadian High Arctic and Runge et al. (2022) for the Russian High Arctic. Despite these characteristic differences in RTS development at West and East Taymyr, both sites showed a strong increase in total RTS-affected area in 2020, which could potentially be related to the heat wave which occurred in northern Siberia in 2020.

At Novaya Zemlya, the summed RTS area of 84 ha (259 slumps) in 2013 increase by a factor of 4 to 353 ha (330 slumps) in 2020. Between 2013 and 2016, RTSs increased

significantly in number, likely inducing the increase in the summed RTS area. After 2016, RTSs decreased in number, however, the RTS affected area strongly increased, even more steeply than before. The numerical decline after 2016 can be explained by the merging of neighbouring slumps (Fig.6.1), indicating that after 2016 the increase in summed RTS area was clearly induced by growth instead of initiation of new slumps, similar to West Taymyr.

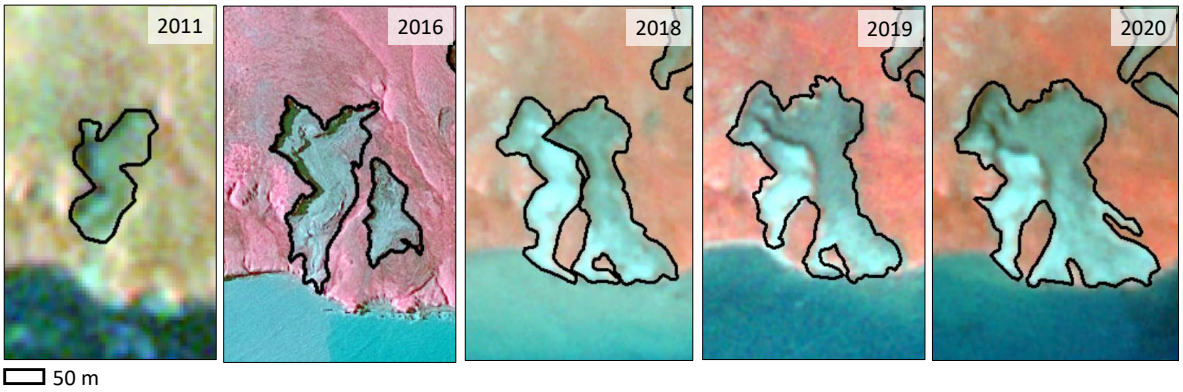

Figure 6.1: False-color image sections of several years overlaid with RTS outlines, visualizing the merging of RTSs at the coast of Novaya Zemlya between 2013 and 2020. Background images left to right: RapidEye image taken on 13.09.2013, Pléíades image taken on 07.09.2016 and PlanetScope images taken on 21.08.2018, 26.07.2019 and 22.07.2020.

6.1.2 Dynamics of coastal RTS

At the coastal study sites, changes in the summed RTS area were less pronounced. At North Kolguev, the total area affected by RTSs slightly increased by around 18 ha - or 20 % - between 2013 and 2020. The areal increase at North Kolguev can likely be explained by uneven thermal abrasion and denudation rates. While the headwall erosion occurred at an overall higher rate, the bluff base retreated at a lower rate which resulted in an increase in the summed RTS area. Interestingly, in some places, where the headwall erosion was highest (e.g. at the largest slump observed, see slump 'LS' in Fig.6.2), the bluff base erosion was the lowest and even reached positive values, which indicates that material had accumulated at the base of the slumps (see black arrows in Fig.6.2, A). Thermal abrasion and thermal denudation rates are not necessarily in equilibrium because they are caused by different factors. Thermal denudation is strongly dependent on solar

radiation while thermal abrasion is also dependent on ocean currents, wind direction, wind strength and other factors affecting the mechanical and thermal parameters of the sea (Gavrilov & Pizhankova, 2018). All these factors can vary greatly in space and time. If the erosion of the headwall is rapidly proceeding, the eroded material may not get transported away directly by the sea and is deposited at the base. This can result in low negative or even positive change values and in the overall reduction of the calculated bluff change rate, also leading to an increase in the calculated RTS area extent.

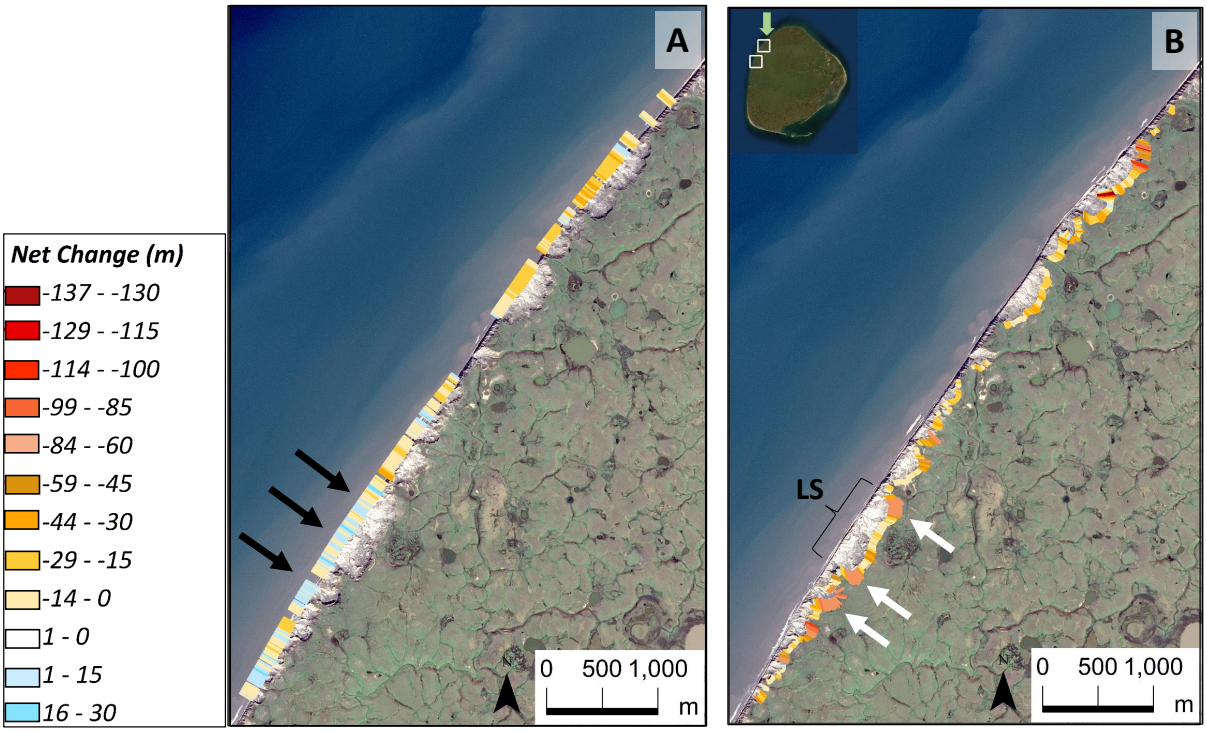

Figure 6.2: RTS on North Kolguev with net headwall and bluff change rates between 2013 and 2020: map A visualizing bluff base net change rates in m; map B visualizing headwall net change rates in m. Note that change rates range between high erosion (red) and accumulation (blue). 'LS' marks location of largest slump observed. Black arrows mark very low change rates, white arrows mark very high change rates. The background image is the SPOT 6 taken on 01.07.2016, visualized in RGB color scheme.

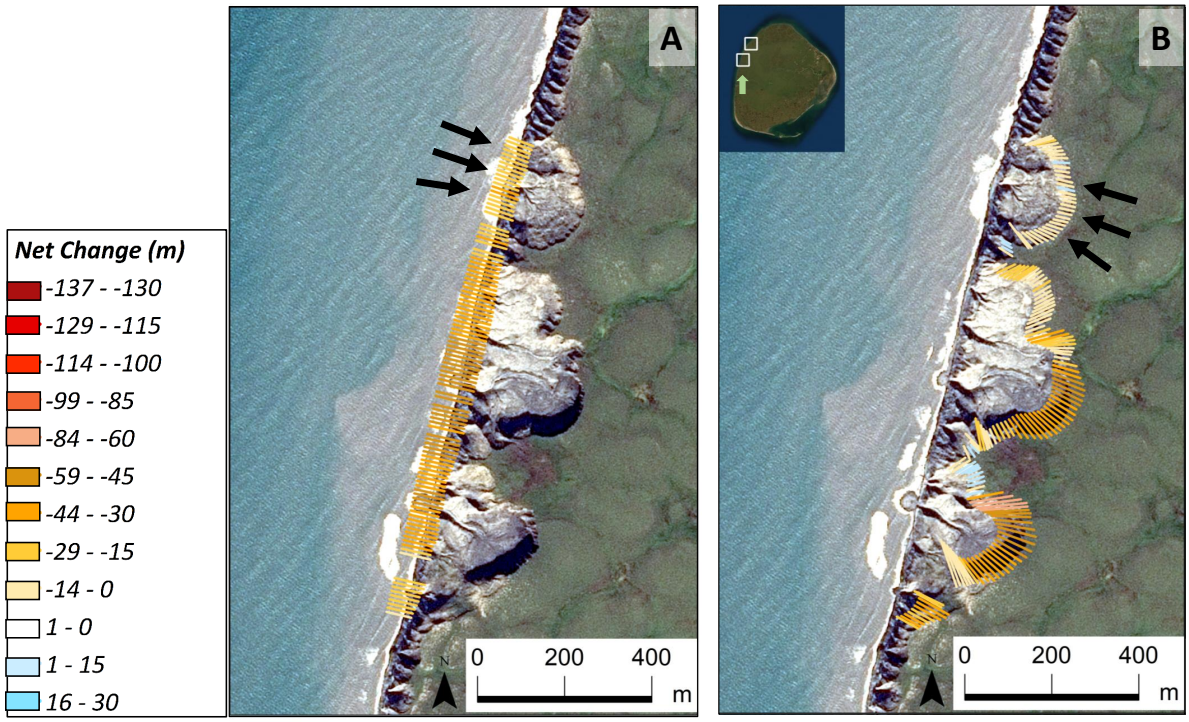

Figure 6.3: RTS on South Kolguev with net headwall and bluff change rates between 2013 and 2020: map A visualizing bluff base net change rates in m; map B visualizing headwall net change rates in m. Note that change rates range between high erosion (red) and accumulation (blue). 'LS' marks location of largest slump observed. Black arrows mark very low change rates, white arrows mark very high change rates. The background image is the SPOT 6 taken on 20.08.2016, visualized in RGB color scheme.

At South Kolguev, the summed RTS area remained more or less the same throughout the investigation period. However, the calculated headwall and bluff base rates were not in equilibrium. When comparing average thermal abrasion and thermal denudation rates, the bluff base erosion advanced on average more rapidly (-5.2 m/yr) than the headwall erosion (-2.9 m/yr). It should be noted however, that the headwall did not erode equally fast along the entire stretch. The most severe headwall erosion rates occurred along the large, central and south located slumps, while the headwall of the smaller slump in the North nearly stabilized over time (see black arrow in Fig.6.3, B). The bluff retreated overall uniformly along the entire coastal stretch. Transects have been calculated for every 10 m, respectively along bluff base and headwall. The headwall is longer than the bluff in its entire length due to its bulging shape. The bluff is a relatively straight boundary and therefore shorter. As a result, 158 transects have been calculated along the headwall and

only 97 along the bluff. This produces unequally weighted transects. It is likely that this results in an overall lower relative headwall retreat rate which should be taken into account when comparing average thermal abrasion and thermal denudation rates.

Some previous studies by Günther et al. (2019) and Kizyakov et al. (2016) looked at headwall and bluff base erosion rates at the West Coast of Kolguev whereby these examined earlier periods, respectively. Günther et al. (2019) calculated bluff base rates of -1.7 and -2.4 m/yr between 2002 and 2012 along the whole coastal stretch of western Kolguev. These results are slightly higher than bluff base rates of -1.4 m/yr (2013-2020) calculated along North Kolguev. Average bluff base erosion rates calculated along South Kolguev were -5.2 m/yr (2013-2020) and thus largely exceed previous results of Günther et al. (2019).

Kizyakov et al. (2016) calculated average RTS growth rates along the entire West Coast of Kolguev. They observed thermal denudation rates of -2.4 m/yr between 1948-2002 and -2.6 m/yr between 2002-2012. They also calculated maximum growth rates which reached up to -15.1 m/yr (2009-2012). In this study, I calculated average headwall change rates between -2.9 m/yr at South Kolguev and -3.9 m/y at North Kolguev for the time span 2013-2020. The calculated maximum headwall change rates observed in this study reached up to -9.7 m/y at South Kolguev and even up to -21.5 m/y at North Kolguev. Compared to the results of Günther et al. (2019) and Kizyakov et al. (2016), who examined the same slumps in more distant time periods, I found overall higher average and maximum retreat rates, suggesting that both thermal abrasion and thermal denudation have become more severe in recent years.

At Bol'shoy Lyakhovsky, slumps located in the northwest of the study site are likely re-initiated or consistently active parts of older, partly stabilized slumps (Fig.6.4 and A.1 in Fig.6.5). While the headwall is actively retreating, at the highest rates observed in this study, some of the lower parts of the slumps became stable over time. This likely leads to the overall decrease in the summed RTS area in recent years. The slumps in the southeast do not appear to be part of stabilized slumps (A.2 in Fig.6.5). They likely formed more recently, indicated by the position of the headwall which is overall closer to the bluff base.

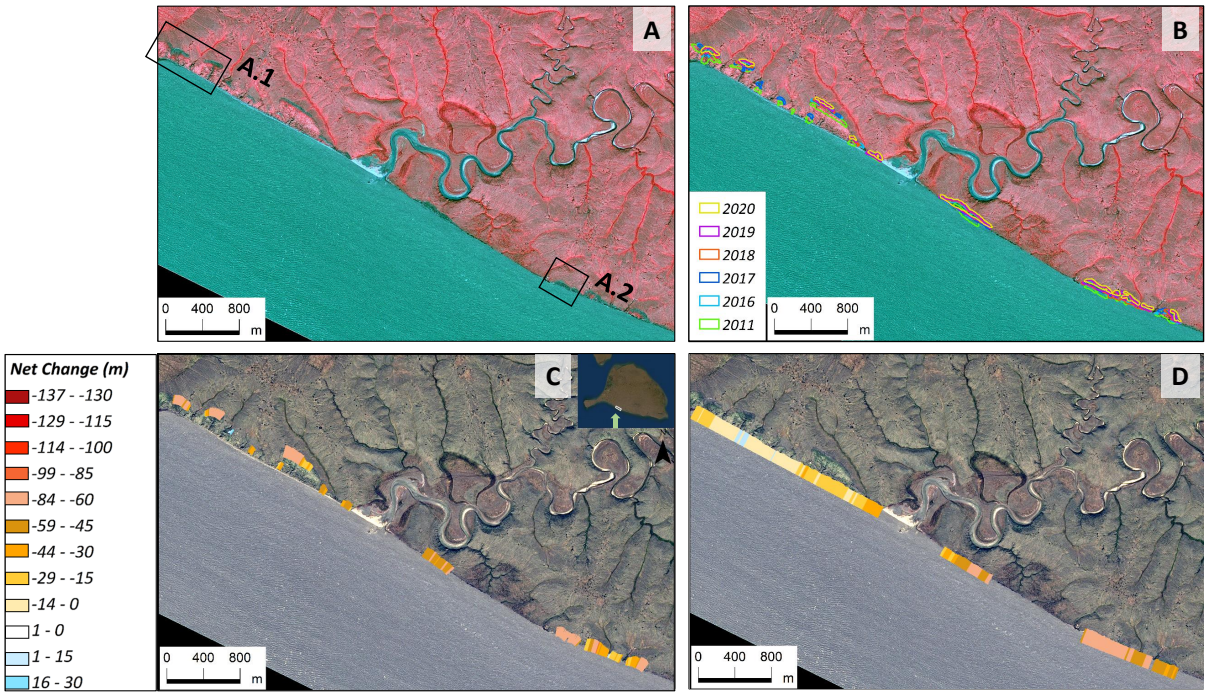

Figure 6.4: RTS on Bol'shoy Lyakhovsky visualized on the Spot image of 2016: on map A and B the image is shown in a false color scheme, on map C and D the image is shown in RGB color scheme; map A marks 'A.1' and 'A.2', locations of characteristic slumps, visualized in Fig.6.5; map B visualizes RTS object outlines between 2011 and 2020; map C shows net headwall change rates in m; map D shows net bluff base change rates in m. Note that the change rates range between high erosion (red) and accumulation (blue). The background image is the SPOT image taken on 03.08.2016.

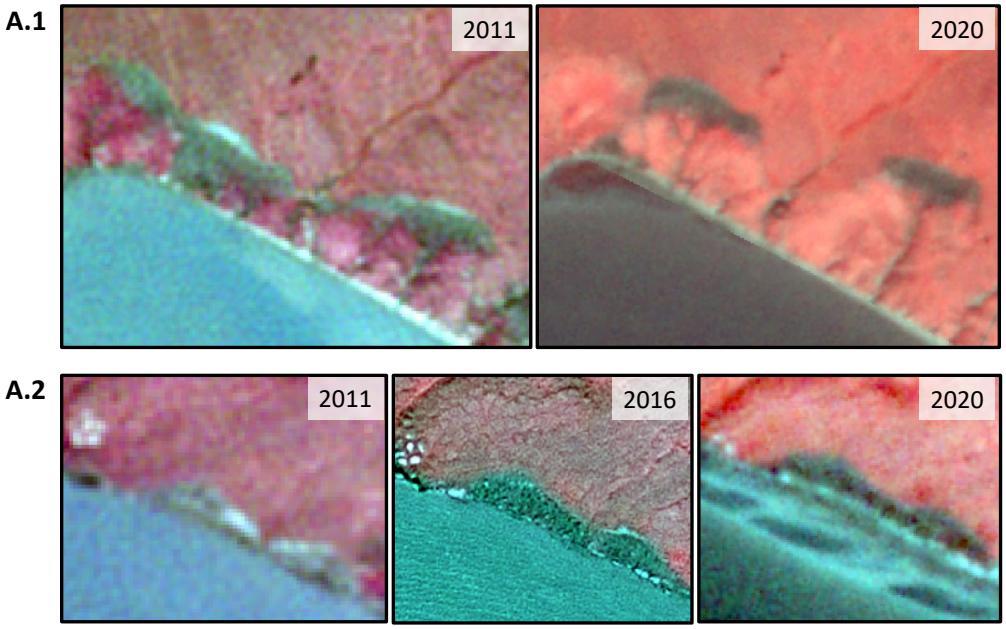

Figure 6.5: False-color image sections of a subregion at the Bol'shoy Lyakhovsky study site, showing characteristic slumps; see Fig.6.4, A for the exact location of the slumps at the study site. A.1: northeast located RTS on the RapidEye image taken on 24.07.2011 and the PlanetScope image taken on 11.07.2020; A.2: southwest located RTS on the same images and additionally on the SPOT image taken on 03.08.2016.

The surveyed RTSs at Bol'shoy Lyakhovsky island are located within an Ice Complex, and an area where severe coastal erosion has been observed for decades (Gavrilov & Pizhankova, 2018). Gavrilov & Pizhankova (2018) calculated average thermal abrasion rates along the South Coast of Bol'shoy Lyakhovsky, between 1951-2001 of -3.4 m/yr and between 2000-2013 of -7.7 m/yr. They concluded that the increase in thermal abrasion rates were likely caused by sea ice loss. Furthermore, they stated that the decline in sea ice extent in recent years is likely the dominant driver of coastal erosion processes in this region, while predominantly enhancing thermal abrasion rates. Thermal abrasion rates at Bol'shoy Lyakhovsky calculated in this study averaged -3.9 m/year, exceeding the rates calculated prior to 2000 but undercutting the average rates calculated between 2000 and 2013. It should be noted however, that thermal abrasion rates varied spatially and revealed overall higher rates in the Southeast of the study site, where presumably younger, active RTSs are located right at the coastline (B in Fig.6.4).

Thermal denudation rates reached on average around -6.3 m/yr between 2011 and 2020. This was surprising, as the decline in area did not suggest this. Visual inspection indicates, that as the headwalls rapidly retreated in the northwestern section of the study site (A.1 in Fig.6.5), part of the eroded material had accumulated and stabilized on the scar zone while another part of the material had been transported through gully systems down the slope to the base of the slumps, which overall resulted in a decrease in the RTS area. Lantuit et al. (2012) identified a similar development of coastal RTSs of the Yukon coast and concluded that these slumps are beginning to stabilize, likely due to several low-thaw seasons. Whether this is also the case for the slumps on Bol'shoy Lyakhovsky cannot be clearly verified from the data collected. However, it can be assumed that even if some of the slumps are currently in a stabilizing phase, there is a high probability that they will become more active again, due to the polycyclic character of these landforms, the special location in very ice-rich, coastal permafrost and the ongoing warming of the arctic region.

6.2 Temperature and precipitation analysis

To improve our understanding of RTS development it is important to investigate trigger mechanism. Many studies revealed that RTS initiation and growth is determined by climatic and terrain factors. Recent climatic changes, in particular, appear to be the driving force in many cases. Exceptional warm summers enhance permafrost thaw and can lead to the exposure of ground ice which can result in RTS initiation. Heavy precipitation events can amplify the transport of thawed material from the slump floor, further exposing and eroding the frozen ground underneath and thus reinforce RTS growth (Ward Jones et al., 2019). At Banks Island, Lewkowicz & Way (2019) looked at the triggers of thousands of RTSs and found that RTS predominantly grew and newly initiated following exceptional warm summers. Kokelj et al. (2015) observed a large incline in slump growth related to heavy summer precipitation events along the Peel Plateau, in northwest Canada and Ward Jones et al. (2019) found that the increase in summer air temperatures at several sites in the Canadian High Arctic was the main driver for RTS initiation and also that sustained RTS activity was dominated by terrain factors such as slope, aspect and slump morphology.

To identify possible trigger of RTS observed in this study, precipitation and temperature analysis has been performed at all sites. On average, summer and winter temperatures

were clearly above the long-term mean during most of the years studied, revealing enhanced warming in recent years at all sites (Fig.A0.1 and Fig.6.13). In addition, individual extreme years with exceptional high winter and summer temperatures and/or heavy precipitation events had been recorded.

(a) East Taymyr

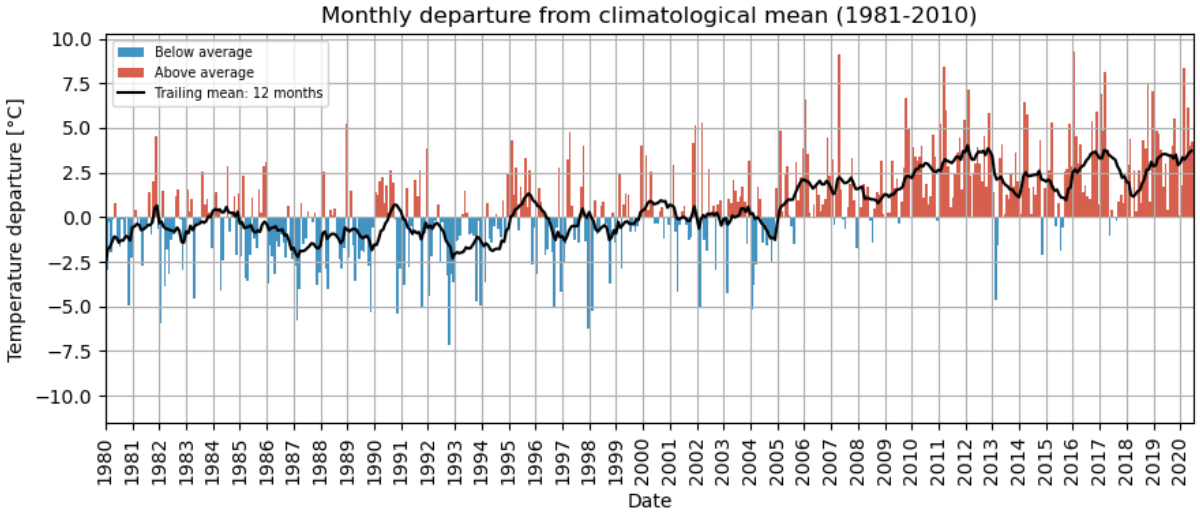

(b) West Taymyr

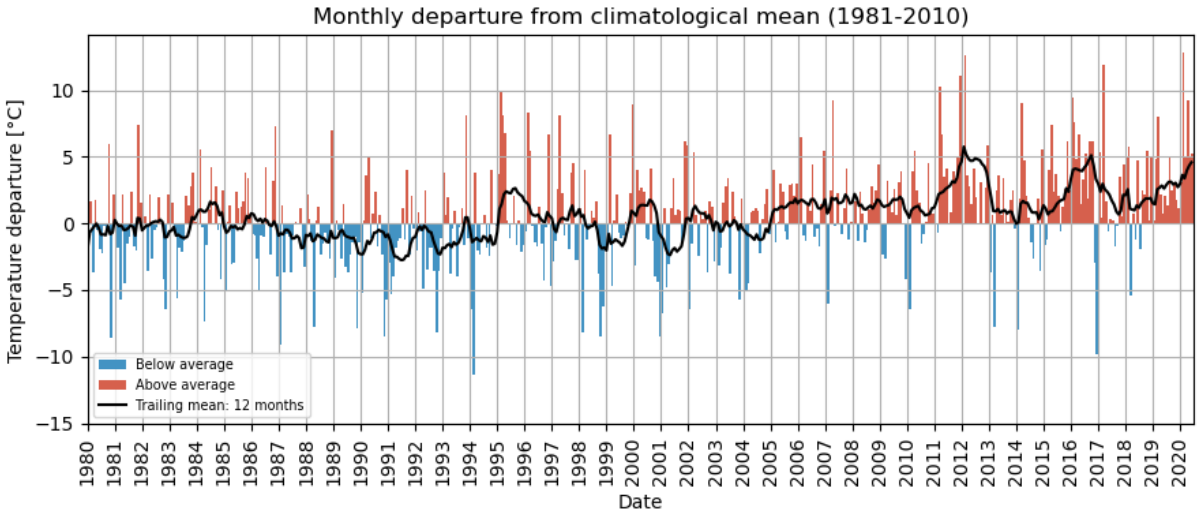

(c) Novaya Zemlya

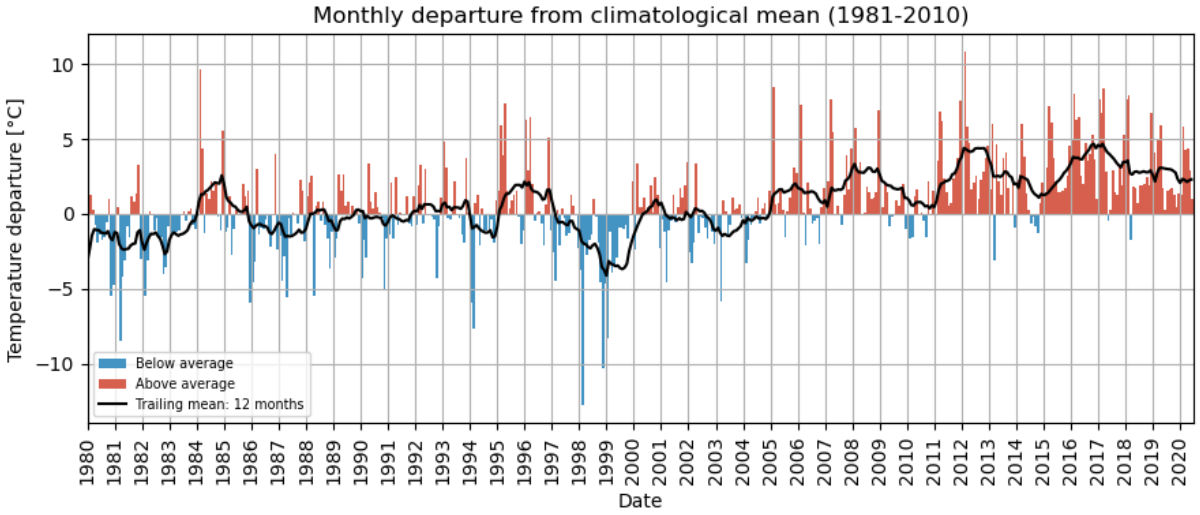

Figure 6.6: Monthly temperature anomaly at the non-coastal study sites (a: West Taymyr, b: East Taymyr, c: Novaya Zemlya) between 1980 and 2020. The black line represents the average monthly temperature over the previous 12 months. Data Source: ERA5 Daily Aggregates (C3S, 2017).

6.2.1 Climate analysis of the non-coastal sites

Within the investigated period, the rise in RTS area did not advance uniformly at the non-coastal study sites. In some years, slump growth advanced more rapidly than in others. The rise in area affected by RTSs steepened predominantly within more recent years. At the two study sites on Taymyr Peninsula, the increase in RTS affected area progessed more rapidly following 2018. At East Taymyr, a more rapid rise occurred between summer 2019 and summer 2020, whereby the total area affected by slumps nearly doubled. At West Taymyr, the more rapid increase in RTS affected area started one year earlier between summer 2018 and 2019 and at Novaya Zemlya a stronger increase showed up already in 2016.

At East Taymyr, 2012, 2018, 2019 and 2020 recorded exceptionally warm summers, with monthly mean temperatures of 7 °C in July 2012 and August 2019 and 8 °C in August 2018 and 2020, respectively (Fig.6.7, A). This is an increase of 4.5 and 5.5 °C compared to the long-term monthly summer average temperature calculated between 1981-2010. The winter temperatures deviated even more significantly from the climatological mean, reaching maximum deviation of roughly 8 °C higher temperatures in Jan 2016. Especially warm winters were observed in 2012 and 2016 (Fig.6.7, B). In addition, large precipitation events occurred in summer 2014. The total amount of precipitation recorded in September reached nearly 120 mm (Fig.6.8). Interestingly, a huge increase in RTS area occurred between 2011 and 2016 (Fig.5.6). At East Taymyr, imagery between 2012 and 2015 is missing, and parts of the study area had been covered by clouds in 2011 which makes it more difficult to quantify RTS development after 2011. Still, the strong increase in both, RTS number and area, observed in 2016 was very likely influenced by the combination of above average summer and winter temperatures and the rain events observed in summer 2014. Another jump in the summed RTS area at East Taymyr occurred between summer 2019 and 2020. This strong increase in RTS initiation and growth was likely induced by the three successive, warm summers of 2018, 2019 and 2020. As previous studies have shown, a delay of one to two years between the onset of reinforcing thaw drivers and the development of RTS is not uncommon Kokelj et al. (2015), Lewkowicz & Way (2019).

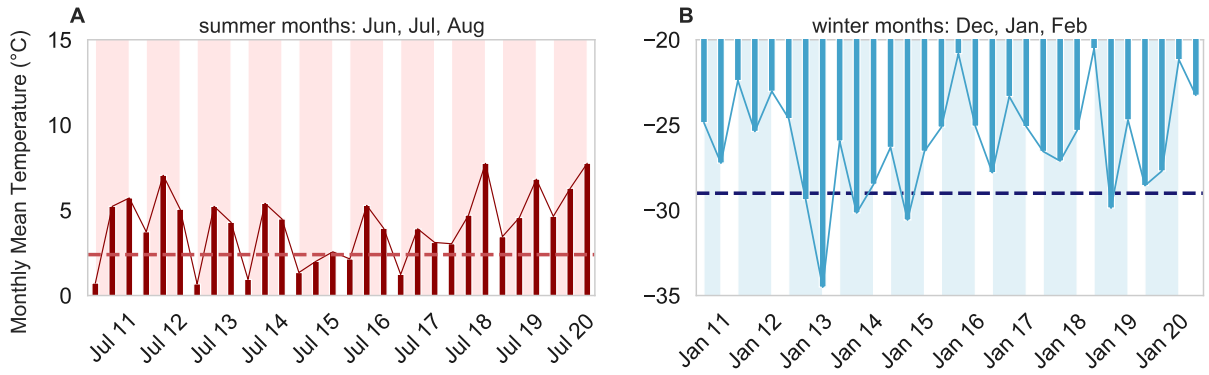

Figure 6.7: Monthly mean temperature data at East Taymyr for the investigation period (2011-2020). A: monthly mean temperature for summer months (Jun, Jul, Aug) in °C, B: monthly mean temperature for winter months (Dec, Jan, Feb) in °C. The climatological mean (1981-2010) for winter and summer temperatures is shown by the dashed line in blue and red, respectively. Data Source: ERA5-Land Monthly Averaged (Muñoz Sabater, J., 2019) and ERA5 Daily Aggregates (C3S, 2017)

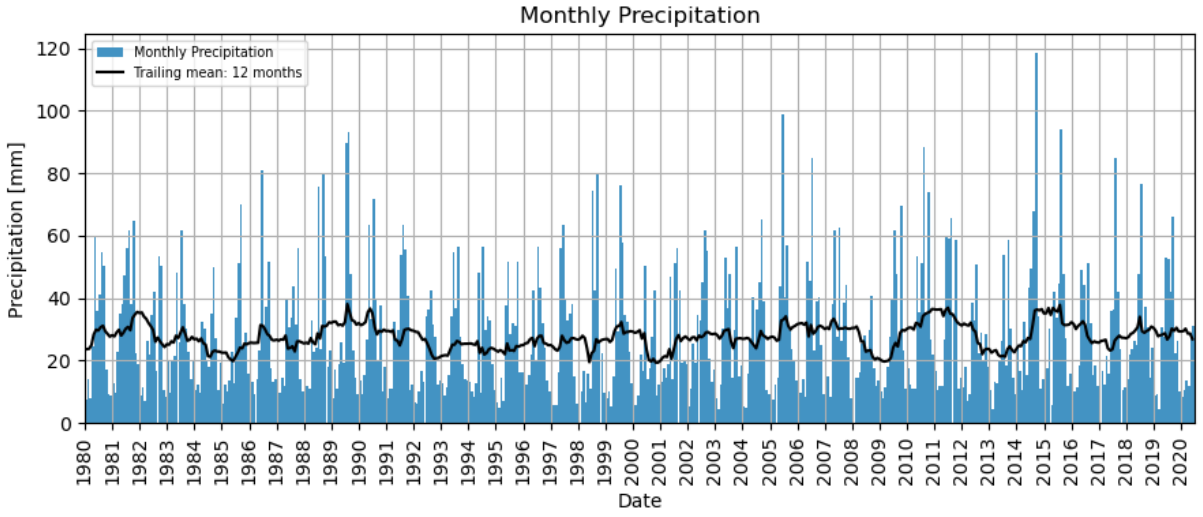

Figure 6.8: Total monthly precipitation data at East Taymyr between 1980-2020. The black line represents the average monthly precipitation over the previous 12 months. Note that precipitation data for 2020 are incomplete. Data Source: ERA5 Daily Aggregates (C3S, 2017)

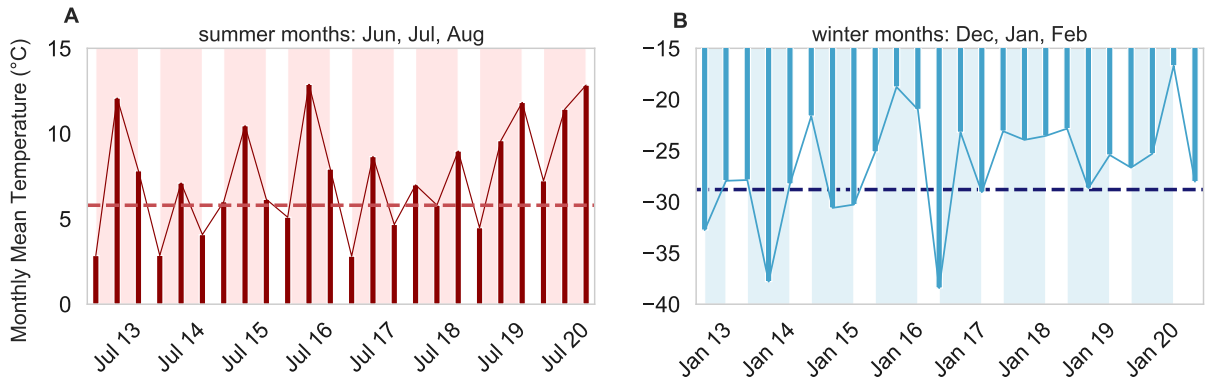

Figure 6.9: Monthly mean temperature data at West Taymyr for the investigated time period (2013-2020). A: monthly mean temperature for summer months (Jun, Jul, Aug) in °C, B: monthly mean temperature for winter months (Dec, Jan, Feb) in °C. Note that in B, the y-axis represents a difference of 25 degrees while in A, a difference of 15 degrees is represented. The climatological mean (1981-2010) for winter and summer temperatures is shown by the dashed line in blue and red, respectively. Data Source: ERA5-Land Monthly Averaged (Muñoz Sabater, J., 2019) and ERA5 Daily Aggregates (C3S, 2017)

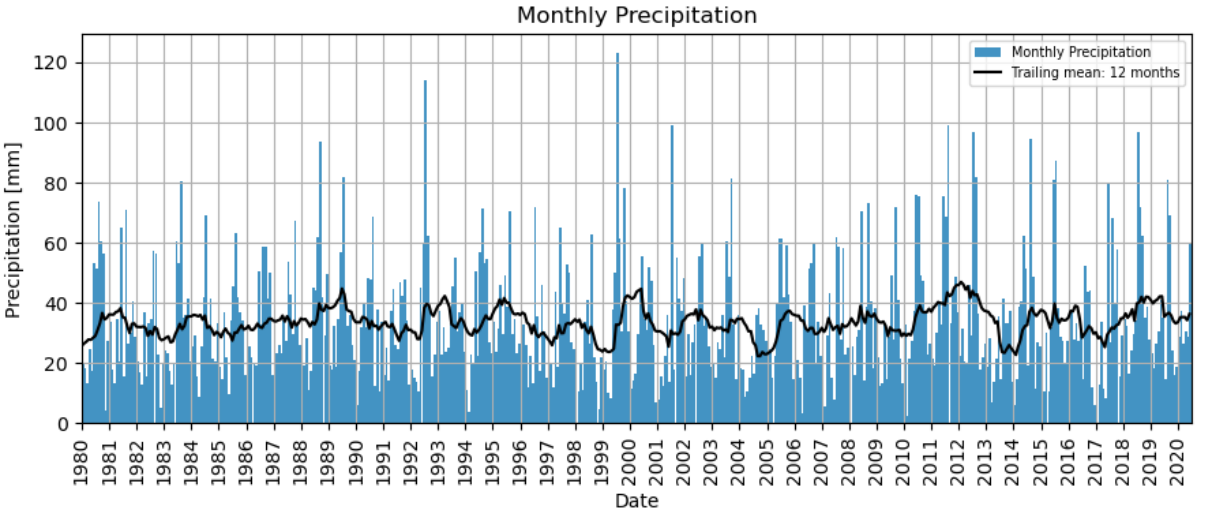

Figure 6.10: Total monthly precipitation data at West Taymyr between 1980-2020. The black line represents the average monthly precipitation over the previous 12 months. Note that precipitation data for 2020 are incomplete. Data Source: ERA5 Daily Aggregates (C3S, 2017)

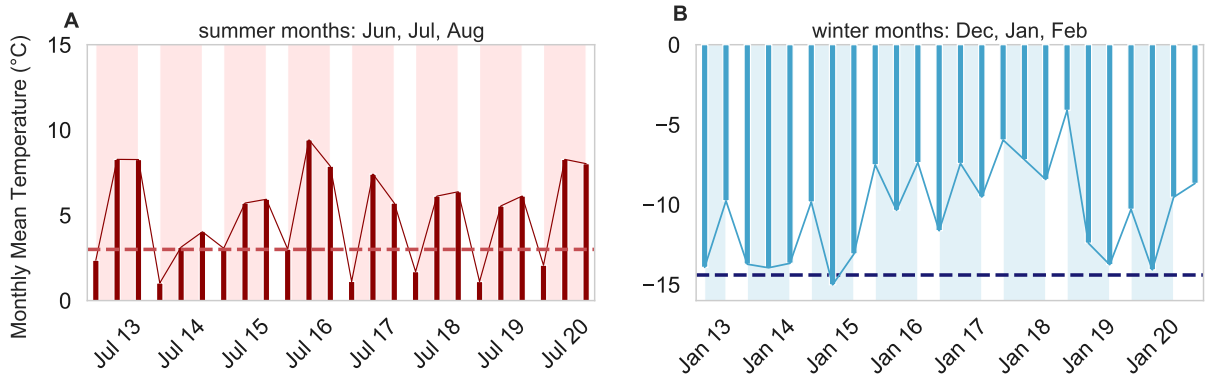

Figure 6.11: Monthly mean temperature data at Novaya Zemlya for the investigated time period (2013-2020). A: monthly mean temperature for summer months (Jun, Jul, Aug) in °C, B: monthly mean temperature for winter months (Dec, Jan, Feb) in °C. The climatological mean (1981-2010) for winter and summer temperatures is shown by the dashed line in blue and red, respectively. Data Source: ERA5-Land Monthly Averaged (Muñoz Sabater, J., 2019) and ERA5 Daily Aggregates (C3S, 2017)

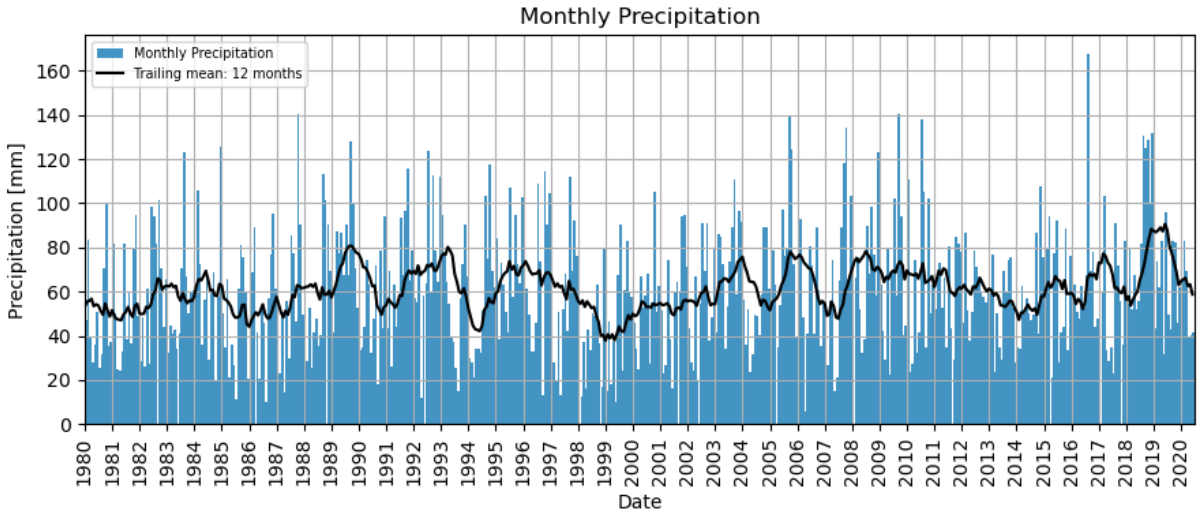

Figure 6.12: Total monthly precipitation data at Novaya Zemlya between 1980-2020. The black line represents the average monthly precipitation over the previous 12 months. Note that precipitation data for 2020 are incomplete. Data Source: ERA5 Daily Aggregates (C3S, 2017)

At West Taymyr exceptional warm summer months had been observed in 2013, 2016, 2019 and 2020 (Fig.6.9, A). During these years, temperature increased by around 6 to 7 °C above the long-term monthly summer temperature average of 5.8°C. Monthly precipitation levels were not particularly high during the study period (Fig.6.10). At West Taymyr jumps in the summed RTS area are less pronounced compared to East Taymyr. Interestingly, there was no sharp increase in totaled RTS area shortly after the warm and dry summer of 2016.

The summed RTS area started to increase more rapidly following 2018. Temperatures had been significantly high in August 2019 and 2020 which likely induced RTS growth. (Bernhard et al., 2022b) observed a large increase in RTS activity at northern Taymyr in summer 2020 in the wake of the Siberian heat wave. It can be assumed that the increase in RTS area in 2020 observed at eastern and western Taymyr can be traced back to this heat wave as well.

At Novaya Zemlya 2013, 2016 and 2020 were the warmest summers of the study period (Fig.6.11, A). In July 2016 monthly mean temperatures reached a record high of nearly 10°C, meaning that average temperatures have been around 7°C above the long-term average. Winter temperatures were overall high between 2016-2018 (Fig.6.11, B). By far the highest winter mean temperatures were recorded in 2017/2018, exceeding the long term-average by nearly 10 °C. In summer 2016, heavy precipitation of more than 160 mm was recorded in August (Fig.6.12). A large accumulation of precipitation was also observed in 2018, however, not associated with a single comparably strong event, but rather a sequence of extremely precipitation rich summer and winter months. The steepest increases in RTS affected area was observed in summer 2016 and 2018. The RTS areal increase in summer 2016 can likely be traced back to the heavy precipitation event and the exceptionally warm average summer temperatures observed in summer 2016. The steep RTS growth in summer 2018 is likely influenced by warm winters of the previous years and the large accumulation of precipitation in 2018.

(a) South Kolguev

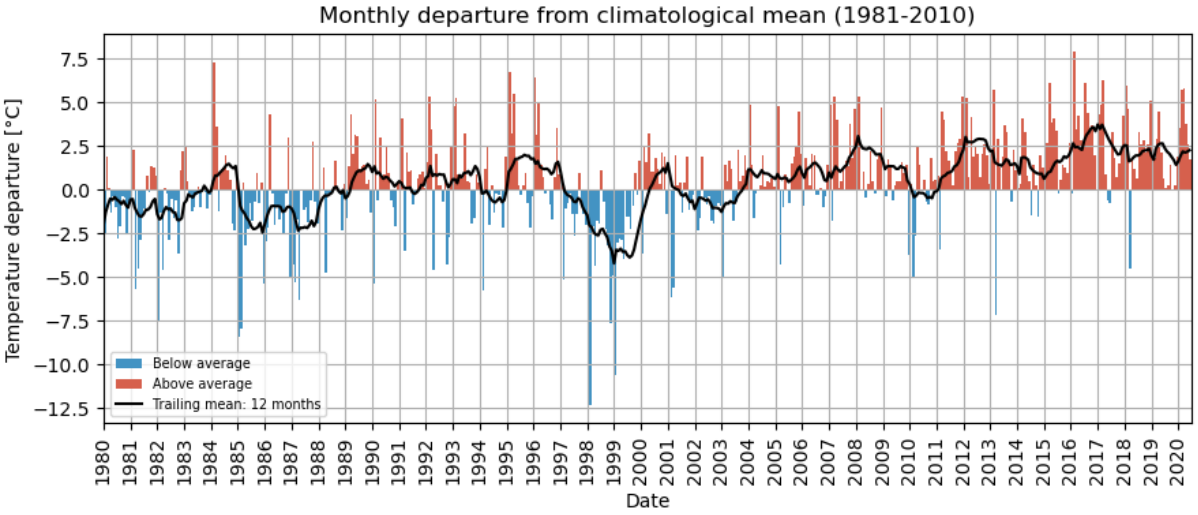

(b) North Kolguev

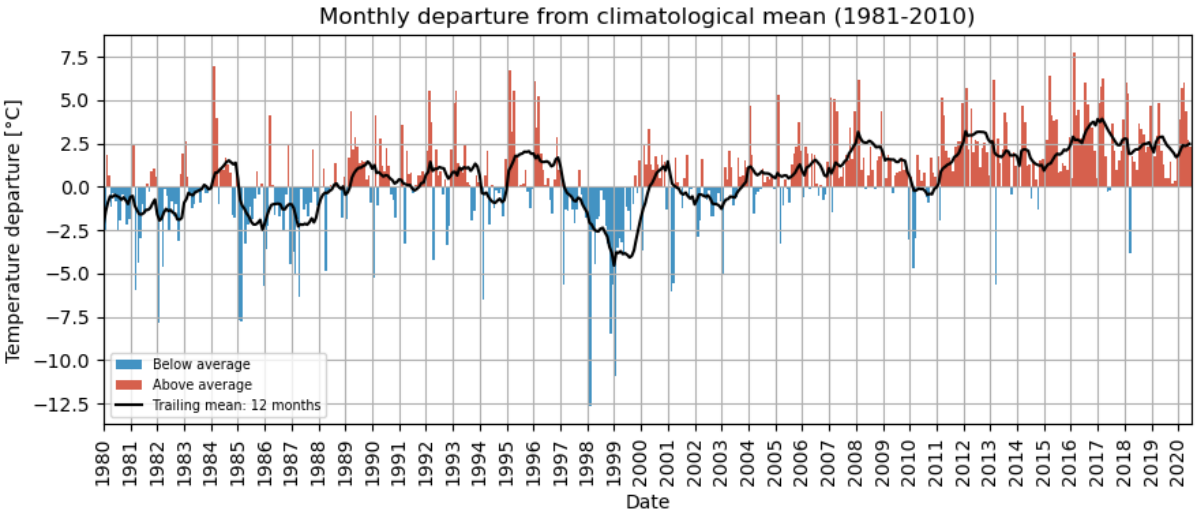

(c) Bol'shoy Lyakhovsky

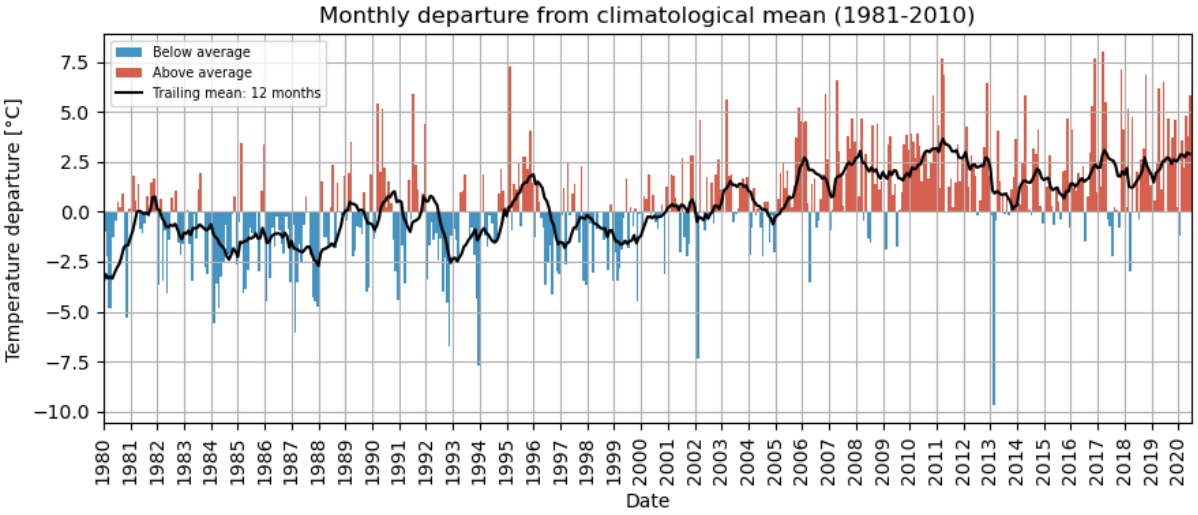

Figure 6.13: Monthly temperature anomaly at the coastal study sites (a: South Kolguev, b: North Kolguev, c: Bol'shoy Lyakhovsky) between 1980 and 2020. The black line represents the average monthly temperature over the previous 12 months. Data Source: ERA5 Daily Aggregates (C3S, 2017).

6.2.2 Climate analysis of the coastal sites

In contrast to the strong positive trend in total RTS area observed at the non-coastal sites, no consistent trend was observed at the coastal sites, and changes in area affected by RTS were less pronounced. This makes it more difficult to relate changes in slump-affected area to climatic factors.

At Kolguev, the summers of 2016 and 2020 were particularly warm (Fig.6.14, A). The July mean temperature reached nearly 15 °C in 2016 and around 13 °C in 2020, roughly 10 and 8 °C above the climatological mean. Winter temperatures were especially high in 2018 were they reached on average -5 °C, a deviation of 5 °C form the long-term average (Fig.6.14, B). Precipitation analysis did not reveal striking rainfall events, however several above average wet years have been observed. In particular, 2018 recorded a large total amount of precipitation (Fig.6.15).

Looking more closely into the summed RTS area at both sites on Kolguev, it appears that a large increase occurred in 2016 at South Kolguev and in 2017 at North Kolguev (Fig.6.16). The 2016 image of South Kolguev has been captured on the 20th of August, at the end of the summer. Therefore, it can be assumed that it can depict temporary changes triggered by the extremely warm summer of 2016. The 2016 image of North Kolguev had been acquired on the 1st of July, at the beginning of summer, before the highest temperatures were reached in July. Thus, it is likely that the 2016 image of North Kolguev has not captured the potential RTS activity likely associated with the outstanding temperature rise in July 2016. Interestingly, however, a strong increase in the RTS area was captured on the image of the following year, suggesting that the heat wave in July 2016 very likely induced enhanced headwall retreat at both sites on Kolguev.

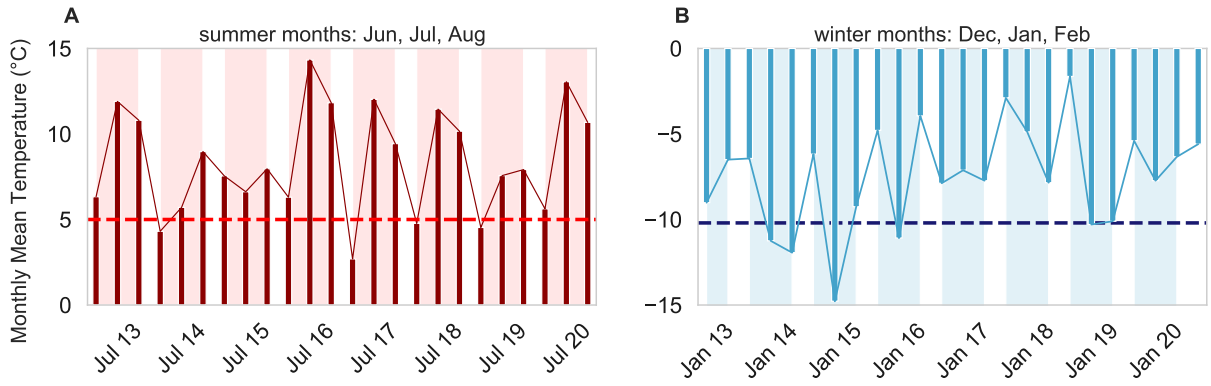

Figure 6.14: Monthly mean temperature data at Kolguev for the investigation period (2013-2020). Note temperature analysis applies to both sites (North and South Kolguev) because of their close proximity to each other. A: monthly mean temperature for summer months (Jun, Jul, Aug) in °C, B: monthly mean temperature for winter months (Dec, Jan, Feb) in °C. The climatological mean (1981-2010) for winter and summer temperatures is shown by the dashed line in blue and red, respectively. Data Source: ERA5-Land Monthly Averaged (Muñoz Sabater, J., 2019) and ERA5 Daily Aggregates (C3S, 2017)

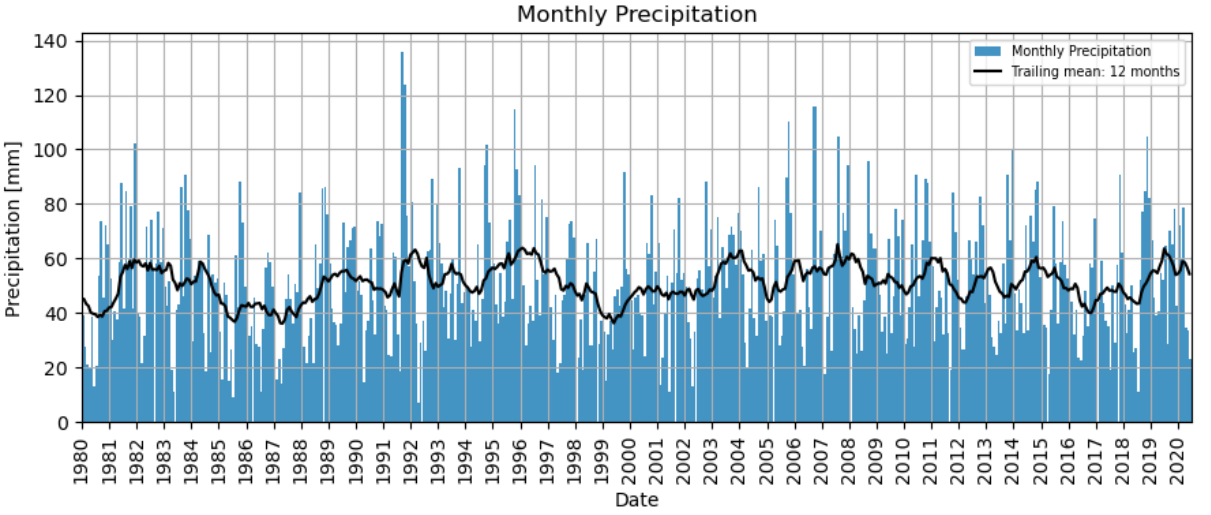

Figure 6.15: Total monthly precipitation data at Kolguev between 1980-2020. Note precipitation analysis applies to both sites (North and South Kolguev) because of their close proximity to each other. The black line represents the average monthly precipitation over the previous 12 months. Note that precipitation data for 2020 are incomplete. Data Source: ERA5 Daily Aggregates (C3S, 2017)

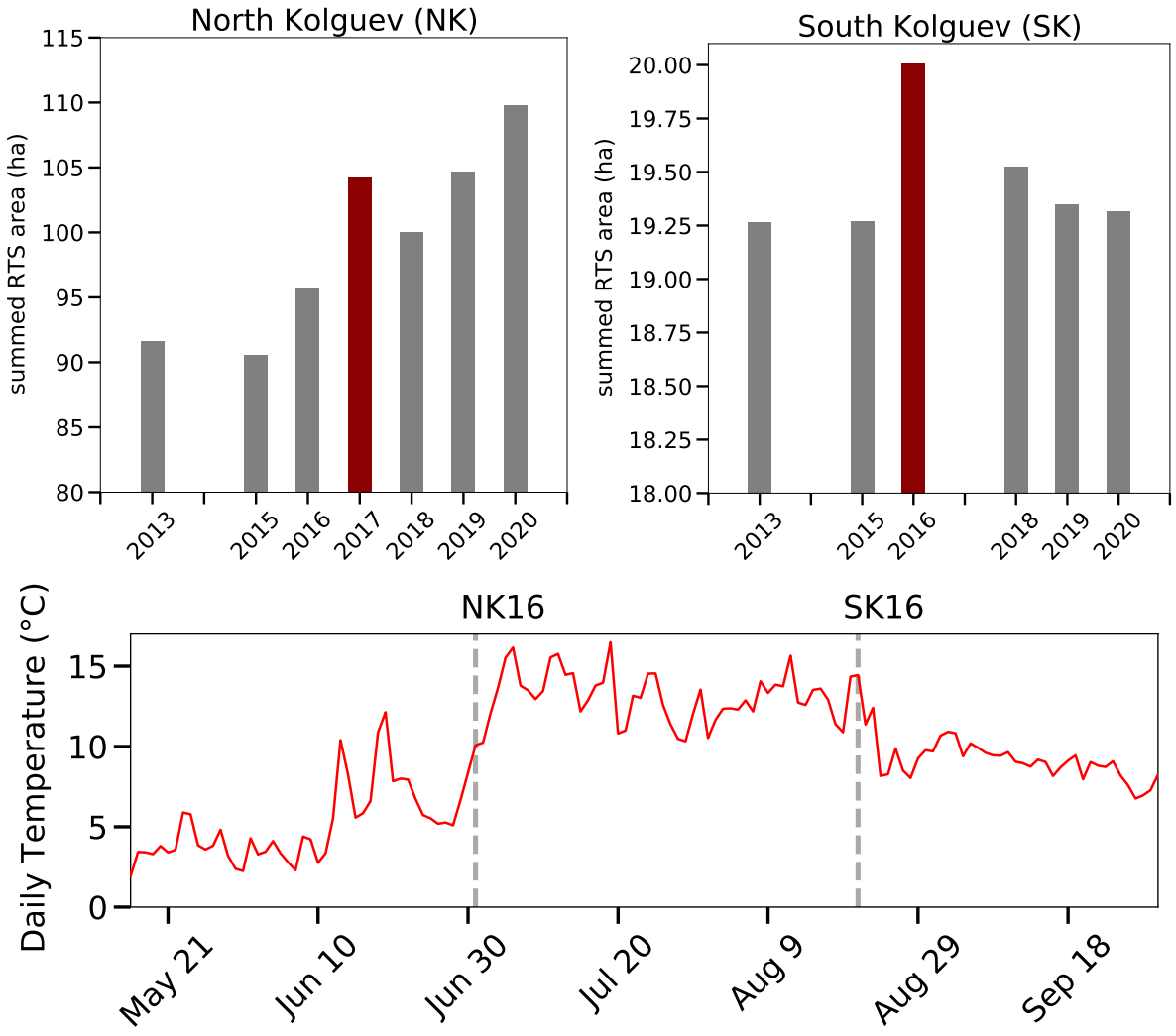

Figure 6.16: Summed RTS area increase in 2016 and 2017 at South and North Kolguev. Top: summed RTS area at North Kolguev and South Kolguev between 2013 and 2020 respectively, bottom: daily temperature in °C between May and September 2016; NK16: acquisition of satellite image of North Kolguev from 2016, SK16: acquisition of satellite image of South Kolguev from 2016. Data Source: ERA5-Land Daily Aggregates (C3S, 2017).

At Bol'shoy Lyakhovsky the monthly average summer and winter temperatures during the investigated years did not deviate as strong from the climatological mean (Fig.6.17). The warmest monthly summer temperatures were observed in August 2019, where temperatures reached on average around 7 °C, 4 °C above average. The warmest monthly winter temperatures were observed in December 2017 and February 2018, where average temperatures reached around -25 °C, 5 °C above average. The total monthly rainfall was not remarkably high in the years studied. Still, an above average rainfall amount accumulated in August 2017, with about 82 mm precipitation (Fig.6.18). Interestingly, at

Bol'shoy Lyakhovsky, where RTS have decreased in area, less severe average temperature deviations occurred, when compared to the other study sites.

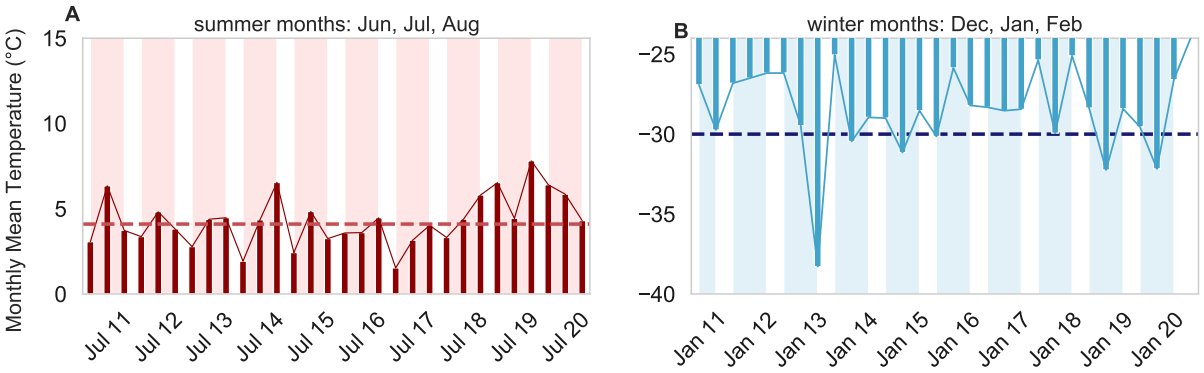

Figure 6.17: Monthly mean temperature data at Bol'shoy Lyakhovsky for the investigated time period (2011-2020). A: monthly mean temperature for summer months (Jun, Jul, Aug) in °C, B: monthly mean temperature for winter months (Dec, Jan, Feb) in °C. The climatological mean (1981-2010) for winter and summer temperatures is shown by the dashed line in blue and red, respectively. Data Source: ERA5-Land Monthly Averaged (Muñoz Sabater, J., 2019) and ERA5 Daily Aggregates (C3S, 2017)

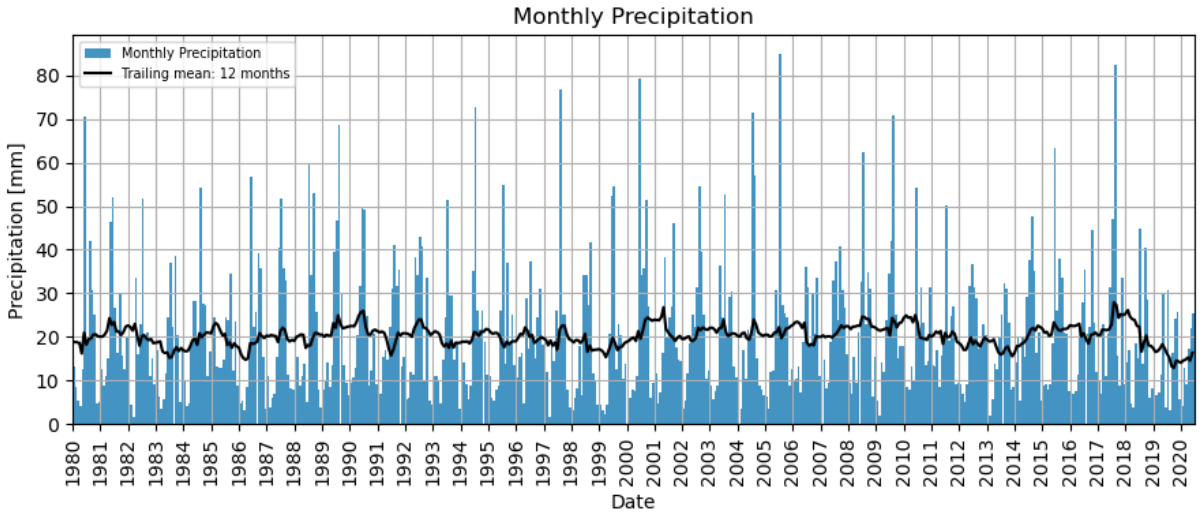

Figure 6.18: Total monthly precipitation data at Bol'shoy Lyakhosvky between 1980-2020. The black line represents the average monthly precipitation over the previous 12 months. Note that precipitation data for 2020 are incomplete. Data Source: ERA5 Daily Aggregates (C3S, 2017)

6.3 Limitations of the study

In the following, some sources of error that affect this study are listed. Firstly, study sites that are susceptible to RTSs activity were intentionally selected. The distribution and

abundance of RTSs varies greatly in space on a pan-acrtic scale as it is strongly influenced by many different factors. RTS characteristics may already look different in the near surroundings of the study sites. In addition, it should be noted that only active RTSs were mapped in this study, the total area affected by RSTs cannot be determined by this procedure.

6.3.0.1 Imagery

The spatial resolution of the imagery used in this study varied between 0.5 and 5 m. In addition, a coarser resolved data set, the Landsat Trend product, was used for verification purposes. To better quantify uncertainties which result from the different spatial image resolutions, a reference data set was created. RTSs were mapped in the same subregion of Novaya Zemlya for the same year (2016) on both Pléiades and RapidEye imagery. The results showed that the summed RTS area mapped was 9 % larger on RapidEye (5 m res.; imagery with the lowest resolution) than Pléiades (0.5 m res.; imagery with the highest resolution) image. The image resolution therefore influences the mapped extent of the RTS-affected area. It should be taken into account however, that this difference of 9 % is likely not only the result of different spatial image resolution as the images had not been acquired at the same time. The Pléiades image was acquired on 07.09.2016 and the RapidEye image on 18.09.2016. As RTSs are dynamic land forms their size can change even within a short time period of several days.
Furthermore, despite co-registration of the images, there are still slight image shifts between the image sets present, which potentially affect the calculations (especially thermal abrasion and thermal denudation change distances/rates).Additionally, interfering factors such as cloud cover, cloud shadows, snow and spectral irregularities have appeared in individual images which further complicates the mapping process.

6.3.0.2 Mapping uncertainties

The extent of active RTSs had been defined and mapped differently in the past. In this study, active RTSs were mapped based on the available image data and definitions in the literature (see 4.2.2 Manual mapping of active RTSs). I tried to exclude debris tongues, however, it was sometimes difficult to distinguish them from active parts of the scar zone. Therefore, it is possible that in some cases these were added to the active slump outlines.

In particular, there were limitations in mapping smaller slumps due to spatial resolution. It cannot be completely ruled out, that inactive slump parts or undisturbed terrain was included. Furthermore, other features such as small lakes may have been mislabeled as RTSs. Intersecting RTSs also posed a challenge; they were counted as a single one when it was no longer possible to draw a clear boundary between the individual features. In addition, changes in the water level and wind direction may have affected the mapping of the bluff base.

6.3.0.3 Change rate calculations

The calculation of thermal abrasion and thermal denudation rates can involve additional uncertainties. Especially, geometric distortions and inter-imagery shifts affect the accuracy. Furthermore, the comparison of change rates along headwalls and bluffs can be difficult, if the number of transects is unequal due to the differing lengths of these features.

Although the method has some shortcomings, as mentioned above, it is a reasonable approach to mapping, quantifying, and analyzing the distribution of RTSs in different high Arctic regions. Compared to an automated mapping approach, which would certainly have sped up the analysis, this study shows that manual mapping revealed high accuracy, as a variety of meaningful results were produced.

7 Conclusion

The aim of this master thesis was to quantify and characterize planimetric change rates of Retrogressive Thaw Slumps in the Russian High Arctic between 2011/2013 and 2020. The study examines five study sites susceptible to RTS activity, located on Kolguev island, Novaya Zemlya archipelago, Bol'shoy Lyakhovsky island and Taymyr Peninsula. The sites are located in ice-rich permafrost characterized by buried glacial ice deposits or syngenetically formed Yedoma permafrost. At Bol'shoy Lyakhvsky and Kolguev, RTSs were observed along the coast (coastal study sites). At Taymyr and Novaya Zemlya, RTSs were initiated mainly on inland hillslopes and lakeshores (non-coastal study sites). The total study area comprises 627 km^2 and a total number of 3466 individual RTSs were mapped.

The main findings of this study are the following:

- RTSs revealed overall high activity at the studied sites between 2011 (or 2013) and 2020, yet the diverse study sites showed quiet different RTS characteristics.
- Coastal and non-coastal RTSs showed varying degrees of areal change, with the non-coastal RTSs experiencing a much larger increase in RTS-affected area.
- At the non-coastal sites, the summed RTS area increased by a factor of 2 (100 %) at West Taymyr, a factor of 4 (400 %) at Novaya Zemlya, and a factor of 33 (3300 %) at East Taymyr, mostly showing a particularly sharp increase in more recent years.
- At the coastal sites, the summed RTS area increased by a factor of 1.2 (20 %) at North Kolguev, remained the same at South Kolguev and slightly decreased by a factor of 0.95 (5 %) at Bol'shoy Lyakhovsky. Headwall and Bluff retreat progressed at all coastal sites. However, depending on the importance of thermal abrasion and thermal denudation, different rates of headwall and buff base erosion were observed. This reveals that areal changes alone cannot be used to determine slump activity at coastal sites. A decrease in RTS area for example could be caused by thermal abrasion dominating over thermal denudation, meaning that buff base erosion progresses faster as headwall retreat.
- The number of RTS did not necessarily increase with increasing RTS activity. At

all study sites except East Taymyr, RTS activity resulted from RTS growth rather than new RTS initiation. Especially at Novaya Zemlya and Kolguev, enhanced RTS growth resulted in the merging of neighbouring slumps which led to a decline in the RTS number in time.

- The resulting overall increase in the area affected by RTSs is accompanied by a loss of permafrost, thus exposing the carbon-rich material stored therein to microbial decomposition.
- Above average temperature rises and heavy rainfalls have been associated with RTS growth and initiation in the past. Climate analysis revealed that the mean temperature increased significantly, by up to several degrees, within the last decade at all sites. Extreme years, including heat waves and heavy precipitation events had also been recorded within the investigation period. However, due to the small data set, it was not possible to establish a correlation and to prove a direct relation. Nevertheless, the analysis of the climatic data in relation with the RTS development indicated that the climatic conditions favored RTS activity.

The study showed that RTS activity at diverse sites of the Russian High Arctic has increased recently. As climate change continues, this trend is expected to continue. Since this could lead to an additional release of GHGs into the atmosphere and thus further heat up the climate, the evolution of rapid thaw in high Arctic permafrost regions, including the formation of RTS, needs to be further investigated.

References

Abbott, B. W., Jones, J. B., Schuur, E. A., Chapin III, F. S., Bowden, W. B., Bret-Harte, M. S., Epstein, H. E., Flannigan, M. D., Harms, T. K., Hollingsworth, T. N., et al. (2016). Biomass offsets little or none of permafrost carbon release from soils, streams, and wildfire: an expert assessment. *Environmental Research Letters*, 11(3), 034014.

Alexanderson, H., Hjort, C., Möller, P., Antonov, O., & Pavlov, M. (2001). The north taymyr ice-marginal zone, arctic siberia—a preliminary overview and dating. *Global and Planetary Change*, 31(1-4), 427–445.

AMAP (2021). Arctic Climate Change Update 2021: Key Trends and Impacts. Summary for Policy-Makers. *Arctic Monitoring and Assessment Programme (AMAP)*.

Andreev, A. A., Grosse, G., Schirrmeister, L., Kuznetsova, T. V., Kuzmina, S. A., Bobrov, A. A., Tarasov, P. E., Novenko, E. Y., Meyer, H., Derevyagin, A. Y., et al. (2009). Weichselian and holocene palaeoenvironmental history of the bol'shoy lyakhovsky island, new siberian archipelago, arctic siberia. *Boreas*, 38(1), 72–110.

Ardelean, F., Onaca, A., Chețan, M.-A., Dornik, A., Georgievski, G., Hagemann, S., Timofte, F., & Berzescu, O. (2020). Assessment of spatio-temporal landscape changes from vhr images in three different permafrost areas in the western russian arctic. *Remote Sensing*, 12(23), 3999.

Barr, I. D. & Clark, C. D. (2012). Late quaternary glaciations in far ne russia; combining moraines, topography and chronology to assess regional and global glaciation synchrony. *Quaternary Science Reviews*, 53, 72–87.

Beck, H. E., Zimmermann, N. E., McVicar, T. R., Vergopolan, N., Berg, A., & Wood, E. F. (2018). Present and future köppen-geiger climate classification maps at 1-km resolution. *Scientific data*, 5(1), 1–12.

Bernhard, P., Zwieback, S., Bergner, N., & Hajnsek, I. (2022a). Assessing volumetric change distributions and scaling relations of retrogressive thaw slumps across the arctic. *The Cryosphere*, 16(1), 1–15.

Bernhard, P., Zwieback, S., & Hajnsek, I. (2022b). Accelerated mobilization of organic carbon from retrogressive thaw slumps on the northern taymyr peninsula. *The Cryosphere Discussions*, (pp. 1–24).

Biskaborn, B. K., Grosse, G., Lantuit, H., & Mehrtens, F. (2019a). The pace at which the world's permafrost soils are warming. https://epic.awi.de/id/eprint/55507/1/PM_16012019_Permafrost_EN.pdf.

Biskaborn, B. K., Smith, S. L., Noetzli, J., Matthes, H., Vieira, G., Streletskiy, D. A., Schoeneich, P., Romanovsky, V. E., Lewkowicz, A. G., Abramov, A., et al. (2019b). Permafrost is warming at a global scale. *Nature communications*, 10(1), 1–11.

Brown, J., Ferrians Jr, O., Heginbottom, J. A., & Melnikov, E. (1997). *Circum-Arctic map of permafrost and ground-ice conditions*. US Geological Survey Reston, VA.

C3S (2017). Copernicus Climate Change Service (C3S) .ERA5: Fifth generation of ECMWF atmospheric reanalyses of the global climate. Copernicus Climate Change

Service Climate Data Store (CDS), (Accessed June 2022), https://cds.climate.copernicus.eu/cdsapp#!/home.

DSAS (2018). Digital shoreline analysis system (DSAS) version 5.0 user guide (No. 2018-1179).[Himmelstoss, E. A., Henderson, R. E., Kratzmann, M. G., Farris, A. S..].US Geological Survey. (Accessed Jan 2022), https://code.usgs.gov/cch/dsas.

Ehlers, J. & Gibbard, P. L. (2003). Extent and chronology of glaciations. *Quaternary Science Reviews*, 22(15-17), 1561–1568.

Esri World Imagery (2009). Esri, DigitalGlobe, GeoEye, i-cubed, USDA FSA, USGS, AEX, Getmapping, Aerogrid, IGN, IGP, swisstopo und die GIS-Anwender-Community. (Accessed June 2022), https://services.arcgisonline.com/ArcGIS/rest/services/World_Imagery/MapServer.

Gavrilov, A. V. & Pizhankova, E. I. (2018). Dynamics of permafrost in the coastal zone of eastern-asian sector of the arctic. *Geography, Environment, Sustainability*, 11(1), 20–37.

Glazov, P. M., Loshchagina, J. A., Kondratyev, A. V., Zaynagutdinova, E. M., Kruckenberg, H., & Pokrovsky, I. G. (2021). The long-term monitoring of bird populations on kolguev island in the barents sea. *Arctic*, 74(5 S1), 23–40.

Grosse, G., Romanovsky, V., Jorgenson, T., Anthony, K. W., Brown, J., & Overduin, P. P. (2011). Vulnerability and feedbacks of permafrost to climate change. *Eos, Transactions American Geophysical Union*, 92(9), 73–74.

Günther, F., Kizyakov, A. I., Zimin, M. V., & Sonyushkin, A. V. (2019). : Destruction of coasts with tabular ground ice occurence on Kolguev Island, European Russian Arctic.YuNC Publishing House, https://epic.awi.de/id/eprint/51213/.

Günther, F., Overduin, P. P., Sandakov, A., Grosse, G., & Grigoriev, M. N. (2012). Thermo-erosion along the yedoma coast of the buor khaya peninsula, laptev sea, east siberia. In *Proceedings of the Tenth International Conference on Permafrost, Volume 1: International Contributions* (pp. 137–142).: The Northern Publisher, Salekhard, Russia.

Günther, F., Overduin, P. P., Sandakov, A. V., Grosse, G., & Grigoriev, M. N. (2013). Short-and long-term thermo-erosion of ice-rich permafrost coasts in the laptev sea region. *Biogeosciences*, 10(6), 4297–4318.

Hjort, J., Streletskiy, D., Doré, G., Wu, Q., Bjella, K., & Luoto, M. (2022). Impacts of permafrost degradation on infrastructure. *Nature Reviews Earth & Environment*, 3(1), 24–38.

IPCC (2019). IPCC Special Report on the Ocean and Cryosphere in a Changing Climate. [H.-O. Pörtner, D.C. Roberts, V. Masson-Delmotte, P. Zhai, M. Tignor, E. Poloczanska, K. Mintenbeck, A. Alegría, M. Nicolai, A. Okem, J. Petzold, B. Rama, N.M. Weyer (eds.)] Geneva: Intergovernmental Panel on Climate Change.

IPCC (2021). IPCC, 2021: Summary for Policymakers. In: Climate Change 2021: The Physical Science Basis. Contribution of Working Group I to the Sixth Assessment Report of the Intergovernmental Panel on Climate Change. [Masson-Delmotte, V., P. Zhai, A. Pirani, S.L. Connors, C. Péan, S. Berger, N. Caud, Y. Chen, L. Goldfarb, M.I. Gomis, M. Huang, K. Leitzell, E. Lonnoy, J.B.R. Matthews, T.K. Maycock, T.

Waterfield, O. Yelekçi, R. Yu, and B. Zhou]. Cambridge University Press, Cambridge, United Kingdom and New York, NY, USA, pp. 332, doi:10.1017/9781009157896.001.

Khan, F. (2020). On tsar bomba—the most powerful nuclear weapon ever tested. *Physics Education*, 56(1), 013002.

Kizyakov, A., Zimin, M., Leibman, M., & Pravikova, N. (2013). Monitoring of the rate of thermal denudation and thermal abrasion on the western coast of kolguev island, using high resolution satellite images. *Earth's Cryosphere*, 17, 36–47.

Kizyakov, A. I., Günther, F., Zimin, M. V., & Sonyushkin, A. V. (2019). : Russian Academy of Science Institute of Physicochemical and Biological Problems in Soil Science RAS Okabiolab Ltd. https://epic.awi.de/id/eprint/51214/.

Kizyakov, A. I., Zimin, M. V., Sonyushkin, A. V., Leibman, M., Pravikova, N. V., & Günther, F. (2016). Modern rates of thermal denudation and thermal abrasion on western Kolguev Island , XI. International Conference on Permafrost, Potsdam, Germany, 20 June 2016 - 24 June 2016. doi: 10.2312/GFZ.LIS.2016.001.

Knoblauch, C., Beer, C., Schuett, A., Sauerland, L., Liebner, S., Steinhof, A., Rethemeyer, J., Grigoriev, M. N., Faguet, A., & Pfeiffer, E.-M. (2021). Carbon dioxide and methane release following abrupt thaw of pleistocene permafrost deposits in arctic siberia. *Journal of Geophysical Research: Biogeosciences*, 126(11), e2021JG006543.

Kokelj, S., Tunnicliffe, J., Lacelle, D., Lantz, T., Chin, K., & Fraser, R. (2015). Increased precipitation drives mega slump development and destabilization of ice-rich permafrost terrain, northwestern canada. *Global and Planetary Change*, 129, 56–68.

Kokelj, S., Zajdlik, B., & Thompson, M. (2009a). The impacts of thawing permafrost on the chemistry of lakes across the subarctic boreal-tundra transition, mackenzie delta region, canada. *Permafrost and Periglacial Processes*, 20(2), 185–199.

Kokelj, S. V. & Jorgenson, M. (2013). Advances in thermokarst research. *Permafrost and Periglacial Processes*, 24(2), 108–119.

Kokelj, S. V., Lacelle, D., Lantz, T., Tunnicliffe, J., Malone, L., Clark, I., & Chin, K. (2013). Thawing of massive ground ice in mega slumps drives increases in stream sediment and solute flux across a range of watershed scales. *Journal of Geophysical Research: Earth Surface*, 118(2), 681–692.

Kokelj, S. V., Lantz, T. C., Kanigan, J., Smith, S., & Coutts, R. (2009b). Origin and polycyclic behaviour of tundra thaw slumps, mackenzie delta region, northwest territories, canada. *Permafrost and Periglacial Processes*, 20(2), 173–184.

Lantuit, H. & Pollard, W. (2005). Temporal stereophotogrammetric analysis of retrogressive thaw slumps on herschel island, yukon territory. *Natural Hazards and Earth System Sciences*, 5(3), 413–423.

Lantuit, H. & Pollard, W. (2008). Fifty years of coastal erosion and retrogressive thaw slump activity on herschel island, southern beaufort sea, yukon territory, canada. *Geomorphology*, 95(1-2), 84–102.

Lantuit, H., Pollard, W., Couture, N., Fritz, M., Schirrmeister, L., Meyer, H., & Hubberten, H.-W. (2012). Modern and late holocene retrogressive thaw slump activity on the yukon

coastal plain and herschel island, yukon territory, canada. *Permafrost and Periglacial Processes*, 23(1), 39–51.

Lantz, T. C. & Kokelj, S. V. (2008). Increasing rates of retrogressive thaw slump activity in the mackenzie delta region, nwt, canada. *Geophysical Research Letters*, 35(6).

Leibman, M., Hubberten, H.-W., Lein, A. Y., Streletskaya, I., & Vanshtein, B. G. (2003). Tabular ground ice origin: cryolithological and isotope-geochemical study. Balkema.

Lewkowicz, A. G. (1987). Nature and importance of thermokarst processes, sand hills moraine, banks island, canada. *Geografiska Annaler: Series A, Physical Geography*, 69(2), 321–327.

Lewkowicz, A. G. & Way, R. G. (2019). Extremes of summer climate trigger thousands of thermokarst landslides in a high arctic environment. *Nature communications*, 10(1), 1–11.

Mackelprang, R., Waldrop, M. P., DeAngelis, K. M., David, M. M., Chavarria, K. L., Blazewicz, S. J., Rubin, E. M., & Jansson, J. K. (2011). Metagenomic analysis of a permafrost microbial community reveals a rapid response to thaw. *Nature*, 480(7377), 368–371.

Miroshnikov, A. Y., Laverov, N., Chernov, R., Kudikov, A., Ysacheva, A., Semenkov, I., Aliev, R., Asadulin, E., & Gavrilo, M. (2017). Radioecological investigations on the northern novaya zemlya archipelago. *Oceanology*, 57(1), 204–214.

Muñoz Sabater, J. (2019). ERA5-Land monthly averaged data from 1981 to present. Copernicus Climate Change Service (C3S) Climate Data Store (CDS). (Accessed June 2022), doi:10.24381/cds.68d2bb30.

Nesterova, N., Khomutov, A., Kalyukina, A., & Leibman, M. (2020). The specificity of thermal denudation feature distribution on yamal and gydan peninsulas, russia. In *EGU General Assembly Conference Abstracts* (pp. 746).

Nitze, I. & Grosse, G. (2016). Detection of landscape dynamics in the arctic lena delta with temporally dense landsat time-series stacks. *Remote Sensing of Environment*, 181, 27–41.

Nitze, I., Grosse, G., Jones, B. M., Romanovsky, V. E., & Boike, J. (2018). Remote sensing quantifies widespread abundance of permafrost region disturbances across the arctic and subarctic. *Nature communications*, 9(1), 1–11.

Nitze, I., Heidler, K., Barth, S., & Grosse, G. (2021). Developing and testing a deep learning approach for mapping retrogressive thaw slumps. *Remote Sensing*, 13(21).

Nötzli, J. & Gruber, S. (2005). Alpiner permafrost–ein überblick. *Jahrbuch des Vereins zum Schutz der Bergwelt*, 70, 111–121.

Obu, J. (2021). How much of the earth's surface is underlain by permafrost? *Journal of Geophysical Research: Earth Surface*, 126(5), e2021JF006123.

Obu, J., Westermann, S., Bartsch, A., Berdnikov, N., Christiansen, H. H., Dashtseren, A., Delaloye, R., Elberling, B., Etzelmüller, B., Kholodov, A., et al. (2019). Northern Hemisphere permafrost map based on TTOP modelling for 2000–2016 at 1 km2 scale. *Earth-Science Reviews*, 193, 299–316.

Obu, J., Westermann, S., Kääb, A., & Bartsch, A. (2018). Ground Temperature Map, 2000-2016, Northern Hemisphere Permafrost. Alfred Wegener Institute, Helmholtz Centre for Polar and Marine Research, Bremerhaven, PANGAEA, https://doi.org/10.1594/PANGAEA.888600.

Osterkamp, T. & Burn, C. (2003). Permafrost. In J. R. Holton (Ed.), *Encyclopedia of Atmospheric Sciences* (pp. 1717–1729). Oxford: Academic Press.

Porter, C., Morin, P., Howat, I., Noh, M.-J., Bates, B., Peterman, K., Keesey, S., Schlenk, M., Gardiner, J., Tomko, K., Willis, M., Kelleher, C., Cloutier, M., Husby, E., Foga, S., Nakamura, H., Platson, M., Wethington, Michael, J., Williamson, C., Bauer, G., Enos, J., Arnold, G., Kramer, W., Becker, P., Doshi, A., D'Souza, C., Cummens, P., Laurier, F., & Bojesen, M. (2018). ArcticDEM.

Previdi, M., Smith, K. L., & Polvani, L. M. (2021). Arctic amplification of climate change: a review of underlying mechanisms. *Environmental Research Letters*.

Ramage, J. L., Irrgang, A. M., Herzschuh, U., Morgenstern, A., Couture, N., & Lantuit, H. (2017). Terrain controls on the occurrence of coastal retrogressive thaw slumps along the yukon coast, canada. *Journal of Geophysical Research: Earth Surface*, 122(9), 1619–1634.

Romanovsky, V. E., Smith, S. L., & Christiansen, H. H. (2010). Permafrost thermal state in the polar northern hemisphere during the international polar year 2007–2009: a synthesis. *Permafrost and Periglacial processes*, 21(2), 106–116.

Runge, A., Nitze, I., & Grosse, G. (2022). Remote sensing annual dynamics of rapid permafrost thaw disturbances with landtrendr. *Remote Sensing of Environment*, 268, 112752.

Rusakov, V. Y., Kuz'mina, T. G., Krupskaya, V. V., Gromyak, I. N., Dogadkin, D. N., & Romashova, T. V. (2022). Holocene history of the eastern side of novaya zemlya from glaciomarine sediment records in the tsivol'ki fjord. *Boreas*.

Scheffler, D., Hollstein, A., Diedrich, H., Segl, K., & Hostert, P. (2017). Arosics: An automated and robust open-source image co-registration software for multi-sensor satellite data. *Remote sensing*, 9(7), 676.

Schuur, E. A., Bockheim, J., Canadell, J. G., Euskirchen, E., Field, C. B., Goryachkin, S. V., Hagemann, S., Kuhry, P., Lafleur, P. M., Lee, H., et al. (2008). Vulnerability of permafrost carbon to climate change: Implications for the global carbon cycle. *BioScience*, 58(8), 701–714.

Schuur, E. A., McGuire, A. D., Schädel, C., Grosse, G., Harden, J. W., Hayes, D. J., Hugelius, G., Koven, C. D., Kuhry, P., Lawrence, D. M., et al. (2015). Climate change and the permafrost carbon feedback. *Nature*, 520(7546), 171–179.

Shur, Y., Hinkel, K. M., & Nelson, F. E. (2005). The transient layer: implications for geocryology and climate-change science. *Permafrost and Periglacial Processes*, 16(1), 5–17.

Strauss, J., Laboor, S., Schirrmeister, L., Fedorov, A. N., Fortier, D., Froese, D. G., Fuchs, M., Günther, F., Grigoriev, M. N., Harden, J. W., Hugelius, G., Jongejans, L. L., Kanevskiy, M. Z., Kholodov, A. L., Kunitsky, V., Kraev, G., Lozhkin, A. V.,

Rivkina, E., Shur, Y., Siegert, C., Spektor, V., Streletskaya, I., Ulrich, M., Vartanyan, S. L., Veremeeva, A., Walter Anthony, K. M., Wetterich, S., Zimov, N. S., & Grosse, G. (2022). Database of Ice-Rich Yedoma Permafrost Version 2 (IRYP v2). PANGAEA. https://doi.pangaea.de/10.1594/PANGAEA.940078.

Strauss, J., Schirrmeister, L., Grosse, G., Fortier, D., Hugelius, G., Knoblauch, C., Romanovsky, V., Schädel, C., von Deimling, T. S., Schuur, E. A., et al. (2017). Deep yedoma permafrost: A synthesis of depositional characteristics and carbon vulnerability. *Earth-Science Reviews*, 172, 75–86.

Streletskaya, I., Pismeniuk, A., Vasiliev, A., Gusev, E., Oblogov, G., & Zadorozhnaya, N. (2021). The ice-rich permafrost sequences as a paleoenvironmental archive for the kara sea region (western arctic). *Frontiers in Earth Science*, (pp. 1004).

van Everdingen, R. (2005). Multi-Language Glossary of Permafrost and Related Ground-Ice Terms in Chinese, English, French, German, Icelandic, Italian, Norwegian, Polish, Romanian, Russian, Spanish, and Swedish. International Permafrost Association, Terminology Working Group, 1998.

Walker, D. A., Raynolds, M. K., Daniëls, F. J., Einarsson, E., Elvebakk, A., Gould, W. A., Katenin, A. E., Kholod, S. S., Markon, C. J., Melnikov, E. S., et al. (2005). The circumpolar arctic vegetation map. *Journal of Vegetation Science*, 16(3), 267–282.

Ward Jones, M. K., Pollard, W. H., & Jones, B. M. (2019). Rapid initialization of retrogressive thaw slumps in the canadian high arctic and their response to climate and terrain factors. *Environmental Research Letters*, 14(5), 055006.

Wetterich, S., Rudaya, N., Kuznetsov, V., Maksimov, F., Opel, T., Meyer, H., Günther, F., Bobrov, A., Raschke, E., Zimmermann, H. H., et al. (2019). Ice complex formation on bol'shoy lyakhovsky island (new siberian archipelago, east siberian arctic) since about 200 ka. *Quaternary Research*, 92(2), 530–548.

Zhang, T., Barry, R. G., Knowles, K., Heginbottom, J. A., & Brown, J. (2008). Statistics and characteristics of permafrost and ground-ice distribution in the northern hemisphere. *Polar Geography*, 31(1-2), 47–68.

Appendix

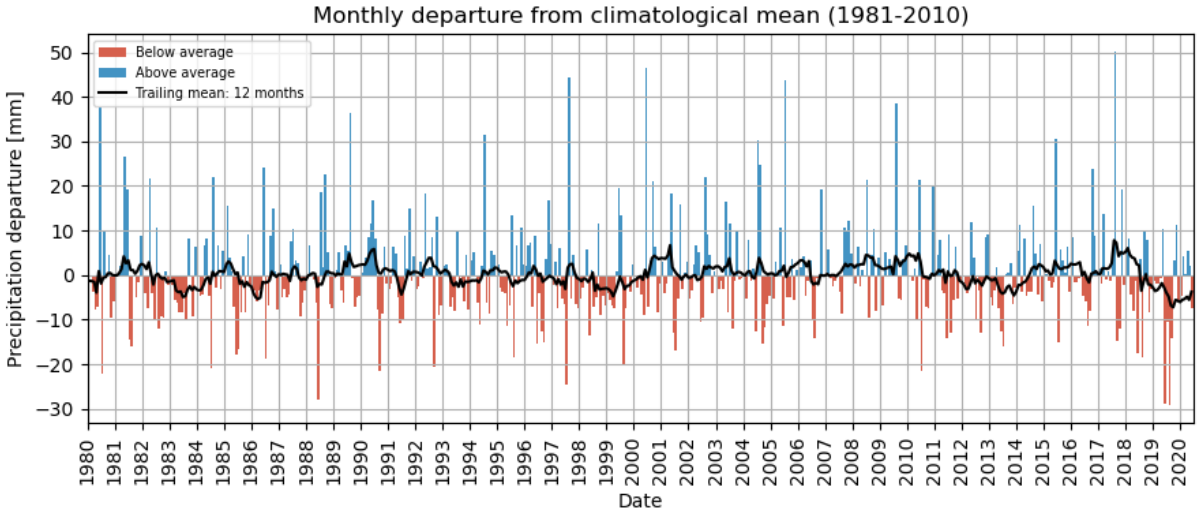

Figure A0.1: Monthly precipitation anomaly at Bol'shoy Lyakhovsky between 1980 and 2020. The black line represents the average monthly temperature over the previous 12 months. Data Source: ERA5 Daily Aggregates (C3S, 2017).

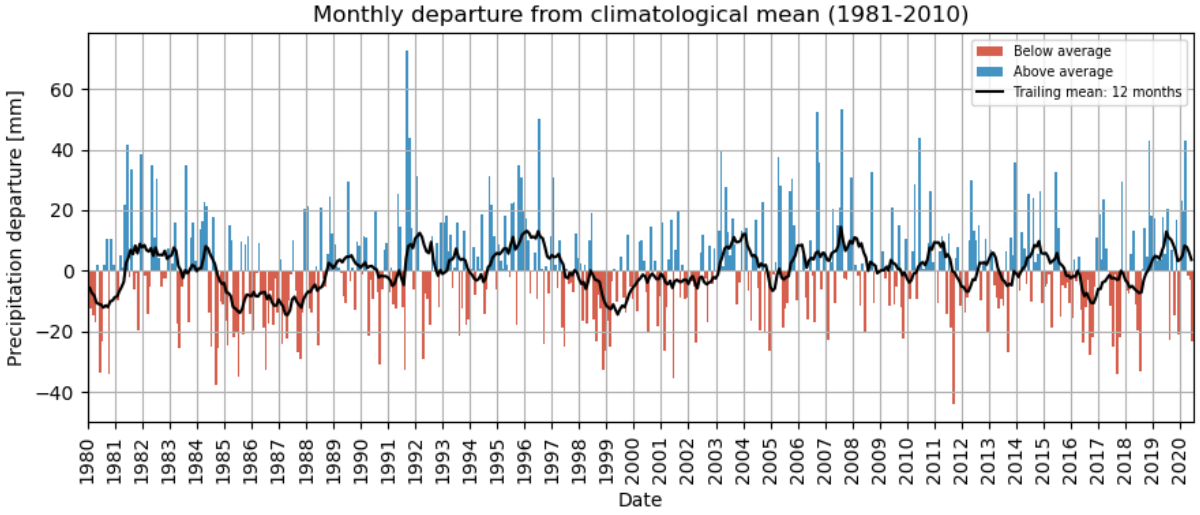

Figure A0.2: Monthly precipitation anomaly at North Kolguev between 1980 and 2020. The black line represents the average monthly temperature over the previous 12 months. Data Source: ERA5 Daily Aggregates (C3S, 2017).

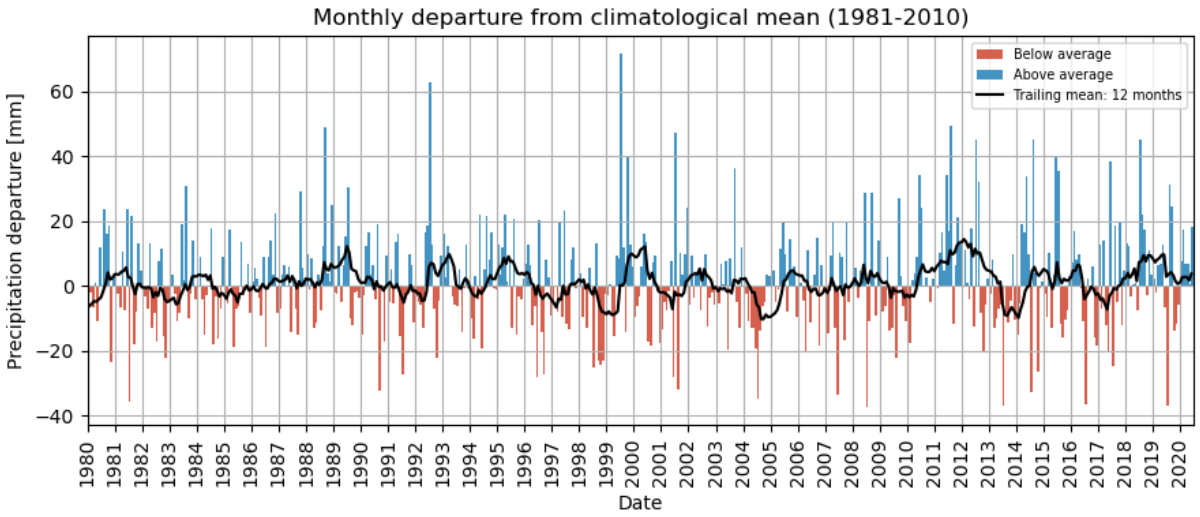

Figure A0.3: Monthly precipitation anomaly at West Taymyr between 1980 and 2020. The black line represents the average monthly temperature over the previous 12 months. Data Source: ERA5 Daily Aggregates (C3S, 2017).

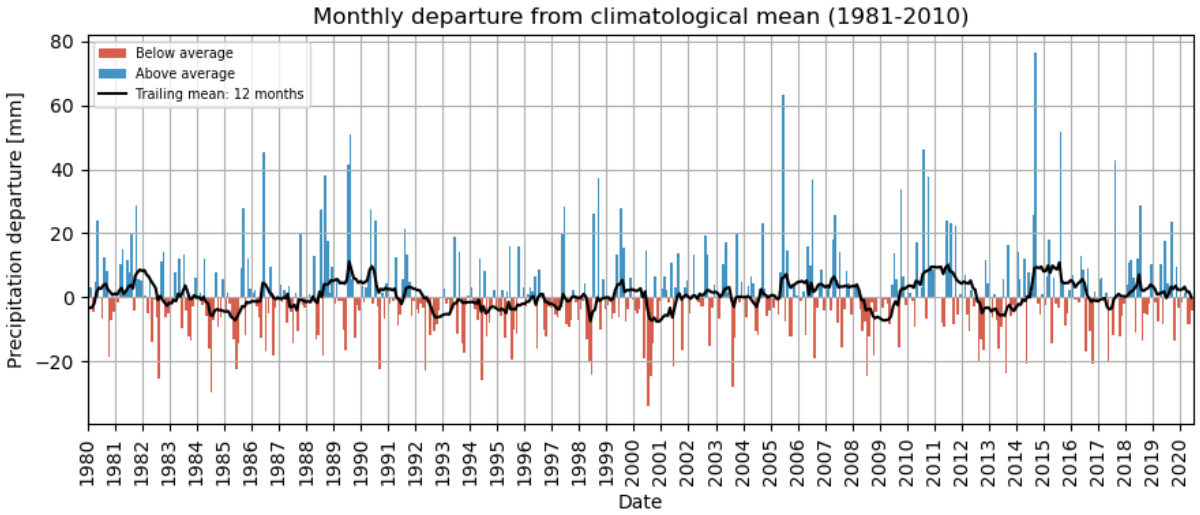

Figure A0.4: Monthly precipitation anomaly at East Taymyr between 1980 and 2020. The black line represents the average monthly temperature over the previous 12 months. Data Source: ERA5 Daily Aggregates (C3S, 2017).

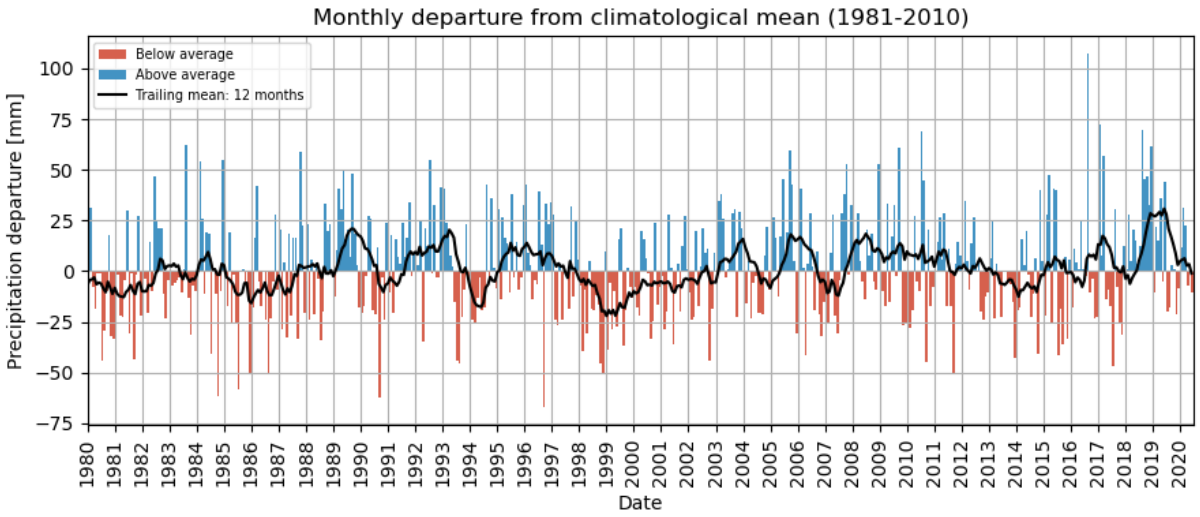

Figure A0.5: Monthly precipitation anomaly at Novaya Zemlya between 1980 and 2020. The black line represents the average monthly temperature over the previous 12 months. Data Source: ERA5 Daily Aggregates (C3S, 2017).

Table A0.1: Very high-resolution satellite image data collection, including image IDs with respective acquisition dates. RE = RapidEye, PS = PlanetScope, S = Spot (6 and 7), P = Pléiades.

Site	Year	Sen.	Image ID
Novaya Zemlya	2013	RE	3973118_2013-09-13_RE3_3A_Analytic_clip.tif
			3973218_2013-09-13_RE3_3A_Analytic_clip.tif
			4073111_2013-09-13_RE3_3A_Analytic_clip.tif
			4073211_2013-09-13_RE3_3A_Analytic_clip.tif
			*2013_novaya_zemlya_north_rap_merged_39N_coreg.tif
	2016	P	DIM_SPOT7_PMS_201609110813081_ORT_5687817101.tif
			*DIM_PHR1A_PMS_201609070908509_ORT_5687819101_coreg.tif
	2018	PS	20180721_051837_1050_3B_AnalyticMS_SR_clip.tif
			20180721_080325_1013_3B_AnalyticMS_SR_clip.tif
			20180721_080326_1013_3B_AnalyticMS_SR_clip.tif
			*2018_novaya_zemlya_north_SR_merged.tif
	2019	S	DIM_SPOT6_PMS_201907260801425_ORT_5687816101.tif
			*DIM_SPOT6_PMS_201907260801425_ORT_5687816101_coreg.tif
	2020	PS	20200722_081436_1032_3B_AnalyticMS_SR_clip.tif
			20200722_081437_1032_3B_AnalyticMS_SR_clip.tif
			20200722_081438_1032_3B_AnalyticMS_SR_clip.tif
			*2020_novaya_zemlaya_north_AnalyticMS_SR_merged.tif
East Taymyr	2011	RE	*2011_taymyr_east_south_rap_merged_coreg.tif
	2016	RE	4973816_2016-09-09_RE1_3A_Analytic_clip.tif
			4973817_2016-09-09_RE1_3A_Analytic_clip.tif
			4973818_2016-09-09_RE1_3A_Analytic_clip.tif
			4973916_2016-09-09_RE1_3A_Analyti_clip.tif
			4973917_2016-09-09_RE1_3A_Analytic_clip.tif
			4973918_2016-09-09_RE1_3A_Analytic_clip.tif
			4974017_2016-09-09_RE1_3A_Analytic_clip.tif
			4974117_2016-09-09_RE1_3A_Analytic_clip.tif
			4974118_2016-09-09_RE1_3A_Analytic_clip.tif
			5074011_2016-09-09_RE1_3A_Analytic_clip.tif
			*2016_taymyr_east_south_rap_merged_50N.tif
			*2016_taymyr_east_south_SR_merged_new_coreg.tif
	2017	S	IMG_SPOT6_PMS_201708130420347_ORT_5694564101_R1C1.TIF
			*IMG_SPOT6_PMS_201708130420347_ORT_5694564101_R1C1_coreg.tif

East Taymyr	2018	PS	20180718_010529_103f_3B_AnalyticMS_SR_clip.tif
			20180718_010530_103f_3B_AnalyticMS_SR_clip.tif
			20180718_010809_100d_3B_AnalyticMS_SR_clip.tif
			20180718_010810_100d_3B_AnalyticMS_SR_clip.tif
			20180718_010811_100d_3B_AnalyticMS_SR_clip.tif
			*2018_taymyr_east_south_SR_merged_coreg.tif
	2019	PS	20190717_042347_1014_3B_AnalyticMS_SR_clip.tif
			20190717_042348_1014_3B_AnalyticMS_SR_clip.tif
			20190717_042350_1014_3B_AnalyticMS_SR_clip.tif
			*2019_taymyr_east_south_SR_merged_coreg.tif
	2020	PS	20200814_044131_1026_3B_AnalyticMS_SR_clip.tif
			20200814_044132_1026_3B_AnalyticMS_SR_clip.tif
			20200814_044133_1026_3B_AnalyticMS_SR_clip.tif
			*2020_east_taymyr_south_AnalyticMS_SR_merged.tif
West Taymyr	2013	RE	4572815_2013-07-20_RE3_3A_Analytic_clip.tif
			*2013_taymyr_west_rap_merged_coreg.tif
	2015	RE	4572815_2015-08-01_RE2_3A_Analytic_clip.tif
			*2015_taymyr_west_rap_merged_coreg.tif
	2017	S	IMG_SPOT6_PMS_201707160614516_ORT_5697254101_R1C1.TIF
			IMG_SPOT6_PMS_201707160614516_ORT_5697254101_R1C2.TIF
			IMG_SPOT6_PMS_201707160614516_ORT_5697254101_R2C1.TIF
			IMG_SPOT6_PMS_201707160614516_ORT_5697254101_R2C2.TIF
			IMG_SPOT7_PMS_201607060600005_ORT_5697253101_R1C1.TIF
			IMG_SPOT7_PMS_201607060600005_ORT_5697253101_R1C2.TIF
			*IMG_SPOT6_PMS_201707160614516_ORT_5697254101_R1C1_coreg.tif
	2018	PS	20180710_031104_0f46_3B_AnalyticMS_SR_clip.tif
			20180710_031105_0f46_3B_AnalyticMS_SR_clip.tif
			20180710_031106_0f46_3B_AnalyticMS_SR_clip.tif
			20180710_031107_0f46_3B_AnalyticMS_SR_clip.tif
			20180710_054436_1044_3B_AnalyticMS_SR_clip.tif
			*2018_taymyr_west_SR_merged_coreg.tif
	2019	PS	20190821_054910_101e_3B_AnalyticMS_SR_clip.tif
			20190821_054911_101e_3B_AnalyticMS_SR_clip.tif
			20190821_054912_101e_3B_AnalyticMS_SR_clip.tif

West Taymyr	2019	PS	20190821_054913_101e_3B_AnalyticMS_SR_clip.tif
			20190821_060333_1013_3B_AnalyticMS_SR_clip.tif
			20190821_060334_1013_3B_AnalyticMS_SR_clip.tif
			20190821_060335_1013_3B_AnalyticMS_SR_clip.tif
			*2019_taymyr_west_SR_merged_coreg.tif
	2020	PS	20200820_060640_89_105c_3B_AnalyticMS_SR_clip.tif
			20200820_060643_36_105c_3B_AnalyticMS_SR_clip.tif
			20200821_055254_1009_3B_AnalyticMS_SR_clip.tif
			20200821_055255_1009_3B_AnalyticMS_SR_clip.tif
			20200821_063207_00_1059_3B_AnalyticMS_SR_clip.tif
			*2020_west_taymyr_AnalyticMS_SR_merged.tif
Bol'shoy Lyakhovsky	2011	RE	5473015_2011-07-24_RE5_3A_Analytic_SR_clip.tif
			5473015_2014-08-13_RE2_3A_Analytic_SR_clip.tif
			*5473015_2011-07-24_RE5_3A_Analytic_SR_clip_coreg.tif
	2016	S	IMG_SPOT7_PMS_201608030226340_ORT_5697230101_R2C2_SR.TIF
			IMG_SPOT7_PMS_201608030226340_ORT_5697230101_R2C1_SR.TIF
			IMG_SPOT7_PMS_201608030226340_ORT_5697230101_R1C2_SR.TIF
			IMG_SPOT7_PMS_201608030226340_ORT_5697230101_R1C1$_S R.TIF$
			$*$ 2016$_bolshoy_spot_merged_coreg.tif$
	2017	S	IMG_SPOT7_PMS_201708310251567_ORT_5697229101_R2C2_SR.TIF
			IMG_SPOT7_PMS_201708310251567_ORT_5697229101_R2C1_SR.TIF
			IMG_SPOT7_PMS_201708310251567_ORT_5697229101_R1C2_SR.TIF
			IMG_SPOT7_PMS_201708310251567_ORT_5697229101_R1C1$_S R.TIF$
			$*$ 2017$_bolshoy_spot_merged.tif$
	2018	PS	20180805_020903_1015_3B_AnalyticMS_SR.tif
			20180805_020904_1015_3B_AnalyticMS$_S R.tif$
			$*$ 2018$_bolshoy_SR_merged_coreg.tif$
	2019	PS	20190706_021956_1035_3B_AnalyticMS_SR.tif
			20190630_021739_1011_3B_AnalyticMS_SR.tif
			*2019_bolshoy_SR_merged_coreg.tif
	2020	PS	20200711_021900_103c_3B_AnalyticMS_SR.tif
			20200713_021440_0f15_3B_AnalyticMS_SR.tif
			*2020_bolshoy_lyakhovsky_AnalyticMS_SR_merged.tif

North Kolguev	2013	RE	3971110_2013-07-21_RE1_3A_Analytic_clip.tif
			*2013_kolguev_north_rap_merged_coreg.tif
	2015	RE	3971110_2015-08-18_RE3_3A_Analytic_clip.tif
			*2015_kolguev_north_rap_merged_coreg.tif
	2016	S	IMG_SPOT6_PMS_201607010818597_ORT_5697295101_R1C1.TIF
			*IMG_SPOT6_PMS_201607010818597_ORT_5697295101_R1C1_coreg.tif
	2017	S	IMG_SPOT7_PMS_201707110830031_ORT_5697296101_R1C1.TIF
			*IMG_SPOT7_PMS_201707110830031_ORT_5697296101_R1C1_coreg.tif
	2018	PS	20180923_080223_0f34_3B_AnalyticMS_SR_clip.tif
			*20180923_080224_0f34_3B_AnalyticMS_SR_clip_coreg.tif
	2019	PS	20190907_081306_100c_3B_AnalyticMS_SR_clip.tif
			*2019_kolguev_north_SR_merged_coreg.tif
	2020	PS	20200823_081434_1009_3B_AnalyticMS_SR_clip.tif
			*2020_kolguev_north_AnalyticMS_SR_merged.tif
South Kolguev	2013	RE	3871020_2013-07-21_RE1_3A_Analytic_SR_clip.tif
			*2013_kolguev_south_rap_merged1_coreg.tif
	2015	RE	3971010_2015-08-18_RE3_3A_Analytic_SR_clip.tif
			*2015_kolguev_south_rap_merged1_coreg.tif
	2016	S	IMG_SPOT6_PMS_201608200832471_ORT_5697272101_R1C1_SR.TIF
			*IMG_SPOT6_PMS_201608200832471_ORT_5697272101_R1C1_coreg _new_wp.tif
	2018	PS	20180801_075816_1021_3B_AnalyticMS_SR_clip.tif
			20180801_075817_1021_3B_AnalyticMS_SR_clip.tif
			*2018_kolguev_south_SR_merged_coreg.tif
	2019	S	IMG_SPOT7_PMS_201908130812291_ORT_5697273101_R1C1_SR.TIF
			*IMG_SPOT7_PMS_201908130812291_ORT_5697273101_R1C1_coreg.tif
	2019	PS	20190814_080303_100c_3B_AnalyticMS_SR_clip.tif
			20190814_080304_100c_3B_AnalyticMS_SR_clip.tif
			*2019_kolguev_south_SR_merged_coreg.tif
	2020	PS	20200727_080631_101f_3B_AnalyticMS_SR_clip.tif
			20200727_080632_101f_3B_AnalyticMS_SR_clip.tif
			*2020_kolguev_south_AnalyticMS_SR_merged.tif